SLOW COOKING OF PHOTONIC MICRORESONATORS

GABRIELLA ILONA GARDOSI

Doctor of Philosophy

ASTON UNIVERSITY
March 2022

ABSTRACT

New techniques to improve the fabrication precision of microphotonic devices is required to develop their applications in optical signal processing, telecommunication and quantum computing. In addition, advances in microfluidic sensing using WGM (whispering gallery mode) spectroscopy, has shown to be a worthwhile endeavour to achieve ultrahigh sensing of biological, chemical and mechanical processes, reaching single molecule detection. This thesis simultaneously advances these fields via the incorporation of microfluidics on the SNAP (surface nanoscale axial photonics) platform. This work has culminated in the discovery of the slow cooking phenomenon which originates from the silica-water interaction at a water-filled microcapillary fibre.

Chapter 1 presents a background to WGM microfluidic sensing and a review of the known silica-water interaction processes. In Chapter 2, we offer the theoretical background to SNAP technology [1,2], which uses nanoscale modifications of the effective radius variation (ERV) of optical fibres to develop photonic microresonator devices such as frequency comb generators [3,4], delay lines [5], optical buffers [6], and, tunable [7] and transient [8] microresonators.

We characterize the discovered slow-cooking phenomenon in Chapter 3, measuring the temporal and spatial variations of the cut-off resonant wavelength (CWV). Our experimentally simple setup uses two microfibres (MF) to couple into a water-filled capillary fibre. The first MF excites WGMs in the fibre to detect the CWV of the resonant wavelength. The second MF is used for optical heating by broadband light of optical power 56-100 mW, which evanescently penetrates into and becomes absorbed by water to induce heating [9] and water motion [10]. We demonstrate the fabrication of SNAP microresonators over hour-long optical heating durations, which displays linear growth for sufficient heating power and time. However, for higher slow-cooking powers and durations, the growth becomes nonlinear and nonmonotonic.

We advance our fabrication precision by reducing the slow-cooking duration in Chapter 4, to achieve precision in CWV of 1.3 pm/10mins limited by the OSA resolution. We propose that further reduction of the slow-cooking duration can achieve 0.02 pm/10secs in CWV corresponding to precision of just 0.6 pm in ERV. This estimated fabrication precision improves the developed laser post-processing techniques [11,12] on the SNAP platform by two orders of magnitude.

Throughout the thesis we attempt to relate the observed CWVs to known silica-water interaction processes. Most prominently, we suggest the observations of the de- and re-hydroxylation at ambient temperatures [13] in Chapter 3 and the structural relaxation of silica after heating ceases in Chapter 4. To our knowledge, these are the first experimental demonstration of these processes using WGM spectroscopy.

Overall, the demonstrated integration of microfluidics with SNAP technology produces a multitude of avenues worthy of pursuit, summarized in Chapter 5. These include advances in the fabrication of the aforementioned photonic devices and enhancement of microfluidic sensing capabilities which can be applied to a variety of fields of interest.

ACKNOWLEDGEMENTS

I cannot portray the amount of support I have received coming back into education after 9 years away living and working abroad as an artist, waitress, cleaner and driver. I am grateful to my parents for encouraging me on my path though it has been a meandering one!

I do not know what luck has granted me such a wonderful supervisor Professor Misha Sumetsky, who has taught me since my undergraduate degree at Aston University. His unwavering support on my path has made me the scientist I am today.

In fact, everyone I have worked with in the SNAP research group has shaped me. Thanks to Dr. Kirill Tokomokov, Dr. Nikita Toropov, Dr. Yong Yang, Dr. Dashiell Vitullo and Dr. Manuel Crespo for spending their time to mentor me. Their faith that I can make a valuable contribution to science was, and still is, an invaluable contribution to my confidence. Special thanks are reserved for the best laboratory partner, Sajid Zaki, for sharing an insatiable curiosity in physics and in life.

The discovery of slow cooked SNAPs may not have been realised without the previous work by Dr. Tabossom Hamifar, who is now my great photonics conference buddy! Another integral part of the discovery is thanks to the collaboration with Bell Labs, especially Dr. Brian J. Mangan and Gabe S. Puc who made custom microcapillary fibres with walls thin enough to generate the slow cooking phenomena.

One of the most important sources of inspiration for me has been the community of incredible women who make up WEST (women in engineering, science and technology). Also of great impact, has been the women scientists at Aston University who tutored me, and extended an extra welcome to me as the only woman in my undergraduate Applied Physics class.

Finally, a huge heartfelt thanks to my amazing friends Beff Slinn, Meta Bora and Joy Pinto. I am thankful to Rebecca Percival for our shared love of activities that challenge our minds over matter from slacklining to rock climbing. Fellow scientist and best friend Charlotte Clarke-Bland shines a light for me into science and into life. My sister, Jasmine Gardosi has been the emotional rock that I have needed during these sometimes tumultuous PhD years. They have always understood me even when I have not understood myself and I am immensely grateful for them.

I dedicate my thesis to my late neighbour Ravi Chohan, because our conversations always left me inspired, in particular our last conversation when he told me:

"Light is the future".

Relevant Publications

Peer-reviewed journals

G. Gardosi, B. J. Mangan, G. S. Puc, and M. Sumetsky, "Photonic Microresonators Created by Slow Optical Cooking," ACS Photonics (2021). https://doi.org/10.1021/acsphotonics.0c01851

D. L. P. Vitullo, S. Zaki, G. Gardosi, B. J. Mangan, R. S. Windeler, M. Brodsky, and M. Sumetsky, "Tunable SNAP microresonators via internal ohmic heating," Opt. Lett. 43, 4316 (2018). https://doi.org/10.1364/OL.43.004316

D. L. P. Vitullo, G. Gardosi, S. Zaki, K. V. Tokmakov, M. Brodsky, and M. Sumetsky, "Discovery of Parabolic Microresonators Produced via Fiber Tapering," Opt. Lett. 43, 4977 (2018). https://doi.org/10.1364/OL.43.004977

Conference Proceedings

G. Gardosi and M. Sumetsky, "SNAP microfluidics," in Photon 2022 Conference, Institute of Physics, Nottingham University (2022).

G. Gardosi and M. Sumetsky, "Picometer-Precise Post-Processing of Optical Microresonators via Slow-Cooking," in 2022 Conference on Lasers and Electro-Optics, OSA Technical Digest (Optica Publishing Group, 2022), paper JW3A.49

G. Gardosi and M. Sumetsky, "Nonlinear formation of photonic microresonators by slow optical cooking," 2021 Conference on Lasers and Electro-Optics Europe & European Quantum Electronics Conference (CLEO/Europe-EQEC), 2021, pp. 1-1, https://doi.org/10.1109/CLEO/Europe-EQEC52157.2021.9542607.

G. Gardosi, Y. Yang, M. Sumetsky, "Slow cooking of SNAP microresonators," in Conference on Lasers and Electro-Optics, OSA Technical Digest (Optica Publishing Group, 2019), paper JTh2A.50. https://doi.org/10.1364/CLEO_AT.2019.JTh2A.50

G. Gardosi, Y. Yang, M. Sumetsky, "Slow Cooked SNAPs," in ONNA Conference 2019, Okinawa, Japan (2019).

G. Gardosi, S. Zaki, D. L. P. Vitullo, K. Tokmakov, M. Brodsky, and M. Sumetsky "Discovery of parabolic SNAP microresonators produced in fibre tapering ", Proc. SPIE 10681, Micro-Structured and Specialty Optical Fibres V, 106810B (2018). https://doi.org/10.1117/12.2307373

G. I. Gardosi, PhD Thesis, Aston University, 2022.

LIST OF CONTENTS

G. I. Gardosi, PhD Thesis, Aston University, 2022.

G. I. Gardosi, PhD Thesis, Aston University, 2022.

LIST OF ABBREVIATIONS

AFM   Atomic force microscopy

BB   Broadband

CW   Cutoff wavelength

CWV   Cutoff wavelength variation

EDFA   Erbium-doped fibre amplifier

ERV   Effective radius variation

FWHM   Full width at half maximum

LCORR   Liquid-core optical ring resonator

µORR   Microfabricated optofluidic ring resonator structures

MCF   Microcapillary fibre

MF   Microfibre

OSA   Optical spectrum analyser

Q   Q-factor

SEM   Scanning electron microscope

SMR   SNAP microresonator

TE   Transverse electric

TEM   Transmission electron microscopy

TM   Transverse magnetic

STM   Scanning tunneling microscope

WGM   Whispering gallery mode

INTRODUCTION

Ever since the invention of the first lasers in the 1960s, photonics has progressed to become the far-reaching and collaborative field of today. Some of the most important innovations of the 21st century have been brought forth as a result of photonics technology, such as global communication, photonic integrated circuits, biophotonics, quantum-enabled technologies and sensors capable of single-molecule detection. Take for example the telecommunications revolution; today we replace our copper phone lines with fibre-optics, which connect the world in a web of terrestrial and marine fibre-optic cables. This allows transatlantic communication in the blink of an eye, thanks to the low signal loss and high bandwidth capability of optical fibres.

Despite such incredible progress, there are many applications of light, which remain in the dark. The untapped potential of light and its properties require new findings in fundamental and applied science. In particular, this includes discoveries of new phenomena in light-matter interaction that can birth as well as support novel photonic technologies. Such developments can expand sensing capabilities and improve fabrication precision of photonic devices for applications in optical signal processing and, potentially, quantum computing.

One of the focused areas of photonic device fabrication is in optical microresonators. Their founding principle is to trap light at multiple discrete frequencies. Such field confinement is achieved using highly reflective boundaries created by a refractive index change. Fabrication of high Q-factor microresonators requires extremely high precision for devices used in optical circuits such as delay lines, frequency-comb generators, switches and buffers; as well as in sensors for the detection of chemical, biological and physical processes.

Surface nanoscale axial photonics (SNAP) is a novel whispering gallery mode (WGM) microresonator platform, which already excels with ultra-high fabrication precision compared to other WGM resonator platforms, currently up to 1.6 GHz precision in resonance frequency (1.3 pm in wavelength). This work develops the SNAP platform by incorporating microfluidics leading to two breakthrough results which promise: 1. unprecedented microresonator fabrication precision and 2. a unique mechanism for the sensing of solid-liquid interactions.

Here, I present the observations of recently discovered effects caused by interactions between silica and water using whispering gallery modes of light on the SNAP platform. I show that these interactions generate a sufficient refractive index contrast to form low loss photonic microresonators. This is a completely new and unique fabrication technique of microresonators, which potentially improves

1

precision by two orders of magnitude, superseding any other platform in microresonator fabrication. Furthermore, to my knowledge this is the first observation of the processes of silica-water interactions induced by optical whispering gallery modes.

1   SENSING BACKGROUND: WGM MICROFLUIDIC RESONATORS AND THE SILICA-WATER INTERACTION

1.1   WHISPERING GALLERY MODE MICRORESONATORS

Whispering gallery modes are a wave phenomenon first discovered by John William Strutt (Lord Rayleigh) a century ago at St Paul's Cathedral. He describes in his paper that "sonorous vibrations have a tendency to cling to a concave surface" [14]. As a wave phenomenon it occurs in optics also, see Figure 1.1, where the resonant wavelength describes geometrical and optical properties of the cavity. A photonic or optical resonator is a dielectric cavity which contains optical resonances. Whispering gallery mode (WGM) resonators use total internal reflection to guide a beam of light in a closed and circular optical path.
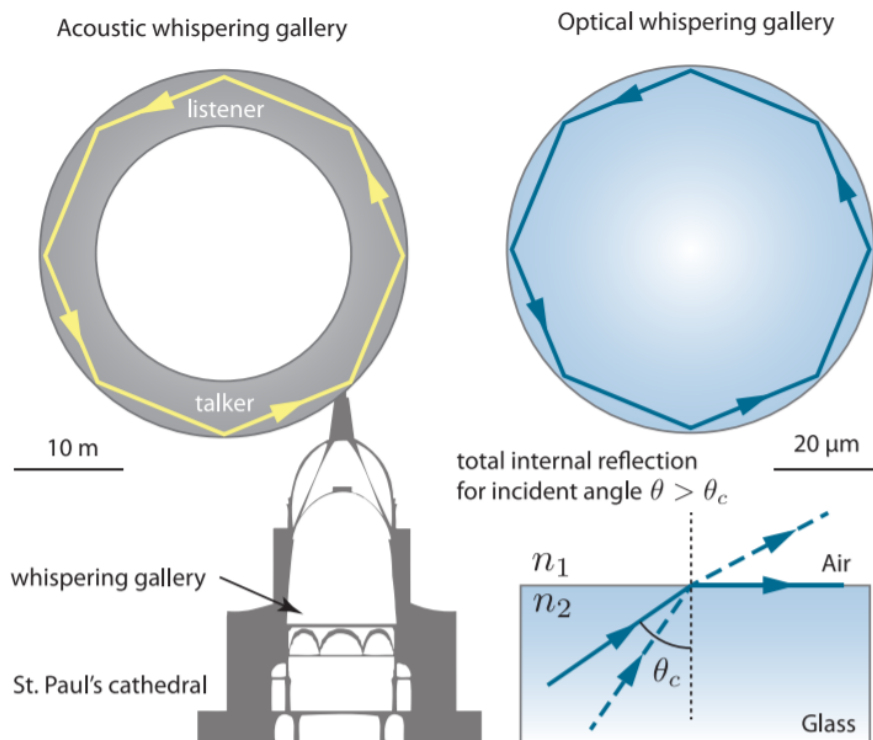

Figure 1.1. Closed acoustic and optical paths supported by total internal reflection in both acoustic (left) and optical (right) waves. From M. R. Foreman et al., "Whispering gallery mode sensors," Adv. Opt. Photon. 7, 168 (2015).

G. I. Gardosi, PhD Thesis, Aston University, 2022.

Resonance occurs due to the spatial overlap and interference of waves within the cavity when the round-trip of light along the cavity circumference is equal to an integer number, m, of wavelengths, λ, given by
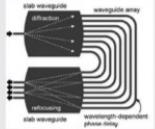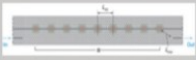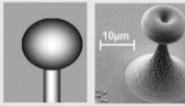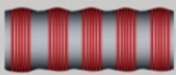
$$2\pi r n_{eff} = m\lambda,$$

where r is the cavity radius and n_{eff} is the effective refractive index of the propagating mode. Changes in the circumferential optical pathway, whether due to absorption or changes in the refractive index and radius, are measurable by shifts in intensity and wavelength of the propagating resonance waves.

Today whispering gallery mode resonators have been developed in the form of microdisks [15], mircrotoroids [16], microspheres [17], microbubbles [18] and specifically what I explore within the SNAP platform, microbottles [11]. The advantages to SNAP technology are outlined in Table 1.1, demonstrating very low loss and extremely high fabrication precision, integral in achieving higher accuracy and efficiency compared to competing microresonator technologies, which will be described in more detail in Chapter 2.

Table 1.1. Comparison of SNAP platform with other resonator fabrication techniques. From M. Sumetsky, "Nanophotonics of optical fibers," Nanophotonics 2, 393–406 (2013).

Platform	Illustration	Dimension of elements	Propagation loss	Fabrication accuracy	Integration
Planar high index contrast		10 μm	0.1 dB/cm	10 nm	Yes
Planar low index contrast		1000 μm	0.01 dB/cm	10 nm	Yes
Photonic crystals		1 μm	0.01 dB/cm	10 nm	Yes
Silica micro resonators		10 μm	0.0001 dB/cm	100 nm	No
Surface nanoscale axial photonics		10 μm	0.0001 dB/cm	0.1 nm	Yes

1.1.1   WGM resonator basic properties

The resonance transmission power of light propagating through a WGM microresonator can be often defined by the Breit- Wigner formula

$$P(\omega) = P_0 \frac{(\gamma_0/2)^2}{(\omega - \omega_0)^2 + (\gamma_0/2)^2}.$$

Here the power amplitude P of the WGM, whose resonant frequency is $\omega = 2\pi/\lambda$ and corresponding full-width half maximum (FWHM) is γ_0, which describes losses, detailed below. Since resonant light is trapped inside of the cavity we infer the WGM spectrum from the transmission power of the input coupled light wavelength, giving rise to Lorentzian transmission dips [19]. Coupling into a WGM is achieved via the overlap between the evanescent fields of a coupler and the excited WGMs of a resonator. Manners of coupling include the use of a prism coupler, slab waveguide or microfibre, summarized in [20]. The Q-factor quantifies the total energy stored in WGMs relative to the energy lost per cycle and is measured with the resonant wavelength and the FWHM as $Q = \lambda_0/\gamma_0$. We consider the following origins of loss. Intrinsic loss pertains to losses in the resonator e.g. material absorption, scattering from surface roughness or other scattering mechanisms including Rayleigh scattering, Mie scattering and geometric optics depending on the scattering sites' geometry and size. Whereas, extrinsic loss is linked to losses via coupling. Both intrinsic and extrinsic losses relate to the Q-factor by $Q^{-1} = Q_{int}^{-1} + Q_{ext}^{-1}$.
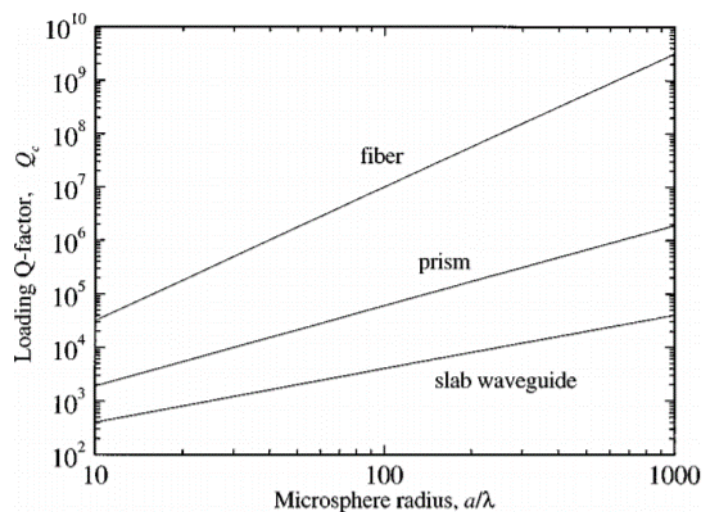
Figure 1.2. The effect of microsphere radius on the Q-factor. From M. L. Gorodetsky and V. S. Ilchenko, "Optical microsphere resonators: optimal coupling to high-Q whispering-gallery modes," J. Opt. Soc. Am. B 16, 147 (1999).

Coupling between the input-output waveguide and microresonator can be separated into three regimes: undercoupling $Q_{int} > Q_{ext}$, critical coupling $Q_{int} = Q_{ext}$ and over-coupling $Q_{int} < Q_{ext}$. To achieve critical coupling we can manipulate either Q_{ext}, e.g. by increasing the resonator-coupler gap, as shown in Figure 1.4., or Q_{int} e.g. by increasing losses in the resonator using a plastic probe attenuator, as shown in Figure 1.3. Figure 1.4. shows how the spectrum of a resonance dip is affected by reducing coupling loss, from over-coupling to critical coupling, characterized as the largest dip or extinction ratio, to undercoupling.
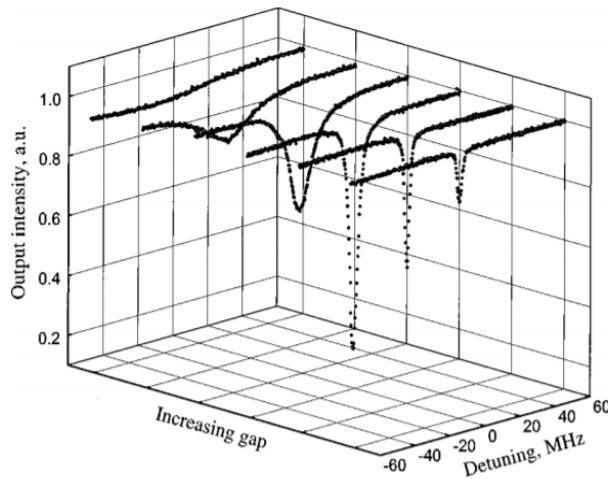
Figure 1.4. Effect on WGM spectrum across coupling regimes. Increasing the gap between prism coupler and microresonator moves coupling towards the undercoupled regime. From M. L. Gorodetsky and V. S. Ilchenko, "Optical microsphere resonators: optimal coupling to high-Q whispering-gallery modes," J. Opt. Soc. Am. B 16, 147 (1999).
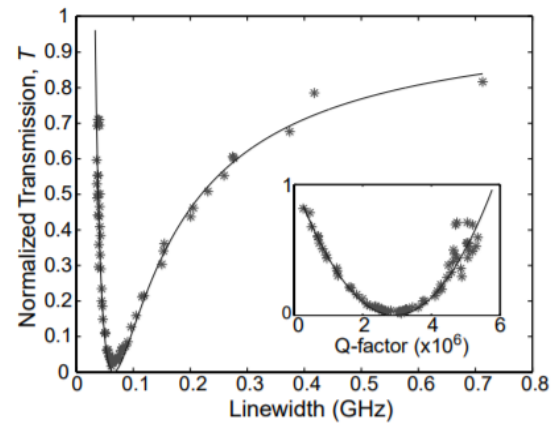
Figure 1.4. Demonstration of zero transmission loss at critical coupling by increasing losses in a microsphere using a plastic probe. From M. L. Gorodetsky and V. S. Ilchenko, "Optical microsphere resonators: optimal coupling to high-Q whispering-gallery modes," J. Opt. Soc. Am. B 16, 147 (1999).

The Q-factor increases linearly with the size of resonator, see Figure 1.. However, a trade-off between a high Q-factor and compactness which gives a desirably large free spectral range (FSR) and small modal volume need to be considered for WGM resonators.

1.1.2   Whispering Gallery Mode Microfluidic Sensors

The combination of WGM resonators with fluidics is an emerging field of investigation developed over the last few decades. It has led to cutting-edge research in both active and passive resonators including biochemical sensors [21,22], droplet-based microlasers [23], and droplet resonators [24]. Regarding sensors, fast progress is being made in detection of biological, chemical and physical processes. Recent reports introduce capabilities in label-free and biocompatible detection [25], single-molecule detection [16,26–28], DNA detection [21] and viral detection [29] broadening the potential for lab-on-a-chip technology.

1.1.2.1   Evanescent wave sensing in microresonators

WGM microfluidic sensors use the evanescent field of the circulating WGM light within capillary fibres such as LCORR (liquid cores optical ring resonator) [30], microspheres [22,25] and ring resonators such as µOFRR (microfabricated optofluidic ring resonator) [31]. The field confinement in these resonators is extremely sensitive to perturbations of the WGM's pathway due to absorption, scattering, refractive index and geometry.

The evanescent field decays exponentially away from the guided light, thus techniques to strengthen the evanescent wave at the sensing region is key to optimize sensitivity. To this end, WGMs whose field has a larger penetration depth are selected, including TM modes, and higher radial modes [26,30]. Figure 1.5(a) illustrates the plane of oscillation of the electric field for clockwise and anti-clockwise WGMs. For the TM-WGM the electric field oscillates parallel to the microresonator radius. Figure 1.(b) shows the electric field amplitude of the TM-WGM of the first radial order $l = 1$ (to be denoted as p, henceforth) and azimuthal order $m = 40$ of a silica microresonator of diameter 10 µm surrounded by air. A closer look at the radial field distribution for the first three radial quantum numbers is shown in Figure 1.(c). We can see that with the increasing radial quantum number the evanescent WGM tail penetrates deeper into the microresonator centre at $\rho = 0$.

Further evanescent wave enhancements involve attachments to the microresonator surface intended for sensing. For example a high-refractive-index layer increases the field amplitude at the microresonator surface [17]. Another example is the use of adsorbed plasmonic nanoparticles to locally boost the evanescent field [32], but such attachments result in Q-factor degradation. Alternatively the microresonator material can be adapted to create a graded-index [33].
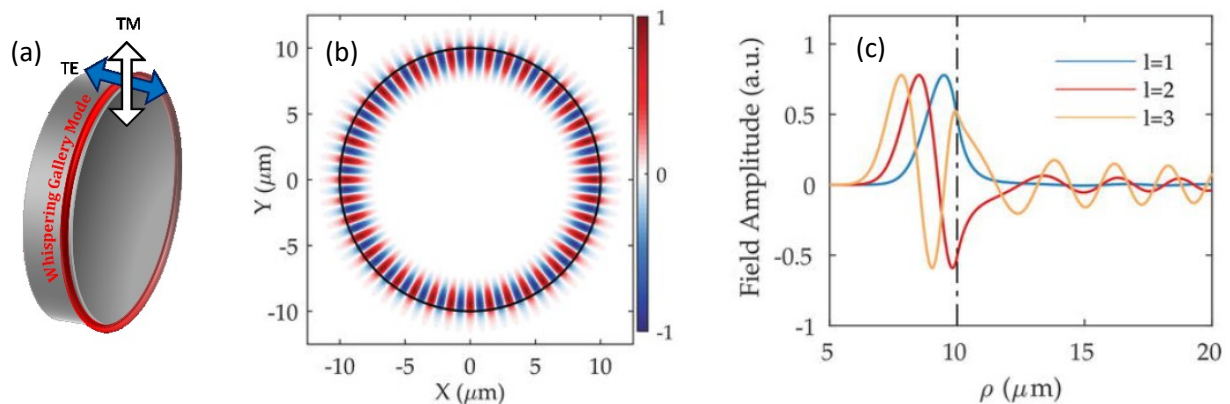
Figure 1.5. Modelling of WGM. (a) Illustration of the electric fields of the TE and TM modes. (b) Optical field of a WGM of quantum numbers m =40 and l =1 in a silica, cylindrical microresonator. (c) Field amplitude of the WGM as a function of the radial coordinate, for m=40 and radial number here denoted as l=1,2,3. (b) and (c) from M. Delgado-Pinar, X. Roselló-Mechó, E. Rivera-Pérez, A. Díez, J. Luis Cruz, and M. V. Andrés, "Whispering Gallery Modes for Accurate Characterization of Optical Fibers' Parameters," in Applications of Optical Fibers for Sensing, C. Cuadrado-Laborde, ed. (IntechOpen, 2019).

G. I. Gardosi, PhD Thesis, Aston University, 2022.

1.1.2.2   Sensing mechanisms

Physical changes in the system are measured by spectral properties of WGMs. For a given coupling efficiency, changes to the WGM resonant wavelength or the resonator Q-factor are measured, illustrated in Figure 1.. Minute changes to the resonator size and local refractive index of the cavity material, generate a shift in the resonant wavelength, see Figure 1.(a). Notably, refractive index change is extremely sensitive to temperature via the thermo-optic coefficient and thermal expansion, which can be applied for highly-sensitive temperature sensors [34,35]. Additionally, molecular adsorption and absorption generates effective radius modifications which shift the resonant wavelength. Demonstrations of label-free single molecule detection show the extraordinary sensitivity of this sensing mechanism [16,21,26,28].
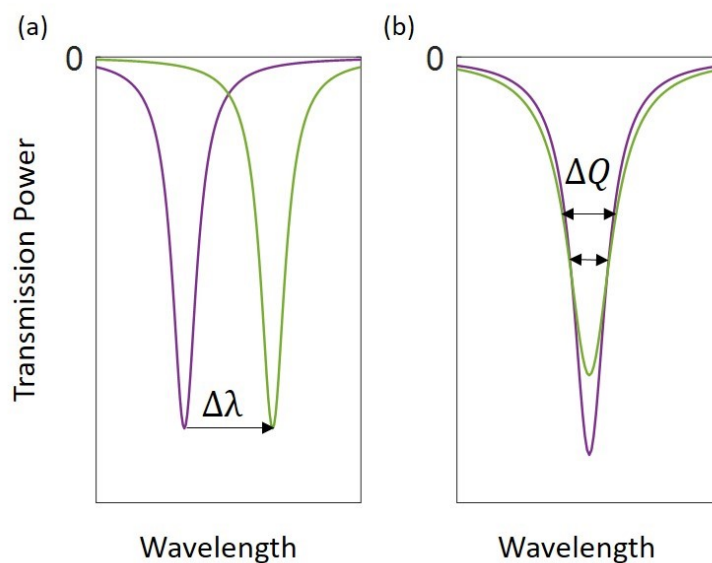
Figure 1.6. Sensing methods for WGM resonators by (a) resonant wavelength shift and (b) Q-factor variation.

Introduction of loss to the system changes the Q-factor of a resonant wavelength, as shown in Figure 1.(b). Loss causes include surface and bulk scattering, absorption and radiation, measurable in high-Q resonators. Such cavity losses defined by the absorption coefficient α, are inversely proportional to the cavity's Q-factor related by $Q_{int} = 2\pi n/\alpha\lambda_0$. The analysis of linewidth changes has been shown to detect single-molecules [27]. In [27], Subramanian et al. placed gold nanorods at a WGM microcavity, which were binding sites for single sub-kDa molecules. Scattering from the plasmonic gold nanorods generated linewidth broadening of the WGM due to unresolved splitting of the mode.

Active whispering gallery modes such as fluorescent-microspheres demonstrate a promising avenue to in-vivo sensing by using biocompatible microresonators which sustain lasing at fluorescent wavelengths measured with a microscope and spectrometer [36]. In these cases, Q-factor reduction

due to the use of fluids can adversely affect the detection limit and must be factored into the plausibility of the sensor for in-vitro and in-vivo sensing.

Usually, microresonators support multiple WGMs which can be used for multi-modal analysis. For example, mode splitting due to the lifting of degeneration occurs with a pressure change in WGM microspheres [19]. Also the use of modes with different quantum numbers e.g. radial numbers [26] can be used to determine changes at higher penetration depths.

While most WGM sensing methods employ the spectra measured at a fixed position of the input-output waveguide (microfibre), Chapter 2 will introduce how the SNAP platform can also measure spectrograms which depend on the spatial position of the waveguide along the microresonator axis. In addition to the temporal and spatial resolution, and apart from Q-factor degradation, the main limitation to sensitivity may be caused by the wavelength resolution of the optical spectral analyser (OSA) connected to the output transmission power.

1.1.2.3 Other known effects in microfluidic WGM resonators/ Nanoparticle trapping

There are other effects within a microfluidic WGM resonator which may contribute to sensing efficacy. Since the confinement of light within the cavity strengthens optical forces leading to radiation heating [24] and pressure [37] concentrated within and around the cavity partly encased by fluid.
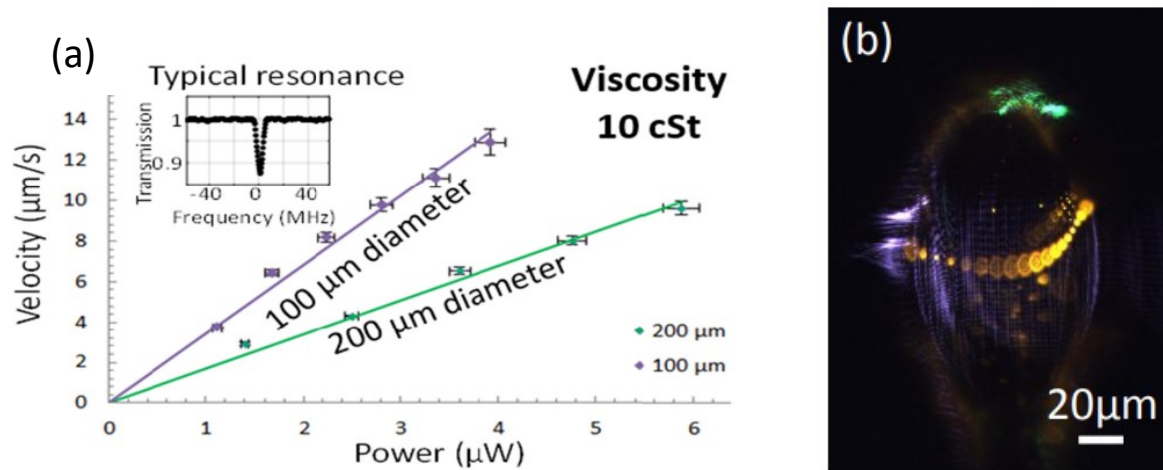
Figure 1.7. (a) Flow speed increases linearly with pumping power for different droplet diameters. (b) Tracking of a nanosphere within a 100 μm droplet by merging video frames a half round trip. From D. Bar-David, S. Maayani, L. L. Martin, and T. Carmon, "Cavity optofluidics: a μdroplet's whispering-gallery mode makes a μvortex," Opt. Express 26, 19115 (2018).

Notably, recent work observed that radiation pressure causes nanoparticles, which are positioned at the vicinity of an evanescent tail, to orbit and to become trapped in a WGM Carousel [38] at orders of power less than the required trapping power in linear waveguides. It stood to reason then, that this angular momentum transfer could generate circular flows within a microdroplet. Bar-David et al.

G. I. Gardosi, PhD Thesis, Aston University, 2022.

demonstrated that WGMs make a microvortex in a droplet see Figure 1.(b). They found that flow speed increases linearly with microwatt power and decreased with the liquid viscosity and resonator size, see Figure 1.(a). [14]

Both flow generation and nanoparticle entrapment are advantageous for sensing by increasing the number of particles in the sensing region and increasing the probability of binding to surface sites by forced re-visitations to the surface. Additionally, fluid mixing can be a useful tool for the study of interactions at the solid-liquid interface due to fresh fluid being introduced at the surface of interest.

1.2   THE SILICA-WATER INTERFACE

Most aforementioned WGM microfluidic sensors are fabricated from silica and their compatibility as sensing devices necessitates interrogation. Intensive multidisciplinary research over the last decades has sought to demystify the silica-water interaction (see refs [39-70] and references therein). Many devices, apparatus and common items are composed of silica, such as optical fibres for telecommunications and glass containers for food. It is thanks to silica's chemical inertness at normal temperature and pressure and much beyond these conditions that render it a reliable, safe and durable material. In particular, it is silica's inertness to water which ensures its many uses. However, water impurities can adversely affect mechanical strength, chemical durability, viscosity and optical properties of silica glass.

The research challenge lies with the ability to measure alterations at the silica-water interface with high spatial and temporal dependence. Developed experimental methods to probe the interaction include vibrational spectroscopy [39–46], optical fibre transmission of light [47], inelastic deformation of optical fibres [48,49] calorimetry [50], AFM [51,52], TEM [53], STM [54] and others. However, these methods limited by the slow silica-water interaction, require that measurable temporal variations last over days, sometimes years. For this reason, many methods accelerate the interaction rate by increasing the surface area of the reaction using silica microparticles [46,55] or porous silica [44] or by heightening pressure and temperature [41,45,56].

The principle processes identified at the silica-water interface are hydrolysis and hydration [41–45,45–61], which can lead to silica dissolution [45,46,55,56], crack formation [51,57] deep water diffusion [47] structural and stress relaxation [41,48,49,62,63], and volume expansion [58]. These processes are interconnected and interdependent, often inferred, bringing about tentative correlations and anomalous results in the literature [59,60,64]. Below, I overview some of these processes relevant to this thesis.

1.2.1 Hydrolysis

Hydrolysis, or specifically at the silica-water interface, silanol formation, occurs when water molecules react to form immobile hydroxyls in an amorphous glass structure by the process,

$$\equiv \text{Si} - \text{O} - \text{Si} \equiv\, +\, \text{H}_2\text{O} \;\rightleftharpoons\; 2 \equiv \text{Si} - \text{OH}, \tag{1.1}$$
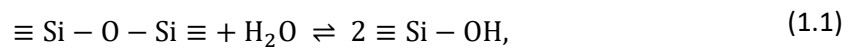
where each horizontal line refers to one chemical bond. The enthalpy of the reaction is $\sim 10.2 \pm 1.2\,\text{kJ/mol}$ [58], though this is a point of discussion in literature thanks to its dependence on the molecular structure of silicates [65], which could take many forms including isolated, vicinal and
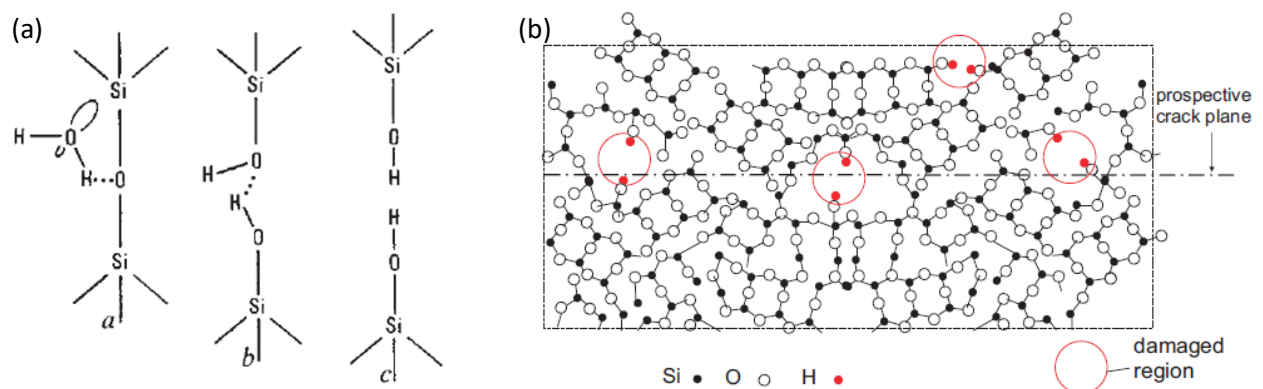
Figure 1.8. Molecular interpretation of hydrolysis in silica. (a) Simultaneous electron and proton transfer at a bridging oxygen atom. (b) Interstitial void creation as silica bonds are broken and replaced by immobile hydroxyls. From T. A. Michalske and S. W. Freiman, "A molecular interpretation of stress corrosion in silica," Nature 295, 511–512 (1982).

germinal silanols [66]. The molecular interpretation shown in the Figure 1.(a), illustrates the simultaneous electron and proton transfer, between a water molecule adsorbed by a bridging oxygen atom of a silica bond. This results in a ruptured bridge creating an interstitial void in the silica network, shown in Figure 1.8(b) [67]. Unstrained surface Si-O-Si bonds react with liquid water at the rate constant $\sim 1 \times 10^{-8}\,\text{s}^{-1}$ at 25°C and neutral pH [68,69].

1.2.1.1 Silica Dissolution

The hydrolysis of the Si-O-Si bond causes the dissolution of silica in the form of silicic acid,

$$\equiv \text{Si} - \text{O} - \text{Si(OH)}_2\text{O}^- + \text{H}_2\text{O} \;\rightleftharpoons\; \equiv \text{Si} - \text{OH} + \text{Si(OH)}_3\text{O}^-(\text{aq}) \tag{1.2}$$
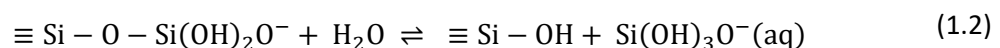
with rate constant $\sim 1 \times 10^{-12}\,\text{mol} \cdot \text{m}^{-2} \cdot \text{s}^{-1}$ at 25°C [70]. Lis et al. demonstrated this dissolution can be increased when water flows along a silica surface [39]. Their investigation measured silica's surface charge using sum frequency generation (SFG) spectroscopy with and without water flow. SFG spectroscopy overlaps both spatially and temporally a visible and tunable infrared pulsed laser beams at a surface of interest to probe surface vibrational modes. The SFG signal is enhanced when the tuned

IR frequency causes vibrational resonance of the surface species. During silica's hydrolysis, negative charge is removed from silica's surface, measured by a decrease in SFG intensity. In [39], they measured a 50% decrease in SFG intensity when flowing water (at pH 6.5) across a silica surface. The forward/backward reaction, shown in Equation 1.2 reaches equilibrium when water at the interface is at rest, due to the saturation of silicic acid of the solution near the surface. However, as water flows, fresh water is introduced to the interface, lowering the silicic acid concentration, thus allowing further hydrolysis, i.e. favouring the forward reaction of Equation 1.2 [39].

1.2.1.2   Volume Expansion

Silanol formation has been found to be dominant cause of volume expansion in silica by Wiederhorn et al. in [58]. Figure **Error! Reference source not found.**(a) graphs the ratio of silanol to water measurements made from multiple authors. Near 90℃, emphasized by the red line, the number of silanol and water molecules is equal, whereas at higher temperatures water's presence in silica is predominantly in the form of silanol. The experiments conducted in [58] exposed 0.25 mm thick silica
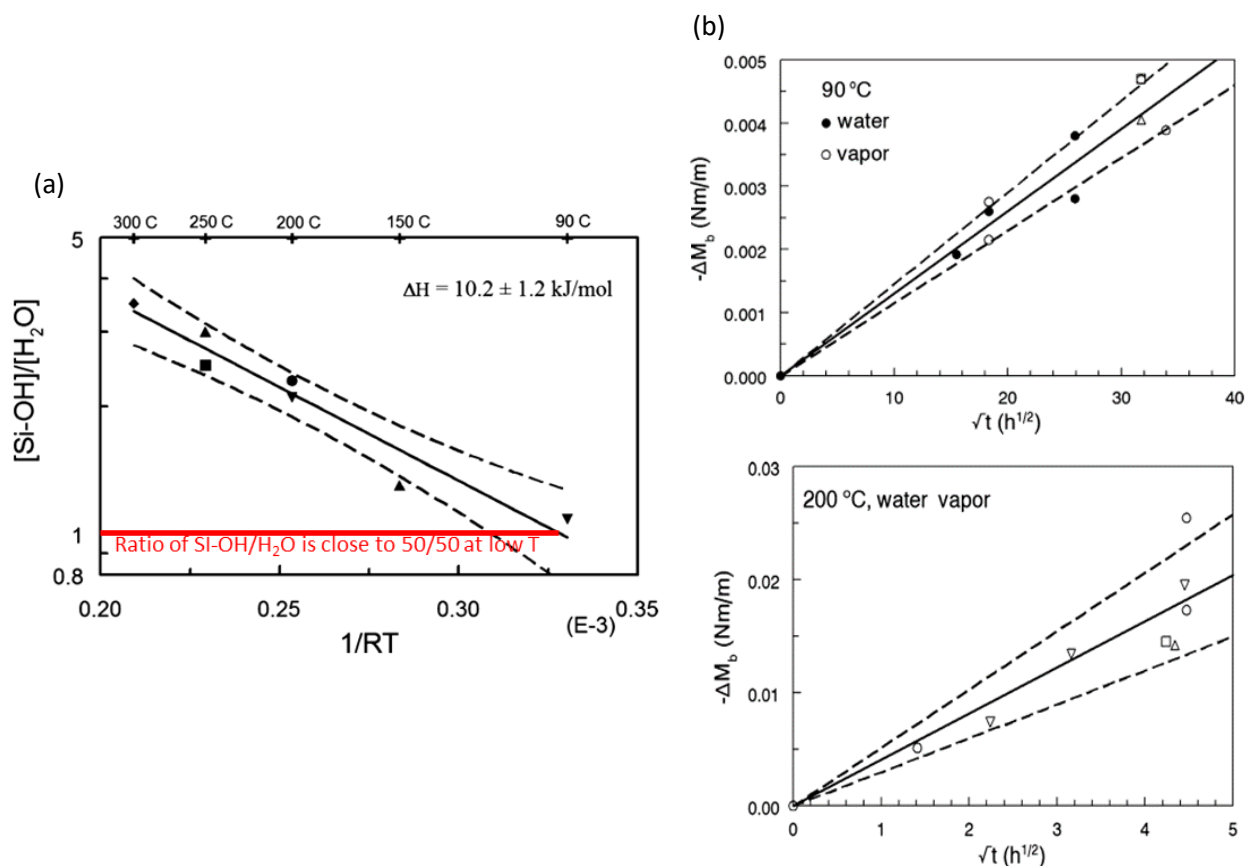
Figure 1.9. (a) The ratio of silanol and water in silica against temperature using IR spectral absorption measurements from multiple authors. Above 300°C the water is present in silica primarily as hydroxyl groups. (b) Bending moments of silica disks with square root of time after exposure to water vapour at 90℃ and 200℃. Source: [14] –(a) added red line to emphasize that the silanol to water ratio is equal near 90℃. From S. M. Wiederhorn, F. Yi, D. LaVan, L. J. Richter, T. Fett, and M. J. Hoffmann, "Volume Expansion Caused by Water Penetration into Silica Glass," J. Am. Ceram. Soc. 98, 78–87 (2015).

disks to 90 ˚C and 200˚C of water vapour for durations of weeks and hours respectively, and measured the disk's radius of curvature caused by volume expansion, shown in Figure **Error! Reference source not found.**(b). At 200°C the presence of molecular water is less than silanol. However, we can see the silica disk's bending moment increased at the higher temperature indicating that in fact hydroxyl diffusion is the dominant cause of volume expansion.

1.2.1.3   Density

It is generally accepted that refractive index changes linearly with glass density $n = C\rho + D$ [71]. In Figure 1. we see that a density decrease of $\Delta\rho = 1 \cdot 10^{-3}$ g/cm^3 approximates to an index reduction of $\Delta n \sim 1 \cdot 10^{-4}$ at wavelength 1.707 µm. The decrease in density can be explained by an increased number of silanol in a glass structure, lengthening the distance between Si atoms [71]. This compliments the earlier supposition (in the previous section) that volume expansion is due to the formation of silanol. The linear relationship between refractive index and density is explained to originate from excess oxygen atoms incorporated into the network during hydrolysis shown in the example of the forward reaction of Equation 1.1.

However in [72], varying glasses of the same density exhibited different refractive indices, which was proposed to be due to structural difference caused by their thermal history. These differences were less than $\pm 3 \cdot 10^{-5}$ in refractive index (comparable to their overall data precision).
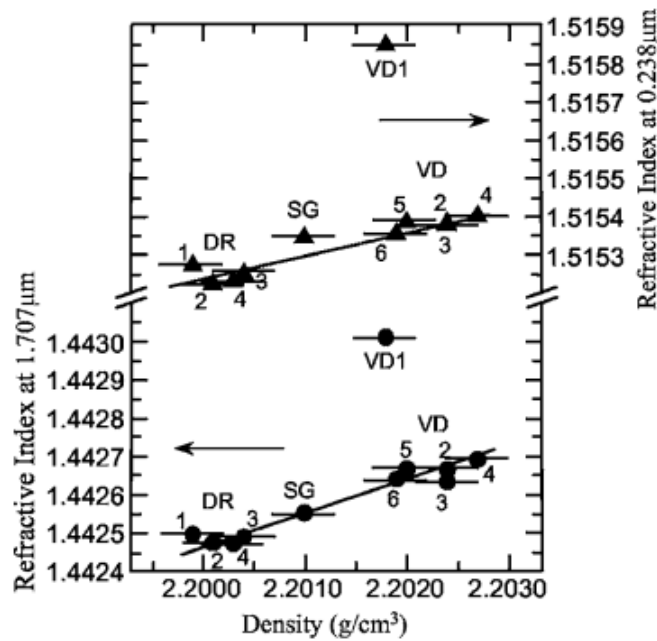
Figure 1.10. Linear relationship between refractive index and density for three types of silica glass at 0.238µm and 1.707 µm demonstrated by the solid lines. From N. Kitamura, K. Fukumi, J. Nishii, and N. Ohno, "Relationship between refractive index and density of synthetic silica glasses," Journal of Applied Physics 101, 123533 (2007).

1.2.1.4   *Crack Formation*

Cracks generated from silanol groups are known to have a surface strengthening effect, used to toughen glass against mechanical failure [49,61]. Compressive stresses found at the tips of cracks can be controlled by the crack depth. Wiederhorn et al. reports that crack depths >1 µm are required for significant toughening and >10 µm for substantial toughening of the silica surface [58]. Of course, the time needed to generate cracks of sufficient length is much longer for lower temperatures. 1000h of vapour exposure was needed to create a 1 µm crack depth at 90 ˚C, which generated a 5% increase in surface strength [58].

1.2.2   Hydration

Hydration is the permeation of water molecules via surface cracks present at an amorphous silica surface. Simply put, the ruptures in the silica network created by hydrolysis, increases the number and depth of cracks allowing water to occupy more spaces within the silica structure. In turn, by allowing further hydration, the number of sites at which hydrolysis can occur increases, thus creating a reinforcing loop of the hydration and hydrolysis processes. However, as summarized in [64], the diffusion rates of these processes differ for vapour and liquid water, due to the formation of a hydration barrier. In the case of liquid water, the diffusion barrier is dissolved into liquid and washed away (see the forward reaction of Equation 1.2) allowing further diffusion.

1.2.2.1 Structural relaxation

Surface structural relaxation is postulated in [41] to be promoted by molecular water diffusion and not silanol formation. This was inferred by using high temperatures up to $1000°C$ to find that the thickness of the relaxed surface layer penetrates deeper than the depth of hydroxyl diffusion. They propose that fast moving molecular water diffuses into silica causing the structural relaxation. Nonetheless at lower temperatures, below $850°C$, the relaxation layer depth drops below the hydroxyl diffusion layer. Experiments to measure the relaxation of silica has required years at ambient conditions [62] or alternatively required the use of temperatures over $1000°C$ [63].

G. I. Gardosi, PhD Thesis, Aston University, 2022.

2 SNAP TECHNOLOGY

2.1 INTRODUCTION

SNAP (surface nanoscale axial photonics) is a developing photonic platform of WGM microresonators fabricated at the surface of an optical fibre. The SNAP devices use nanoscale variations in fibre refractive index and radius, combined as its effective radius variation (ERV), for sensing and microresonator applications using WGMs [11,73]. Similar to other whispering gallery mode platforms, SNAP microresonator devices are commonly fabricated from silica and thus have ultra-low loss (10^{-4} dB/cm) and high Q (>10^7) [73]. However, SNAP microresonators supersede other platforms by boasting sub-angstrom fabrication precision in ERV [5,74]. So far, SNAP devices have developed applications for photonic devices such as frequency comb generators [3,4], delay lines [5], optical buffers [6], tunable [7] and transient [8] microresonators [7,8]. Furthermore, SNAP technology has pursued investigations to develop fundamental understanding of physical processes such as tunneling [8] and theoretical inquiries such as light by light transportation [76].

2.2 GENERAL THEORY AND PROCEDURE

The speed of light is a universal constant; however, by using the near-grazing incident reflections of transversely-circulating WGMs, light exhibits a slow axial propagation, which is extraordinarily sensitive to angstrom variations in the ERV [77]. As noted, SNAP sets itself apart from other WGM platforms by the nanometre-scale spatial ERV of the elongated fibre length unique from WGM resonators formed by rings, microspheres or disks. The wave equation is defined in cylindrical coordinates

$$\left(\nabla^2 - \frac{\delta^2}{\delta z^2}\right)\Psi + \left[\frac{\omega^2}{c^2}n^2(r,\phi) - \beta^2\right]\Psi = 0.$$

(2.1)

WGMs confined by a circular boundary of a fibre have axial, azimuthal, radial and polarization mode numbers, denoted by q, m, p and s respectively. We define the electric field in cylindrical coordinates as,

$$\mathcal{E}_{q,m,p}(\rho,\phi,z) = \exp(im\phi) \cdot U_{m,p}\left(\frac{\rho}{r(z)}\right) \cdot \Psi_{q,m,p}(z).$$

For a WGM-bottle resonator, shown in Figure 2.1. light has slow axial propagation between turning points z_1 and z_2, and the axial dependence of the field is modelled by the 1D stationary Schrödinger equation [1] derived from Equation 2.1 (see Appendix A Subsection A.1 of ref [78]),

$$\Psi_{zz} + [E(\lambda) - V(z)]\Psi = 0$$

The potential $V(z)$ depends on small variations of ERV, $\Delta r_{eff}(z)$ with n_r refractive index, $V(z) = -\kappa^2 \, \Delta r_{eff}(z)/r_0$ where $\kappa = 2^{3/2}\pi n_r/\lambda_r$. If the WGM wavelength λ_r is close to the transmission band edge or cut-off wavelength (CW) λ_{cw} then the WGM propagation constant is found as

$$\beta_c(\lambda, z) = 2^{\frac{3}{2}}\pi n_r \lambda_{cw}^{-\frac{3}{2}}(\lambda_{cw}(z) + i\gamma_{cw} - \lambda)^{\frac{1}{2}} ,$$

where $cw = m, p, s$.

2.2.1 Cut-off wavelength variation

The propagation constant $\beta(z)$ can be very small and, therefore, extremely sensitive to nonuniformities in the fibre characterized by the cut-off wavelength variation (CWV) $\Delta\lambda_{cw}$. These nonuniformities describe changes to the relative physical changes in refractive index and external radius of a fibre with either spatial or temporal dependency,

$$\frac{\Delta\lambda_{cw}}{\lambda_{cw}} = \frac{\Delta n}{n_0} + \frac{\Delta r_{ext}}{r_{0,ext}} . \tag{2.2}$$

Due to the circulating light of a WGM, we can assume that the CWV, averages the change of refractive index and radius around the circumference.

We can interrogate the CWV by tangentially contacting a microfibre coupler with the fibre under test. The input-output microfibre connected to a tuneable laser sweeps over a determined bandwidth. The resultant transmission spectrum $P(\lambda, z)$ reveals the WGM resonant wavelengths indicated by spectral dips measured by the microfibre output at an optical spectrum analyser (OSA). A spectrogram appends transmission spectrums mapping the CWs with dependencies in time or space. It is important to distinguish the different types of CWV which will be referred to in later chapters as the variation is relative to a determined reference point either spatially along z, or temporally.

2.2.1.1 Spatial cut-off wavelength variation/ CW profiles

A spatial spectrogram appends the transmission spectrums measured by translation of a microfibre along a test fibre. The experimental setup shown in Figure 2.1. translates a microfibre and periodically makes contact at z_i with a spatial resolution of $\Delta z = z_{i+1} - z_i$ to map out the CW profile of the scanned fibre length $\lambda_{cw}(z)$, via the transmission power $P(\lambda, z)$ with subangstrom ERV precision [73]. Relatives changes to the CW at a reference point $\lambda_{cw}(z_0)$ are used to find the CWV along the fibre

G. I. Gardosi, PhD Thesis, Aston University, 2022.

using $\Delta\lambda_{cw}(z) = \lambda_{cw}(z_i) - \lambda_{cw}(z_0)$, assuming there are no ambient changes during the scanning time.

 The ERV described as the change in effective radius along the fibre with a reference point, $\Delta r_{eff}(z) = r_{eff}(z) - r_{0,eff}$ and is determined by the rescaling relation with the CWV,

$$\frac{\Delta\lambda_{cw}(z)}{\lambda_{cw}} = \frac{\Delta r_{eff}(z)}{r_{0.ext}}.$$

(2.3)

2.2.1.2 Temporal cut-off wavelength variation/ CW evolution

A temporal spectrogram appends the transmission spectrums measured over time by fixing the position of a microfibre at a test fibre, as shown in Figure 2.1. At a fixed z position, the CW remains constant, assuming there are no ambient changes such as temperature fluctuations which would affect the CW, and thus, we can measure the physical changes of the cavity via $P(\lambda, t)$ with temporal resolution of $\Delta t = t_{i+1} - t_i$. The temporal CWV then is found by subtracting the CW from a reference point $\lambda_{cw}(t_0)$ using $\Delta\lambda_{cw}(t) = \lambda_{cw}(t_i) - \lambda_{cw}(t_0)$.
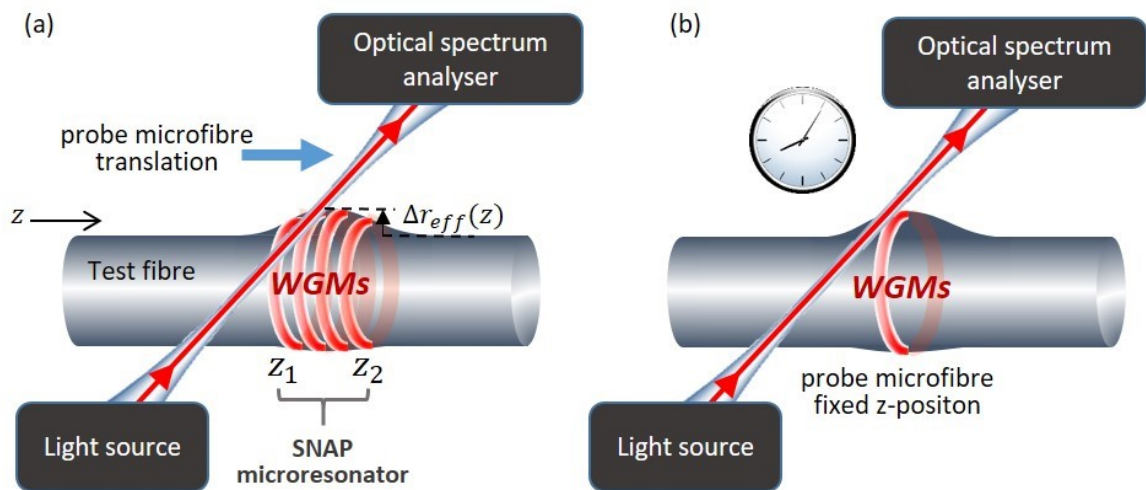
Figure 2.1. WGM spectroscopy of a SNAP bottle microresonator using a probe microfibre taper whose input is connected to a tuneable laser source and output power transmission is measured by the OSA. (a) The probe microfibre is translated along a test fibre with a SNAP microresonator between z_1 and z_2. (b) The same setup as (a) but without microfibre translation, rather the microfibre is fixed at a z-position and takes measurements over time.

In both spatial and temporal spectrograms, the bandwidth sweep of the laser source allows CW tracking of multiple orders of WGMs with differing q, m, p and s quantum numbers. As noted in

G. I. Gardosi, PhD Thesis, Aston University, 2022.

section 1.2.1, a larger p mode increases the radial penetration depth of the WGM tangent to the fibre surface. Additionally adjacent m modes are periodic and their free-spectral range (FSR) $\Delta\lambda_{cw}^{FSR} = \left| \lambda_{q,m+1,p,s} - \lambda_{q,m,p,s} \right|$ can be used to calculate the fibre radius using,

$$r_{0,ext} = \frac{\lambda_{cw}^2}{2\pi n \Delta\lambda_{cw}^{FSR}} .$$

(2.4)

2.3 SNAP MICRORESONATOR FABRICATION TECHNIQUES

The fabrication of SNAP microresonators has taken on many forms since the platform has been developed, summarised in Table 2.1, all of which are made from drawn silica. Thanks to the low surface roughness of drawn silica fibres, there are minimal non-uniformities, making them an ideal canvas for resonator fabrication.

Table 2.1 Comparison of fabrication techniques developed on the SNAP platform. The ERV is calculated using the rescaling relation in Equation 2.3.

SNAP fabrication technique	ERV	Microresonator Extent	Known dependencies
CO_2 laser annealing	$\sim 15\,nm$ Precision $> 0.17\,\text{Å}$	$\sim 50\,\mu m$	Laser power, exposure time, tension of fibre.
Femtosecond laser inscription	$\sim 3\text{-}5\,nm$ Precision $> 0.5\,\text{Å}$	Determined by inscription length.	Laser pulse energy, duration and repetition rate, fibre translation speed, tension of fibre.
Tapering	$\sim 180\,nm$	1-2 mm	Pulling length and speed.
Bending	$\sim 10\,nm$	$\sim 20\,mm$	Bending angle.
HF acid etching	$\sim 300\,nm$	Determined by etching length.	Acid concentration, etching time.
Water droplet	$\sim 30\text{-}100\,nm$	Determined by droplet length.	Refractive index of droplet, capillary wall thickness.
Ohmic tuning	Precision $> 0.2\,pm$	$> 1\,mm$	Input power, diameter of tungsten wire, ambient temperature drifts.
Laser-induced transient SNAP	Temporal stability $=$ $0.7\,\text{Å}$	$\sim 1.2\,mm$	Laser power, beam spot area.

The most commonly used CO_2 laser annealing technique exploits the intrinsic tension frozen-in to the fibre during its manufacture [11,79]. A CO_2 laser beam is focused onto a fibre surface for a predetermined exposure time releasing tension, which has demonstrated the best fabrication precision of just 0.17 Å through post-processing of the ERV [11]. The femtosecond laser method focuses its beam at the fibre's radial centre generating a microresonator via inscription with ERV precision 0.5 Å [80].

The tapering method uses translational stages to stretch a standard 125 μm diameter fibre to ~30 μm inside of a laser-heated microfurnace, which creates a parabolic-shaped resonator at the taper waist [4]. Simple bending of a fibre creates a microresonator whose ERV is proportional to the fibre's loop curvature [81] and could be a promisingly straightforward method for WGM tuning. The more complex multi-stage lithographic method first uses a CO_2 laser to create a polymer jacket mask, followed by hydrofluoric (HF) acid etching, and finally removal of the mask [82]. The water droplet method differs from other methods since there is no modification made to the fibre. Instead, the introduction of a water droplet within a very-thin walled microcapillary fibre (MCF) induces a refractive index sufficient to create square-shaped SNAP resonator [24]. Tuning methods have also been produced such as the ohmic tuning method, for which an etched tungsten wire is thread into a MCF to locally tune with 0.2 pm precision [7]. Finally, an attenuated CO_2 laser beam thermally introduces a transient SNAP with temporal stability of 0.7 Å [8].

Whilst all these techniques produce unique CWV profiles, none have achieved the fabrication precision of the CO_2 annealing method. However, the large range of SNAP fabrication techniques demonstrate the versatility and accessibility of this microresonator platform.

2.4   SNAP MICROFLUIDICS

The potential for SNAP resonators to detect and manipulate microfluidic processes was first explored theoretically in [2]. Figure 2.2 illustrates how replacing a conventional SNAP fibre shown in Figure 2.2(a), to a hollowed-core MCF shown in Figure 2.2(b) and 2.2(c), allows evanescent sensing of a liquid coloured in yellow. It was proposed that circulating WGMs in MCFs, illustrated by the right-hand-side cross-sections, could sense and manipulate micro/nanoparticles located near the internal micron-thin wall. Figure 2.2(c) describes a hollow-core that is asymmetric to the fibre axis, which could increase detection sensitivity by increasing the ratio between the sensing area to liquid volume of the microchannel. The SNAP platform allows measurements with both spatial and temporal dependencies of the physiochemical properties of the contained microfluid.
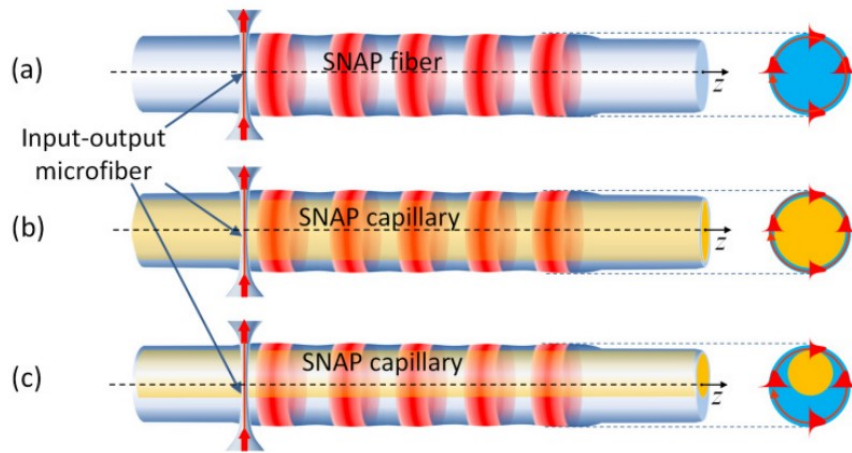
Figure 2.2. Proposed illustrative adaptions of SNAP for microfluidic sensing and illustrations of the circulating WGM light at the fibre cross-sections with their evanescent penetration into a microfluid shown in yellow. (a) SNAP microresonators at a fibre surface; (b) adaptation using SNAP thin-walled capillary fibre; (c) an asymmetrically positioned hollow core. From M. Sumetsky, "Slow light optofluidics: a proposal," Opt. Lett. 39, 5578 (2014).

The first experimental demonstration of SNAP microfluidics was shown in [24] using a symmetric MCF as illustrated in Figure 2.3(a). Hamidfar et al. found that a water droplet within a 136 μm outer-diameter MCF with 7 μm wall thickness created a droplet resonator. In their paper, they determined WGMs which become localized within a thin layer of water adjacent to the internal MCF wall. Figure 2.3(b) shows the modelled spectrogram of a droplet resonator using the 1D stationary Schrödinger equation to approximate the contained WGMs, for radial number, $p = 3$.

During these experiments, slanting of the axial WGMs was observed, see spectrogram in Figure 2.3(c). It was hypothesized that evaporation of the droplet, during the scan, produces this resonant wavelength shift, by reducing the droplet length during data acquisition. Later experiments tested this hypothesis, by timing evaporation of a droplet with and without sensing. It was discovered that without sensing the evaporation time of a same-sized droplet was significantly lower. We can assume therefore that the 0.2 mW tuneable laser power used for WGM spectroscopy caused a heating effect. The work to be presented in the following chapter has been based to further probe this heating effect.

2.5   SUMMARY

SNAP is a demonstrably flexible, versatile, and accessible platform, shown by the great variety of microresonator fabrication methods. The slow axial dependence of WGMs in SNAP relies on controllably changing the ERV. Thus, the ability of introducing ERV with even higher precision is paramount to the development of SNAP as a robust and effective technology. Currently the CO_2

annealing is the most precise method, achieving 0.17 Å in ERV [11]. However, if we want to achieve precision better than sub-angstrom in ERV, we need to establish a new technique.
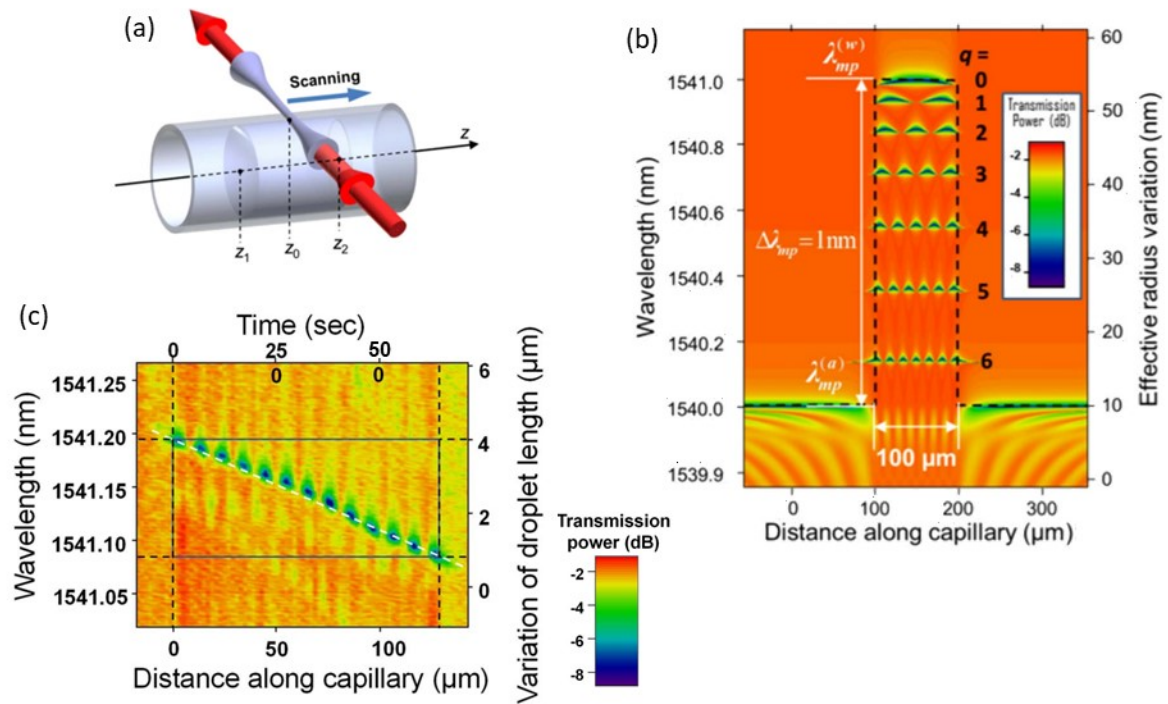
Figure 2.3. Water droplet resonator. (a) Experimental setup of a water droplet contained within a capillary fibre measured using the transversely oriented microfibre. (b) A sample spectrogram of a resultant square-droplet resonator modelled for the water-induced cutoff wavelength shift of 1 nm and predetermined coupling parameters. (c) Zoomed spectrogram of experimental data showing the slanting of axial modes with quantum number $q = 12$, demonstrating evaporation of the droplet during data acquisition. From T. Hamidfar et al., "Localization of light in an optical microcapillary induced by a droplet," Optica 5, 382 (2018).

Combining microfluidics with SNAP has theoretically shown capabilities of micro/nanoparticle detection [2]. The first demonstration of SNAP microfluidic sensing created a novel droplet resonator within a MCF [24]. The evaporation observed during WGM spectroscopy, indicates a heating effect between the input 0.2 mW power delivered by the microfibre and the water droplet. Further work exploiting this effect could expand the capabilities of SNAP microfluidics. This thesis has expanded upon this heating hypothesis, initially aiming to find out if this thermal effect could be used for WGM tuning by internal heating.

3   SLOW OPTICAL COOKING

3.1   INTRODUCTION

This chapter presents a new technique for the formation of a SNAP microresonator (SMR) termed 'slow cooking' referring to the ultra-slow fabrication method using the silica-water interaction. Here we use WGMs for both characterization and heating. The latter effect was discovered by work in [24] and previously mentioned in section 2.4. Preliminary experiments demonstrated that over short time periods thermal tuning and deformation of SNAP resonators could be achieved using this optical heating method as described in Appendix A. Whilst conducting these experiments we found that this heating effect lead to the formation of a permanent SMR when using a high optical power over longer time periods such as 10 hrs. The resultant SNAP microresonator remains after the heat source is removed and also when water is removed from the microcapillary fibre, demonstrating a permanent change in the silica structure. The following experiments presents the characterization of this novel phenomenon demonstrating the formation of a temporary SMR during slow optical cooking, the temporal evolution of spectra during sustained heating and the final permanent slow-cooked SMR.

3.2   EXPERIMENTAL SETUP

The experimental setup, as shown in Figure 2.1. 3.1, consisted of a microcapillary fibre (MCF) and two transversely oriented microfibre tapers, MF1 and MF2, which are placed on other side of the capillary
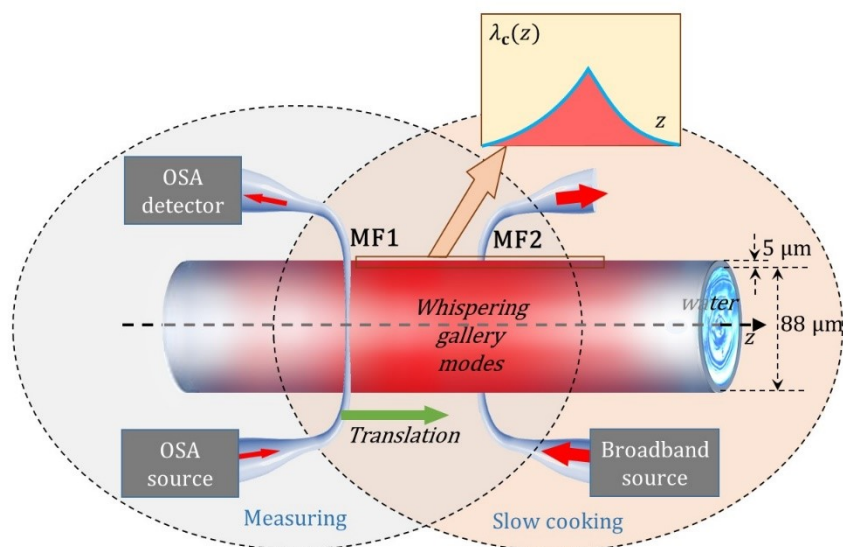
Figure 3.1. Experimental setup. A water-filled silica capillary was oriented perpendicularly to two microfibre couplers, MF1 and MF2. MF1 connected to an OSA, measured the CW profile $\lambda_{cw}(z)$ of the capillary, shown inset. MF2 coupled broadband light and maintained a fixed position along the fibre. The slow-cooking effect along the capillary caused by the broadband WGMs is illustrated in red. From G. Gardosi et al., "Photonic Microresonators Created by Slow Optical Cooking," ACS Photonics (2021).

so that they do not contact each other. The test MCF (hollow capillary fibre, fabricated at OFS laboratories) is chemically etched to remove the external polymer jacket by submerging a middle section ~3 cm of a 15 cm length of MCF into heated sulphuric acid at ~120°C for 2mins, followed by a deionized water rinse. The remaining pure silica cylindrical microcavity has a thin 4.2 μm wall thickness and external diameter 90.6 μm (as measured using a microscope, see Appendix B). The MCF is placed onto an aluminium mount for testing and one end is thread through a blunt microlance needle and epoxied into place to syringe deionized water into the MCF. MF1 and MF2 are fabricated from single-mode OFS G.652.D standard fibre from an initial diameter 125 μm and tapered to approximately 1.7 μm by the ceramic-heated tapering method. They are U-bent and mounted onto acrylic holders each attached to XYZ micro-positioning stages (Aerotech: PRO115LM, ANT130-L and MPS50SL).

MF1, used for measuring, is connected to an optical spectrum analyser (LUNA OVA5000: spectral resolution of 1.3 pm and average power of 0.2 mW), which evanescently couples into excited WGMs of the MCF and characterizes the cut-off wavelength (CW) longitudinal profile, $\lambda_{cw}(z)$ indicated by the transmission dips (blue line of a spectrogram), shown in the inset of Figure 3.1. Further description of this characterization using WGM spectroscopy can be found in the previous chapter, Section 2.2.1. Generally, the recorded transmission power includes the effects of light propagation along the microfibre and inside the MCF. Thus, in some subsequent spectrograms a small angle between MF1 and the MCF creates a quasi-periodic background. Such spectrograms were treated to eliminate this background to determine the $P(\lambda, z)$ of the MCF under study, as explained in Appendix C.

MF2, used for heating, is connected to a broadband light source (1530- 1610 nm bandwidth, average power 20 mW) and an erbium doped fibre amplifier (EDFA: Finisar R7100PB variable gain dual stage) to transmit 63- 100 mW of optical power. Whilst MF1 is near critically-coupled to the capillary for effective measurement, MF2 makes contact with the MCF close to the thinnest point of the taper waist to bring it into the over-coupled regime. Thus, many WGMs are excited simultaneously in the MCF by the input broadband light, which can evanescently penetrate into the capillary wall, and be absorbed by water to generate a heating effect, first observed in [24]. Finally, we added a microscope camera above the setup, to monitor water's presence in the MCF during the experiments.

3.3 CHARACTERIZATION OF SLOW COOKED SNAPS

The results of the following experiment are characterized by MF1 measuring spectrograms in five stages of the slow cooking method which include: spatial CWV along the original and optically heated

water-filled MCF, the evolution of spectra during slow cooking, and finally the irreversible CWV found at the MCF with and without water.

3.3.1   Experimental Procedure

First, we characterize the non-uniformities of 5.5 mm of the original empty MCF. We take a longitudinal scan by translating MF1 along the MCF, periodically contacting it at points z_i with spatial resolution $\Delta z = 20$ μm, to measure the transmission spectrum $P(\lambda_{cw}, z)$. After recording the initial CW profile, $\lambda_{cw}(z)$, MF2 is connected to the MCF at a fixed position and the amplified light source transmits 63-100 W of power to generate a heating effect. The induced CWV is measured by scanning along the same MCF length over 80mins, to find the effect of heating on the empty MCF. The above method is then repeated after filling the MCF with deionised water.

Following the characterization of the temporary CW profile during optical heating, the MCF is scanned to ensure that no permanent changes remain in the MCF. Then MF1 is positioned at the same axial position as MF2, $z = z_{MF2}$ to measure the evolution of spectra in time, $P(\lambda_{cw}, t)$ during the slow cooking process with temporal resolution $\Delta t = 1$min over 12h. During this scanning time we take 5mins of measurements at the beginning and end of the scan during which the optical heating transmitted via MF2 is switched on and off respectively, to discover the immediate CWV before and after the slow cooking process. Final characterization of the MCF after disconnecting MF2 determines the resultant slow-cooked SMR after injecting fresh deionized water into the MCF with spatial resolution $\Delta z = 10$ μm. The MCF is then injected with air and allowed to dry for 12h and scanned again to obtain the CW profile without water with spatial resolution $\Delta z = 20$ μm.

3.3.2   Results and Discussion

The results of a series of slow-cooking experiments made with the same MCF length are shown in Figure 3.2 and presented and discussed in the following sections.

3.3.2.1   Characterization of the original MCF

The original CWs of the water-filled MCF are shown in Figure 3.2(a), where the azimuthal FSR is labelled with a black arrow. We use Equation 2.4 to confirm the external radius of the MCF. We find $r_{0,ext} = 45$ μm, setting $n_r = 1.44$, $\lambda = 1548.4$ nm and $\Delta\lambda_{cw}^{FSR} = 5.9$ nm, which is in good agreement with the microscope measurements, see Appendix B. Figure 3.2(a1) magnifies the blue box shown in Figure 3.2(a) to view the nanoscale nonuniformities of the 5 mm MCF length near $\lambda_{cw} = 1548$ nm, whose CWV is $\Delta\lambda_{cw} \sim 0.1$ nm, equivalent to an ERV of ~ 3 nm, using the rescaling relation in Equation 2.3. Notably the ERV for the empty MCF was equal to the water-filled MCF thus no observable nonuniformities were introduced with the insertion of water.

G. I. Gardosi, PhD Thesis, Aston University, 2022.
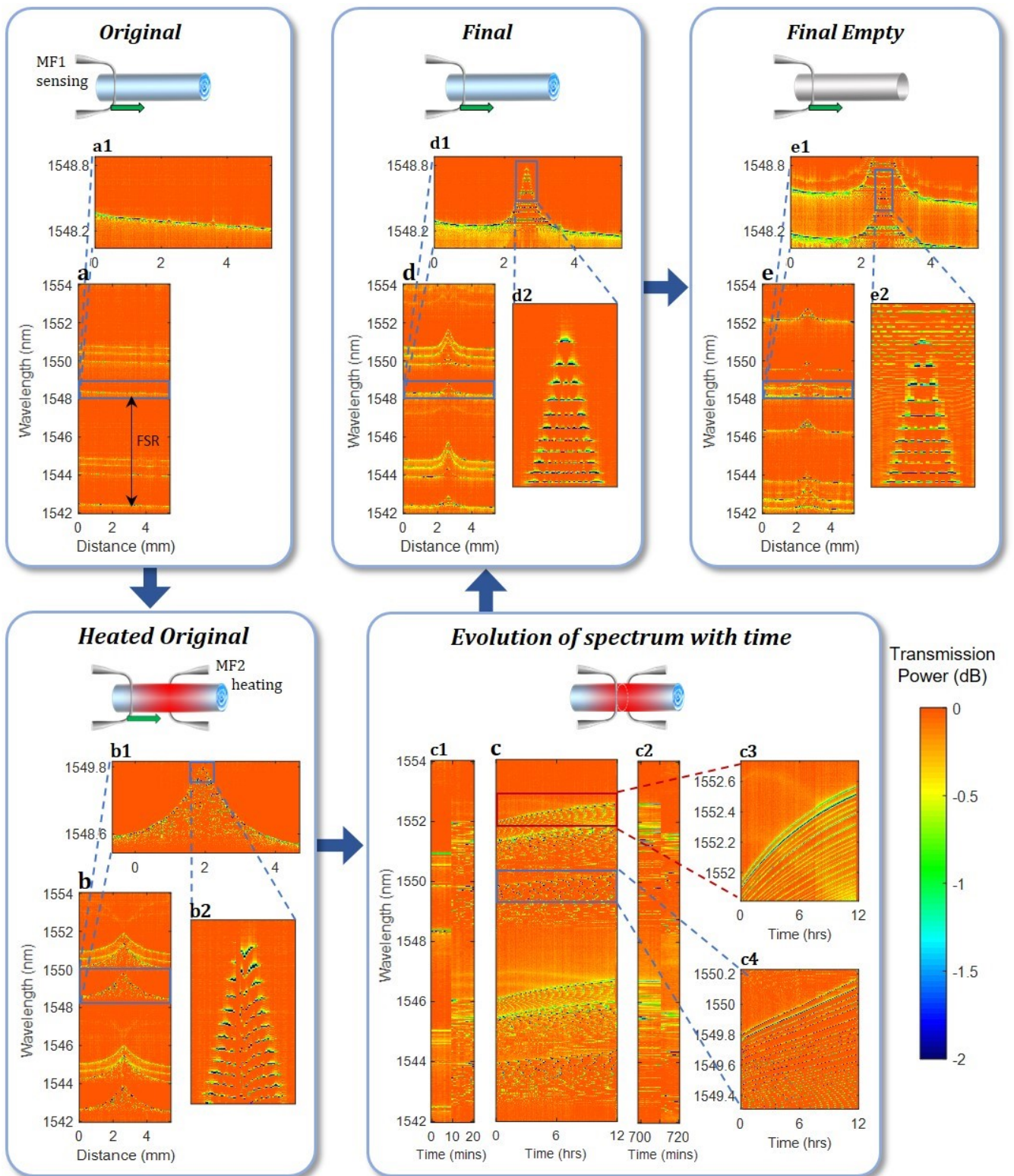
Figure 3.2. The slow cooking process. (a) The control spectrogram, which determines the original cutoff wavelength variation. (b) The spectrogram of the temporary resonator formed by heating with magnified parts shown in (b1) and (b2). (c) The temporal spectrogram showing the variation of spectrum as a function of time at the position of MF2 during the process of slow cooking with magnified parts shown in (c1)-(c4). (d) The spectrogram showing the formation of a permanent microresonator, with magnified parts shown in (d1) and (d2). (e) The spectrogram of the same permanent resonator after water is removed from the MCF and dried for 12 hrs. (e1) and (e2) are magnified parts of spectrogram (e). From G. Gardosi et al., "Photonic Microresonators Created by Slow Optical Cooking," ACS Photonics (2021).

G. I. Gardosi, PhD Thesis, Aston University, 2022.

3.3.2.2 Temporary SNAP generated via optical heating

The next stage investigated the longitudinal CWV induced by optical heating shown in Figure 3.2(b). The 63 mW power used for heating via MF2, was 2 orders of magnitude greater than the power used to interrogate the CWV (0.2 mW) via MF1. Additionally if any heating was caused by MF1 it would be recorded in the original spectrogram shown in Figure 3.2(a1), thus we ignore any heating effect caused by MF1. The temporary resonator magnified in in Figure 3.2(b1) disappeared after heating was turned off, therefore we deduce that there are reversible physical changes to the silica MCF and the contained water. Such reversible changes can be caused by the thermo-optic coefficients of silica, dn_s/dT, water, dn_w/dT or radial expansion of the silica MCF, dr_0/dT. By assuming a uniform temperature distribution over the each MCF cross-section, we determine the temperature distribution along the MCF as,

$$\Delta T(z) = \left(\frac{F_{cw}^{(s)}}{n_s} \frac{dn_s}{dT} + \frac{F_{cw}^{(w)}}{n_w} \frac{dn_w}{dT} + \frac{1}{r_0} \frac{dr_0}{dT} \right)^{-1} \frac{\Delta \lambda_{cw}(z)}{\lambda_{cw}} \, , \tag{3.3}$$

where $F_{cw}^{(s)}$ and $F_{cw}^{(w)} = 1 - F_{cw}^{(s)}$ are the fractions of a WGM localized in the silica capillary wall and water, respectively, with quantum numbers $cw = (m, p, s)$. We can therefore determine the temperature distribution with resolution determined by our spectral resolution of $\Delta \lambda_{cw} = 1.3$ pm which corresponds to a temperature resolution of $\Delta T = \pm 0.1\,°C$. Notably, the temperature distribution is primarily driven by the thermo-optic effect which is significantly larger than the corresponding effect of radial expansion, as we have $\frac{1}{n_s} \frac{dn_s}{dT} = 8 \cdot 10^{-6}/°C$ and $\frac{1}{n_w} \frac{dn_w}{dT} = -7 \cdot 10^{-5}/°C$ while the relative expansion of the fiber radius is $\frac{1}{r_0} \frac{dr_0}{dT} = 6 \cdot 10^{-7}/°C$.

Further magnification in Figure 3.2(b2) shows that the axial eigenwavelengths form a V-shape decreasing near the MF2 contact position. We expect the eigenwavelengths to remain constant along the entirety of the resonator length. However, this measurement artefact grows as MF1 approaches MF2, at the centre of the temporary resonator, and diminishes as MF1 moves away from MF2, to form this V-shape. We suggest then that a fraction of heating power leaks out of MF1 affecting the temperature distribution and decreasing the eigenwavelengths within the resonator. Knowing this, any temperature distribution discovered from the CW profile can only be an approximation, and the temperature may in fact be larger if there is no sensing MF1 in contact with the MCF.

G. I. Gardosi, PhD Thesis, Aston University, 2022.
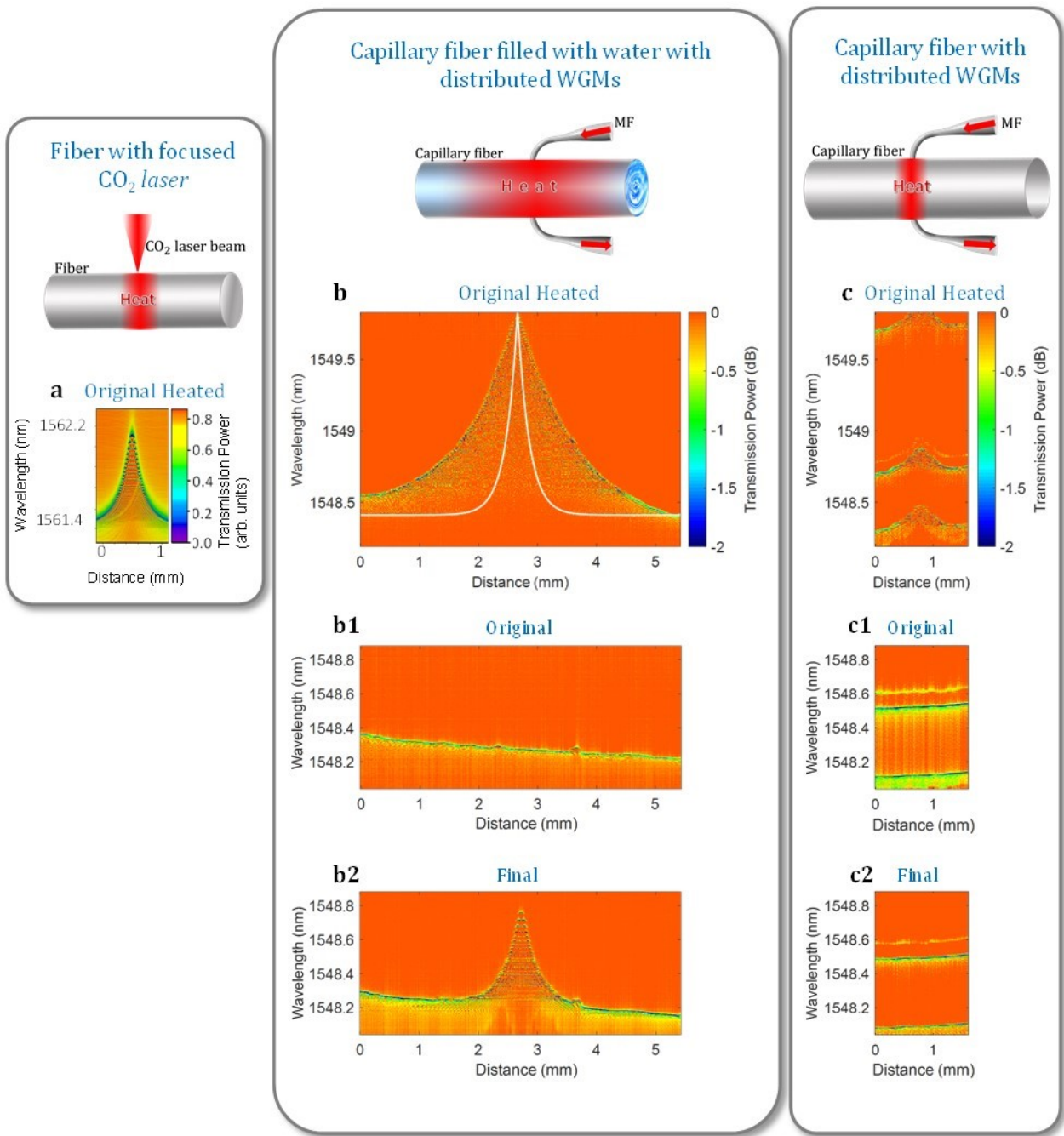
Figure 3.3. Comparison of local fibre heating. (a) Spectrogram of a bulk fibre heated using a focused CO_2 laser beam3. (b) Spectrogram of the heated water-filled MCF from Figure 3.2; (b1) original before heating; (b2) permanently induced microresonator after 12 hour heating. (c) Spectrogram of the heated empty MCF; (c1) original before heating; (c2) after 12 hour heating. From Supplementary section of G. Gardosi et al., "Photonic Microresonators Created by Slow Optical Cooking," ACS Photonics (2021).

3.3.2.2.1 Evidence of liquid water heating by evanescent WGMs

At first glance the temperature distribution is much wider than expected if heating was caused by a point source at the MF2 contact position. To test this, we model the temperature distribution for a point source to compare it with our CW profile which is proportional to our temperature distribution approximation. The stationary 1D heat equation defined as,

$$Q(z) = -k \left(\frac{d^2 \Delta T}{dz^2} \right) + 2h r_{0,ext}^{-1} \Delta T,$$

gives the solution,

$$\Delta T(z) = \Delta T_0 \cdot \exp \left(- \left(\frac{2h}{r_0 k} \right)^{\frac{1}{2}} |z| \right), \tag{3.4}$$

where ΔT_0 is the maximum temperature variation from the heat source, h is the fibre-air heat transfer coefficient $\sim 350 \, \text{W/(m}^2 \cdot \text{K)}$ and k is the thermal conductivity of water $0.65 \, \text{W/(m} \cdot \text{K)}$ and silica $1.38 \, \text{W/(m} \cdot \text{K)}$. The resultant temperature distribution is plotted as a white line overlay in Figure 3.3(b) using the larger thermal conductivity of silica (which yields the widest temperature distribution). We notice that the distribution is significantly narrower than the distribution caused by optical heating, with an extent just over 1 mm vs. the measured temporary resonator extent >5 mm.

Further comparison of our temperature distribution with that induced by a focused CO_2 laser onto a silica fibre is shown in Figure 3.3(a), demonstrated in [8]. Here we see that the temperature distribution from a point heat source is narrower, localized at the CO_2 laser beam. Additionally, we measure the temperature distribution of an empty MCF via optical heating, which is much weaker, shown in Figure 3.3(c). Both temperature variations extend to about 1 mm along the MCF length, as expected for a localized heat source. However, the top of the temperature distribution measured in the empty MCF is stunted probably due to the aforementioned measurement artefact.

As a result, we can assert that our temperature distribution measured with a filled MCF is not caused by a localized heat source, rather it is introduced by WGMs excited by MF2. Remarkably, the axial propagation of the WGMs contained within the turning points of the temporarily created SMR, extends the heating effect along the MCF. The thin wall allows WGMs (including a small fraction of light which directly refracts into water) to evanescently penetrate and become absorbed by water to generate the measured heating effect. Moreover, prior work demonstrates that light-water momentum transfer can cause water motion [10], thus we can expect mixing of the heated water.

3.3.2.2.2 Temperature estimation

We may estimate the maximum temperature change at $z = z_{MF2}$. As the heating power is switched on and off the wavelength variation measured at the beginning and end of the temporal experiment is found to be $\Delta\lambda_{cw}^{init} = 1.43$ nm and $\Delta\lambda_{cw}^{init} = 1.42$ nm, respectively, see Figures 3.2(c1) and (c2). Assuming that the WGM at $\lambda_{cw} = 1548.6$ nm is completely contained by the MCF silica wall, thus by using $F_{cw}^{(s)} = 1$, $F_{cw}^{(w)} = 0$ in Equation 3.3 and ignoring the thermo-optic coefficient for water as well as the small contribution of radial expansion, we find that the corresponding temperature change is $\Delta T_{init} = 110.7°C$ and $\Delta T_{fin} = 109.9°C$. The 0.8°C variation in temperature change from intial and final measurements is larger than our resolution $\pm 0.1°C$, thus likely due to an ambient temperature change during the 12h experiment. Considering the room temperature during the experiment was ∼22°C, the maximum measured temperature of the MCF was ∼130°C. Despite being above the water's boiling point, the optical microscope images taken during the experiment indicated no evaporation of water. In fact, we know that water evaporation is measurable by a steep drop in CWs of the transmission spectrum, see Appendix D. The explanation of this result may be caused by water flow, or that water remains in a superheated liquid state [83–85]. However further investigation is needed to determine the cause of this phenomenon.

3.3.2.2.3 Multi-modal analysis

Until now, we have discussed the results found in the vicinity of a single CW, which we assume to correspond to the lowest radial number $p = 0$. This is a fair assumption, since the we expect the largest CWV during initial heating to correspond to a WGM which propagates closest to the external MCF wall. WGMs with larger radial numbers which penetrate deeper into the capillary wall, as mentioned in section 1.2.1, will yield a smaller CWV owing to the negative thermo-optic coefficient of water, see Equation 3.3. Assuming the temperature variation $\Delta T_0 = 110°C$ we can find the fraction of power which would correspond to WGMs having different CWVs. It is difficult to discern this in Figure 3.2(c1) and (c2), as the CWV induced by the heating effect is faster than the temporal resolution of 1min. However viewing Figure 3.2(b), we can clearly see the longitudinal variation as MF1 approached the MF2 position. For CWs with higher radial numbers which have a smaller contrast (for example in the region between $\lambda = 1551$ and 1552 nm), we find a smaller CWV of $\Delta\lambda_{cw} = 1.02$ nm, corresponding to approximately $F_s = 0.97$ and $F_w = 0.03$. Furthermore, CW variations with much smaller contrast correspond to WGMs with even higher radial modes and, thus, much deeper penetration into water. Indeed, their CWV $\Delta\lambda_{cw}(z_{MF2})$ is negative and, therefore, $F_w > 0.1$ (see for example, those between $\lambda = 1546$ and 1548 nm).

Additional analysis by splitting the polarization modes, TE and TM, demonstrates three CWVs in each polarisation which are periodic. This suggests WGMs with p=0,1,2 are excited under the coupling condition of this experiment. Thus, the CWVs caused by heating can elucidate which radial mode is under observation as also suggested in [26]. It is also known that each polarization can interact with an optical material differently [86]. Further work to model the radial distribution of these higher WGMs as well as understanding the effect of polarisation on the CWV, could further our understanding of physiochemical processes at a solid-liquid interface.

3.3.2.2.4   Linear, non-linear and nonmonotonic evolution of spectra with time

The temporal spectrogram shown in Figure 3.2(c) shows the evolution of the CWs as a function of time at the MF2 position of $z = z_{MF2}$, during 12h of slow cooking. MF1 remained in contact throughout the experiment recording the power transmission every 1min. Overall we can see that all CWs are affected by the slow cooking process. The top axial eigenwavelengths of the WGMs, which are inferred to have radial number $p = 0$, is shown in Figure 3.2(c4), and indicates smooth linear growth of the CWV. The total growth of the CW over 12h is found to be $\Delta\lambda_{cw}(t = 12\text{h})\sim +0.4$ nm. On the other hand, CWs of higher radial modes demonstrate non-linear growth, see Figure 3.2(c3). The CW whose initial fundamental eigenwavelengths is $\lambda_{cw}(t = 0\text{h})\sim 1552$ nm, is shown to grow non-linearly, seemingly towards saturation. Moreover we can see non-monotonic growth of CWs of even higher radial modes leading to a negative CWV (see for example $\lambda_{cw}(t = 0\text{h})\sim 1552.6$ nm in Figure 3.2(c3)).

The probable reasons of the observed non-monotonic (positive and negative) CWV caused by the silica-water interaction (previously discussed in section 1.3), are summarized in Table 3.1. We hypothesize that the positive CW variation saturates with time due to the processes of volume expansion and structural relaxation. At the same time, competing processes which can introduce a negative CWV which includes the reduction in density, diffusion of water and formation of cracks at the MCF. Notably, higher radial modes which are localized closer to the internal MCF surface, i.e. at the silica-water interface, will be most affected by the processes associated with a negative CWV, strengthening our hypothesis. Additionally, the flow of water at the silica-water interface allow these interdependent processes to be continuous. Therefore, the positive and negative CWVs results from the competition of these processes and are demonstrably dependent on the local WGM distributions as well as temperature and time.

G. I. Gardosi, PhD Thesis, Aston University, 2022.

3.3.2.3 Formation of a permanent slow-cooked SNAP

The induced irreversible nonuniformities at the unheated MCF are shown in Figure 3.2(d), demonstrating the permanent SNAP formed after 12h of slow-cooking. The magnitude of permanent alterations are evaluated by comparing the CW profiles before and after slow-cooking, see the respective magnified spectrograms in Figure 3.2(a1) and (d1). For comparison, we applied the same heating power and time to an empty MCF, to find no perceptible changes to the CWs, see Figures 3.2(c1) and (c2), affirming that the irreversible alterations are a result of the silica-water interaction. Moreover, as shown in Figure 3.2(e), the induced CWV remained after we emptied the MCF from water and allowed it to dry for 12h. The CWs, of higher radial modes shift significantly after water is removed, see as an example the CWs in region of $\lambda_{cw} = 1550$ nm in Figures 3.2(d) and (e). This further confirms that these WGMs are localized close to the silica-water interface. Meanwhile the assumed $p = 0$ WGM, magnified in Figure 3.2(d1) and (e1), experiences a slight shift, contrary to our earlier assumption that $F_{cw}^{(w)} = 0$ for the lowest radial mode. We measure the shift ~ 70 pm at the same reference point on both spectrograms. If this were due to an ambient temperature change between experiments, it would correspond to $\sim 5°C$, much larger than the room temperature fluctuations which stay within $\pm 1°C$. Thus, the previously estimated temperature change $\Delta T(z_{MF2}) = 110°C$, may in fact be higher, since the negative thermo-optic coefficient of water would increase the estimated temperature albeit by a small amount. However, without modelling the radial distribution

Table 3.1 Summary of the origins of cutoff wavelength variation and their corresponding physical changes to refractive index, n and external radius, r. Unshaded cells indicate processes caused by hydrolysis and shaded cells indicate processes caused by hydration, as inferred by literature reviewed in Section 1.3.

CWV $\Delta\lambda_{cw}$	Process	Physical change n or r	Description
+	Volume expansion	r	Due to production of silanol groups.
	Structural relaxation	n & r	Promoted by water diffusion.
-	Reduction in density of silica	n	Breaking of silica glass bonds lowers refractive index of material via the interstitial voids created in the network.
	Compressive stress at crack tips	n	Compressive stress occurring at cracks with depth of at least 1 μm.
	Water molecule diffusion	n	Water has a lower refractive index than silica $n_w = 1.33$ and lower density $\rho_w = 1$ g/cm^3 (density of silica $\rho_s = 2.2$ g/cm^3)

of the WGM to determine its fraction within water, we assume it to be sufficiently small for our temperature estimation.

The induced permanent ERV is slightly decreased with the removal of water. We measure this change from the base of both resonators and find a 0.06 nm wavelength difference (discussed further in Section 3.5.2.1). Overall, using Equation 2.3 we find that the SMR height of $\Delta\lambda_{cw}(z = z_{MF2})\sim0.5$ nm is equivalent to an ERV of $\Delta r_{eff} =14$ nm. This is close to the typical ERV of 15 nm introduced by the CO_2 laser annealing method (see Table 2.1), which releases frozen-in tension of an optical fibre. However, further slow-cooking experiments have featured SNAP resonators with larger ERVs, up to 85 nm (see Section 3.5.2), indicating that the physical processes which causes the ERV in both these methods are not the same. Furthermore, the ERV created using CO_2 laser exposes the fibre to much higher temperatures for several seconds [1,11]. In contrast, the slow cooking method, introduces a resonator using a significantly lower temperature and over a much longer time. We suggest that the physical changes which generate this slow cooking phenomenon can be explained by the interaction processes between silica and water, which are summarized in Table 3.1, describing how each process may affect the refractive index or local radius measurable by the positive or negative CWV. In addition, we expect the flow of water inside our MCF due to the momentum transfer between the circulating WGMs and water [10], and due to the temperature gradient evident in Figure 3.2(b) and Equation 3.3 [87]. Water flows introduces fresh water at the silica-water interface, allowing the continuous reactions of hydration and hydrolysis in silica [11]. These continuous reactions induce the processes listed in Table 3.1. Thus, slow cooking, which generates both heat and water motion, may extend these processes beyond previous work at ambient temperature and pressure.

It is interesting to compare the temporal CWV found during the 12h slow cooking process, $\Delta\lambda_{cw} (t = 12\text{h})\sim0.4$ nm with the CWV found after heating is removed $\Delta\lambda_{cw}(z_{MF2})\sim0.5$ nm. This significant CWV increase, after heating ceases, suggests a post-cooking phenomenon, which will be explored further in the Section 4.3.

3.4   FORMATION OF A SLOW COOKED SNAP OVER DISCRETE DURATIONS

Although, monitoring of the CWV during the slow cooking process may not be useful in determining the final height of the permanent SNAP resonator, we can compare the permanent alterations after different slow cooking times, as shown in this experiment.

3.4.1 Experimental Procedure

We compare the permanent alterations caused by slow cooking over different time durations by re-heating the same MCF for total durations of 18, 40, and 57 hours. MF2 transmits the optical heating power of 63mW and is disconnected after each time interval. The unheated MCF is then measured between each slow cooking duration by translating MF1 along the MCF to characterize the permanent alterations with resolution $\Delta z = 30$ μm.
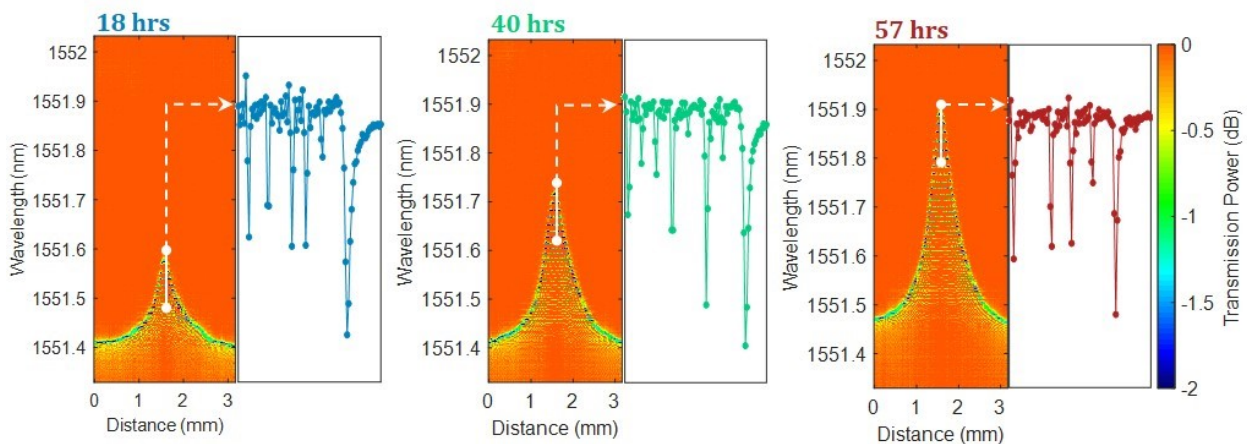
Figure 3.4. Spectrograms of permanently induced microresonators cooked over different time periods. (a)-(c) Left: spectrograms of the same MCF after slow cooking for total duration of 18, 40 and 57 hrs. Right: spectrum at the top CWs (labelled in white) of the corresponding spectrogram. From G. Gardosi et al., "Photonic Microresonators Created by Slow Optical Cooking," ACS Photonics (2021).

3.4.2 Results and Discussion

Figure 3.4. shows the permanent SMRs after varying slow cooking durations. We found an approximately linear growth between the time interval of 18 and 57 hours during which the average growth of the fundamental axial eigenwavelength is $\Delta \lambda_{cw} \sim 3\text{pm/min}$. Using the rescaling relation in Equation 2.3, we find the corresponding ERV fabrication precision of slow cooking to be $\Delta r_{eff} = 0.9$ Å/min. While this prevision is the same order of magnitude as the best slow cooking methods (particularly of CO_2 laser annealing), we demonstrate much better precision in the following chapter. In general, further work is needed to collect more data points on the SMR growth with time. Most importantly, the Q-factor was not found to degrade during the slow cooking process, within the 1.3 pm resolution of our OSA. The spectrums at the maxima position, z_{MF2} are shown to the right of each spectrogram in Figure 3.4., measuring a Q-factor exceeding $5 \cdot 10^5$. In addition, we can linearly rescale the profiles of the induced CWV to each other.

G. I. Gardosi, PhD Thesis, Aston University, 2022.

3.5 NONLINEAR FORMATION OF SLOW COOKED SNAPS

To understand the competition of the different processes which affect our CWV (summarized in Table 3.1 we present below two further experiments using a higher optical cooking power.

3.5.1 Experimental Procedure

We increase the optical power through MF2 to 100 mW to characterize the slow cooking phenomenon measuring temporal and permanent alterations of the MCF. In the first experiment, we create a SMR using 12h cooking time whilst measuring the spectral evolution at the MF2 heating position with temporal resolution $\Delta t = 1$min. We measure the permanent CWV at the unheated MCF introduced by slow cooking with spatial resolution $\Delta z = 10$ μm. First, we measure the water-filled MCF, then we measure the empty MCF after we inject air into the MCF and allow it to dry in ambient conditions for 23h. We repeat these measurements at the water-filled and empty MCF, allowing a longer drying time of 36h. In the second experiment we measure the same unheated MCF filled with water after total slow-cooking durations of 15h and 37h with spatial resolution $\Delta z = 10$ μm.

3.5.2 Results and Discussion

The temporal spectrogram in Figure 3.5(a), demonstrates the evolution of spectra at 100 mW of slow cooking power. Initially the processes which cause a positive CWV are dominant for all WGMs, i.e. the volume expansion and structural relaxation of the silica MCF. The lower radial modes demonstrate a linear CWV for the first 1.5h, after which, their evolution becomes nonlinear and seem to reach saturation after 12h of slow cooking with a total CWV of $\Delta\lambda_{cw}(t = 12\text{h}) \sim +2.5$ nm. In comparison, the total temporal CWV found in the earlier experiment using just 63 mW optical heating power is at least four times smaller. In fact, from Figure 3.2(c3) and (c4) we find $\Delta\lambda_{cw}(t = 12\text{h}) \sim 0.6$ and ~ 0.4 nm, respectively. Additionally, the spectra shown in Figure 3.2(c3) are not close to saturation after 12h. CWs of higher radial modes, shown in Figure 3.5(a) (identified by their lower contrast), begin with a nonlinear increase in CW, reaching saturation much earlier, after only 2h of slow-cooking. After saturation, the CWs decrease, indicating that the CWV is now governed by processes which generate a negative CWV such as a reduction in density, water diffusion and compressive stress at the silica wall. This behaviour is also observed using a lower power, as seen from the nonmonotonic evolution of higher radial modes in 3.2(c3). Unfortunately, we cannot infer whether water or hydroxyl diffusion rates into our silica wall are faster, since both their respective processes of hydration and hydrolysis can create positive and negative CWVs (see the shaded and unshaded cells of Table 3.1). However, it seems that increased optical power has accelerated the processes of the silica-water interaction. Our final resonator height measures at $\Delta\lambda_{cw}(z = z_{MF2}) \sim 3$ nm corresponding to an ERV of 85 nm, which is 6 times larger than the SMR measured using 63 mW over the same 12h slow cooking duration.

G. I. Gardosi, PhD Thesis, Aston University, 2022.
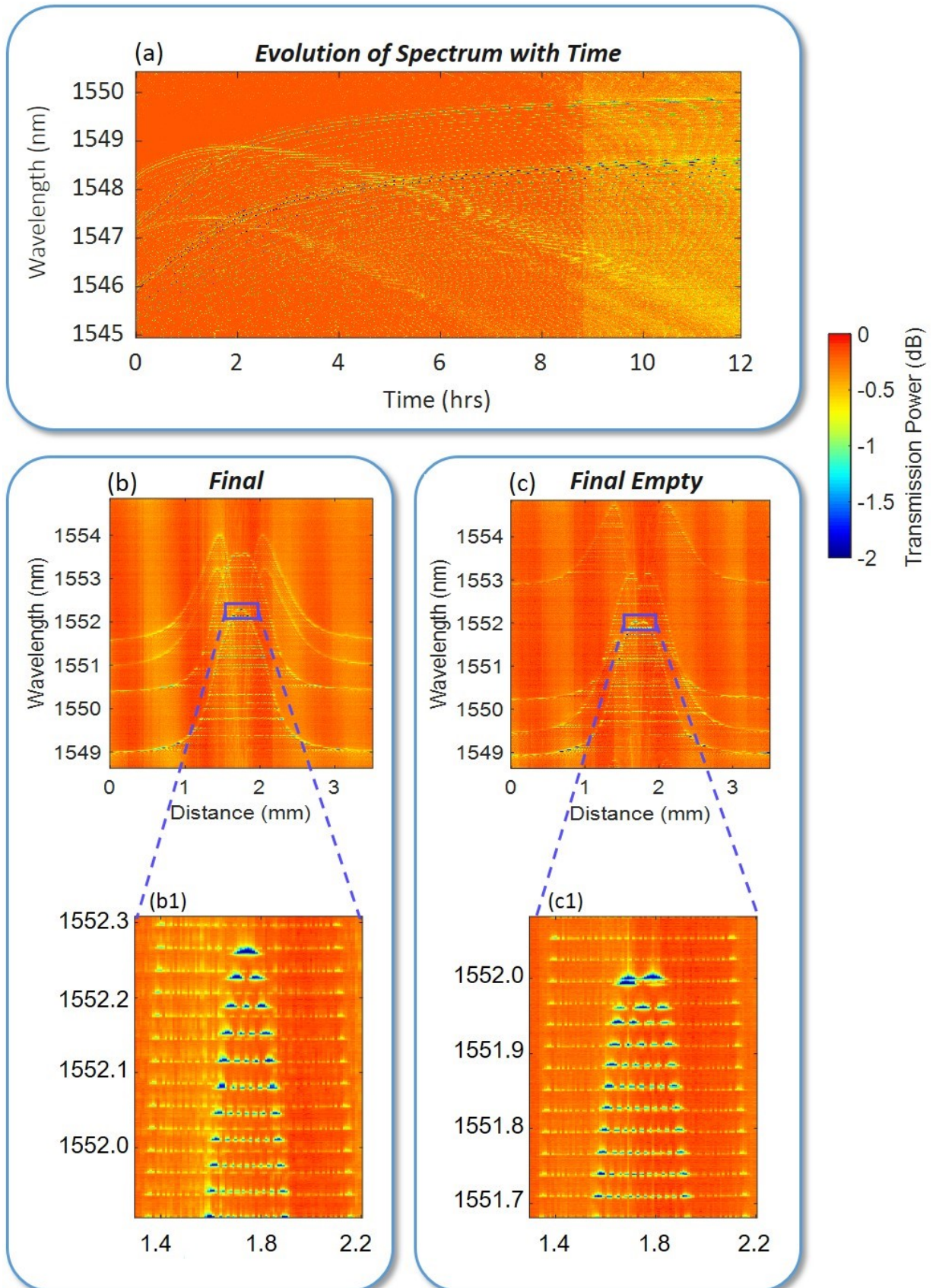
Figure 3.5. Slow cooking at higher optical power 100 mW. (a) Temporal spectrogram showing CWV during slow cooking. Evolution of some modes is non-monotonic after reaching saturation. After 9h there is background colour decrease due to taper degradation, though this does not affect our measurements of the CWV. (b) The spectrogram of the permanent alterations after slow cooking with magnified part shown in (b1). (c) The spectrogram after water is removed from the MCF and dried for 23h showing modification of the SMR with the removal of water with magnified part shown in (c1).

Given that the sensing region of higher radial modes is closer to the internal MCF wall [30], we hypothesize that the processes which produces a negative CWV would also eventually reach the sensing region of lower radial modes close to the external MCF wall. In other words, continued slow cooking would cause these low radial CWs to reach saturation and then decrease as we observe in high radial modes. In fact, we demonstrate a CW decrease for a lower radial mode in the experiment shown in Figure 3.6. After 15h slow cooking we find that the CW has decreased at the centre of the unheated SMR (the same position used for heating via MF2) for all WGMs. We can see that WGMs with higher radial quantum numbers are more strongly altered decreasing beyond the original MCF profile, and decreasing further with longer slow cooking time. Lower radial modes are less altered. We see in the magnified spectrogram shown in Figure 3.6(a1), that the CW at the heated position decreased to $\lambda_{cw}(z = z_{MF2}) \sim 1563.45$. Two SMRs are formed by this CWV depression, and the distance between their fundamental axial modes is ~ 0.4 mm. Then after more slow cooking with total duration of 37h, the negative variation further decreases, and we see from Figure 3.6(b1) that the fundamental axial modes of the two SMRs has widened to a total distance of ~ 0.6 mm.

Overall, from Figures 3.5 and 3.6, we find that slow cooking does not always cause a positive CWV. Rather, given sufficient time and slow-cooking power, all WGMs are observed to be affected by silica-water interaction processes which are associated with a negative CWV. Thus, the characteristic depth of the physical changes, due to the diffusion of processes within the silica wall, may be of micrometre order. Further experimental and theoretical work is needed to better understand the variations observed and the processes which have caused them.

3.5.2.1   *Microresonator modification with the removal of water*

Remarkably, in ambient conditions there is a stark profile change with just the removal of water, as shown in the magnified spectrograms of Figures 3.5(b1) and (c1). After water is removed and allowed to dry, the SMR splits into two. We repeat these measurements, adding and removing water again, which yields identical results. This significant SMR height change is measured about ~ 0.2 nm in wavelength. Notably the SMR height difference in our previous experiment with the removal of water was measured much less only ~ 0.06 nm (from Figures 3.2(d) and (e)). This indicates a reversible process at the silica-water interface. We suggest this decrease in CW is due to dehydroxylation of silica (see the backward reaction of Equation 1.1). As water is removed, the condensation of silica releases water, shown to occur at ambient conditions [13]. It is interesting that the SMR formed using a higher

G. I. Gardosi, PhD Thesis, Aston University, 2022.
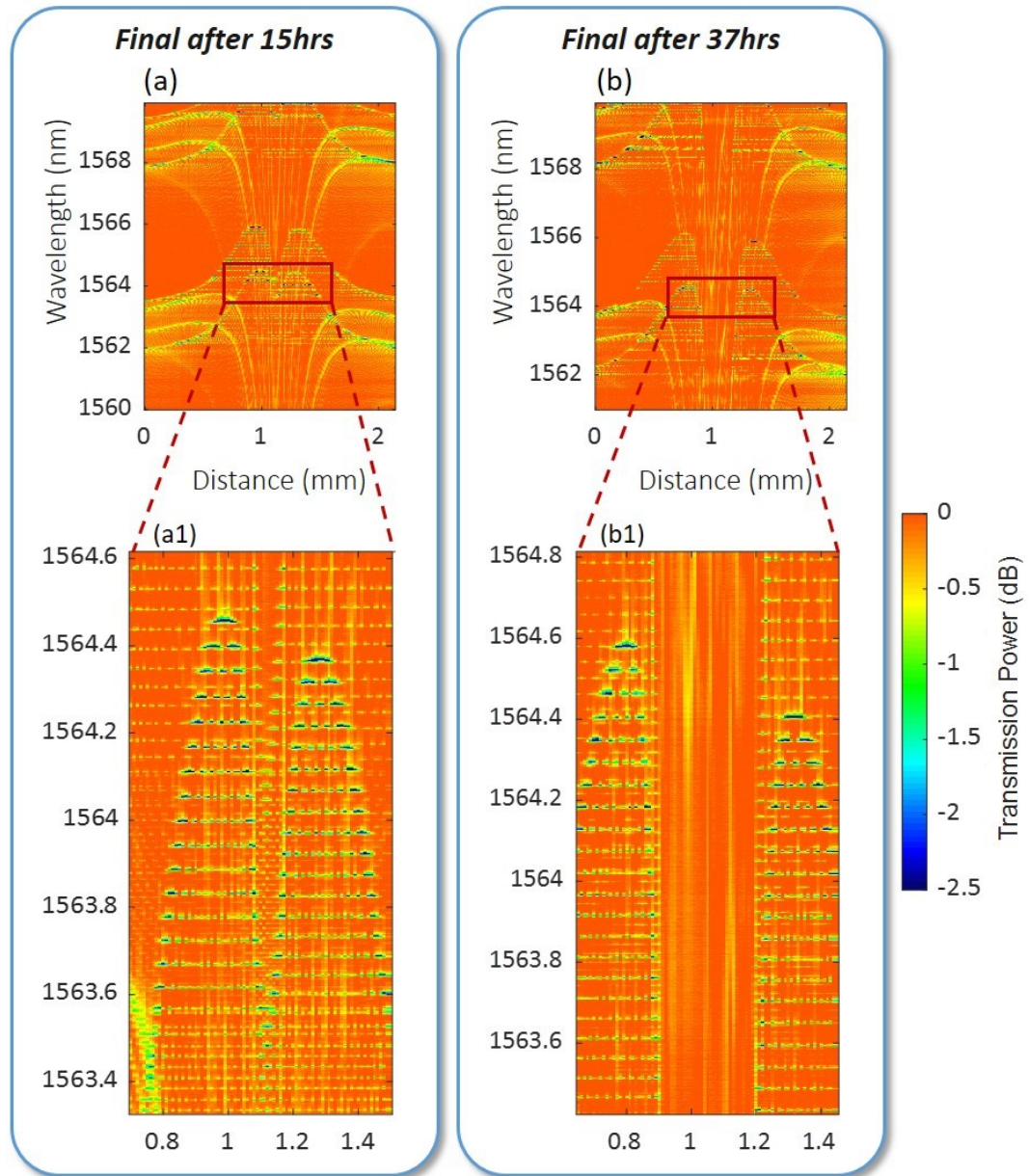
Figure 3.6. Spectrograms of an unheated MCF which has been slow cooked for total durations of (a) 15 hours and (b) 37 hours. Magnified spectrograms in (a1) and (b1) demonstrate the formation of two SMRs which widen with further slow cooking.

power has an increased sensitivity to this silica-water interaction. We suggest that the heightened sensitivity is caused by the formation of nanocracks [51,88] during the silica-water interaction. Nanocracks increase the number of reaction sites within our sensing region. Further investigation is needed to understand this increased sensitivity, but it reveals a promising technique for ultra-high sensing which may be capable of single molecule detection. Additionally, we can probe further, by taking temporal CW measurements to determine if this reversible process is time-dependent.

3.6 Conclusions & Outlook

We have presented a new method for the fabrication of SMRs, which simultaneously has utilities in the sensing of solid-liquid interfaces and of microfluidics. Our two MF experimental setup is relatively simple, using one MF for modification of a MCF and the other MF for the characterization of these modifications. This eliminates the need to transfer our sample across different setups, as required for the more complicated femtosecond laser inscription [80], HF acid etching [82] and tapering [4] fabrication methods, thus reducing risks of sample contamination. Additionally, to our knowledge, this is the first demonstration of microresonator fabrication using the ultra-slow silica-water interaction and a unique characterization technique to elucidate processes at the silica-water interface.

The slow cooking method applies optical heating, introducing a temperature variation at the MCF. Whilst transmitting 63 mW of optical power, we estimated that the maximum temperature of the MCF found at the heating MF position to be $T = 130°C$ (using silica's thermo-optic coefficient and by assuming a uniform radial distribution of temperature). Evidently the temperature found is above water's boiling point, nonetheless we observed that water remained in its liquid state throughout our experiments, warranting further investigation to understand this phenomenon. The induced temperature variation had a longitudinal distribution with an extent >5 mm along the MCF, creating a temporary resonator. The extent was found to be 5x larger than previous SMR thermal tuning methods, which locally heated a fibre using ohmic- [7] and laser-heating [8]. We hypothesize that our larger extent is because the evanescent tails of WGMs penetrate into and are absorbed by water to generate an internal heating effect distributed along the MCF. The temporary SMR disappears after heating ceases returning the CWs to its original profile. However, sustained heating caused irreversible alterations which created permanent SMRs.

We demonstrate the fabrication of a permanent SMR via slow-cooking with various heights of ERV $\Delta r_{eff}(z_{MF2}) =$14 nm and $\Delta r_{eff}(z_{MF2}) =$85 nm at the heating MF position, by transmitting optical heating powers of 63 and 100 mW respectively. The latter is significantly larger than the commonly used CO_2 laser annealing method, establishing slow-cooking as a flexible fabrication technique. The SMR formation exhibits approximately linear growth between the time interval of 18, 40 and 57 hours of slow cooking using 63 mW optical power. During this time we calculated the average fundamental axial eigenwavelength growth to be $\Delta\lambda_{cw}\sim$3pm/min, which corresponds to an ERV precision of $\Delta r_{eff} = 0.9$ Å/min (we improve this precision by two orders of magnitude in the following chapter). Favourably, our Q-factor of our fundamental axial mode was not found to degrade during these intervals, achieving $Q > 5 \cdot 10^5$ limited by our OSA resolution.

We propose that the creation of a permanent SMR is due to processes of the silica-water interaction originating at the internal MCF wall, via the hydration and hydrolysis of silica [39,49,53,58–60,64,71,72]. The unceasing modification of the MCF indicates that our slow-cooking method also generates water motion [10], since fresh water introduced to the silica-water interface allows the continuous reaction of these processes [39]. During our modifications, we observed that the CWV of different WGMs do not always demonstrate linear growth with time. We know that WGMs of higher radial modes penetrate deeper into the MCF towards its centre [19,30]. The WGMs observed in our experiments, which were identified to have higher radial modes, demonstrated a nonlinear evolution in CWV with time. Whilst, the WGMs identified to have even higher radial modes demonstrated nonmonotonic evolution. Over time, the CWVs were found to increase, reach saturation and then decrease. We suggest that these observations demonstrate the competition of silica-water interaction processes whose physical changes give rise to both positive and negative CWVs. Higher cooking powers seem to accelerate these processes since the positive CWV reached saturation much earlier than observed at a lower cooking power. We consider therefore, that given sufficient slow cooking power and duration, all WGMs will follow this nonmonotonic evolution. Unfortunately, we cannot separate the processes to infer whether water or hydroxyl diffusion rates are faster since both their respective processes can cause positive and negative CWVs (summarized in Table 3.1). However, further work using different cooking powers and durations, and dehydrated silica may elucidate more about the silica-water interaction, which until now has been challenging to measure at ambient conditions. In addition, modelling the radial distribution of these higher WGMs as well as splitting the polarisation, to restore the CWVs observed, can advance our understanding of the slow cooking phenomenon.

We also demonstrate a reversible reaction at the silica-water interface with the simple removal of water from the MCF. Removing water reduced our permanent SMR height, found most significant at our SMR with larger ERV formed using 100 mW. In this case the SMR split into two SMRs when water was absent and the reconfiguration was repeatable with the addition and removal of water. We think that the reversible process is re- and de-hydroxylation of the silica-water interface known to occur at ambient conditions [13]. The heightened sensitivity may be due to the formation of nanocracks [51,88] during the silica-water interaction, which increases the reaction sites of this process. Alternatively it may be due to enhancement of the evanescent field which occurs with the addition of a high refractive index layer [17], which we suggest was caused by silica-water processes. In general, this reveals an ultra-high microfluidic sensing technique that could be developed for single-molecule detection.

In summary, the discovered slow cooking method has demonstrated to be an experimentally simple, flexible and precise fabrication method for microresonators on the SNAP platform. In addition, it opens new possibilities for the sensing of complex physical, chemical and mechanical processes at the silica-water interface at ambient conditions. Further work to characterize the slow cooking phenomenon, include variation of the slow cooking power and heating MF coupling condition, acquisition of more data points during slow cooking growth, and theoretical modelling of WGM radial distributions. Finally, we can broaden the scope of slow cooking by incorporating other solid materials, e.g. by adding a nanoscale coating at the silica MCF internal wall, or by using other liquids, e.g. aprotic, colloidal and of varying pH.

4   Picometre Fabrication Precision

4.1 Introduction

A key area of development in microphotonics technologies is the precise fabrication of photonic devices. Developed modern technologies are capable of measuring the surface displacement and profile with exceptional picometre scale precision [89,90]. However, commercial fabrication methods in state of the art microphotonics, achieve precision of only several nanometres, two orders of magnitude worse than the precision of sensing. Various microphotonic applications necessitate a higher fabrication precision including for the creation of resonant photonic devices for optical signal processing such as frequency comb generators, dispersion compensators and delay lines [3,5,91–93]. WGM microresonators are befit to achieve this high precision because any relative change is effectively averaged over the volume of the propagating WGM with characteristic dimensions in the order of the wavelength of light. Thus, picometre fabrication precision in wavelength can be attainable. Several emerging methods to precisely control the size of optical resonators include microlithographic fabrication [94], and post-fabrication trimming [92]. The former process is complex, performing very accurate etching over a relatively large surface area. Development of this technique to achieve picometre-scale precision would be a challenging problem. The latter tunes the resonant wavelength of the microresonator via waveguide doping [92,93], which adversely affects its Q-factor. In addition, their method, which enables postprocessing of multiple independent microresonators [92], is more complicated when applied to coupled resonator circuits [93].

Comparatively, the SNAP platform which works well for coupled resonator circuits [11,74], has developed two straightforward post-processing methods to permanently position the resonance of fabricated optical resonators. Both use multiple fast laser exposures of a fibre via either a CO_2 [11,74] or femtosecond [12] laser. However, their sub-angstrom precision in ERV correction, are poorly reproducible, requiring numerous iterative attempts, and, are limited by their processes which modify silica. The CO_2 laser method, releases frozen in tension from fibre's drawing manufacture, while the fs laser method introduces internal stress via laser inscription. In particular the fs laser's maximum postprocessed ERV reached only 8.0 Å [12].

On the other hand, the slow cooking method exploits the ultra-slow silica water interaction to permanently change the ERV of a SMR. In the previous chapter, we generate resonator heights ranging 14-85 nm in ERV from 12h of slow cooking fabrication. Here, we further our investigations for precise resonator size control. We present precision experiments in: the post-processing of a SMR using short

slow cooking times (minutes), the temporal evolution of our resonator after slow cooking and the effects of coupling on optical heating.

4.2   PICOMETRE PRECISION IN POST-PROCESSING OF A SLOW COOKED SNAP MICRORESONATOR

Our previous experiments used multi-hour-long slow cooking durations to fabricate a SMR at a silica MCF. We demonstrated that during optical heating, generally the CWV varies nonlinearly in time, however, over shorter durations and moderate cooking power, the CWV can be linear (see Sections 3.3.2.3 and 3.5.2).   The following experiment probes this exceptionally slow fabrication technique using much shorter minute-long slow cooking durations to determine whether we can controllably post-process a SMR with picometre order variation of its CW.

4.2.1   Experimental Procedure

We use the same experimental setup previously described in Section 3.2. First, we fabricate a SNAP microresonator (SMR) using the slow cooking method. This initial SMR is then postprocessed using 56 mW optical power at 1h discrete durations. The measured spectrograms are made after each 1h slow cooking steps with spatial resolution $\Delta z = 10$ μm, and are wavelength adjusted relative to a chosen reference CW at 2.5 mm away from the SMR. This reference CW is chosen to be sufficiently away from the SMR to be unaffected by irreversible alterations created by slow cooking, and therefore accounts for any ambient temperature variations during spectrogram measurements. Throughout the experiment, MF2 remains in contact with the MCF, to ensure the local heating position remains the same.

We continue the investigation by slow-cooking an additional two microresonators, SMR1 and SMR2, using 100 mW optical power for 3.5h. Next, we postprocess the SMRs to equalize the fundamental axial eigenwavelengths by translating MF2 between SMRs using three iterations. These iterations involved slow-cooking of (1) SMR1 for 10mins, (2) SMR2 for 5mins and finally (3) SMR2 for 10mins.

4.2.2   Results and Discussion

Figure 4.1(a) shows the spectrogram of the initial SMR at 0h, alongside the subsequent spectrograms made after each 1h slow cooking duration. We illustrate the temporal linearity of the first seven axial eigenwavelengths with straight black dashed lines. A closer look at the linear growth of the first three axial eigenmodes are graphed in Figure 4.2. The CWV, $\Delta\lambda_{cw}$, is calculated relative to the CW reference for each of the 0-5h spectrograms. The axial eigenwavelengths are identified from their spectrums, taking the resonant dips of largest extinction ratio and lowest wavelength. Vertical error bars show the OSA resolution ± 1.3 pm, and the linear trends are made by setting the intercept to $\lambda_0(q)$
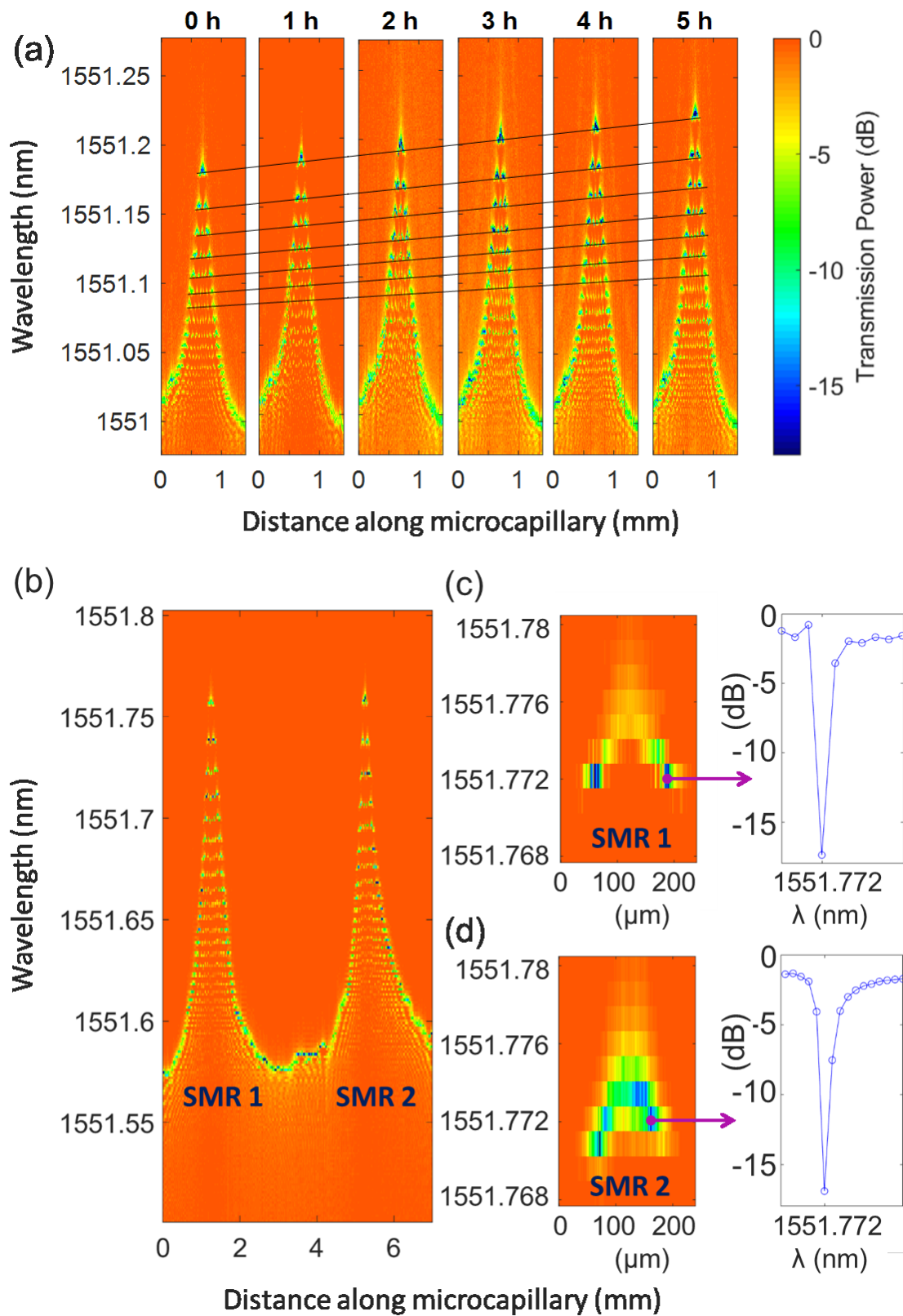
Figure 4.1. (a) Spectrograms of an SMR post-processed at 1h intervals. (b) Spectrogram of SMR1 and SMR2 fabricated at the same MCF. (c) and (d) Spectrograms of the final post-processed fundamental axial eigenwavelengths of these SMRs with their spectra to the right.

G. I. Gardosi, PhD Thesis, Aston University, 2022.

measured at 0h for each respective axial eigenwavelength, $q = 0, 1, 2$. The linear trends demonstrate temporal linearity that is subpicometre per minute, but the growth is non-uniform for $q = 0,1,2$, at 0.15 pm/min, 0.13 pm/min and 0.12 pm/min respectively, which corresponds to an ERV precision of $\Delta r_{eff} \sim 3$ pm/min. The largest residuals found at 60mins deviate by a maximum of 2.4 pm from our trend within the 1.3 pm resolution of our OSA. This deviation is unaccounted for and may be an experimental error since ambient temperature variations between spectrogram measurements were considered using our CW reference. It is possible that there was a temperature change during the spectrogram measurement. If so, this relates to a 0.2 °C ambient shift (using the thermo-optic coefficient for silica in Equation 3.1) during the 30mins of MF1 translation between the CW reference and SMR. Overall, the eigenwavelength growth was found at ~ 10 pm/hr.

The next experiment postprocessed two SMRs shown in Figure 4.1(b). The eigenwavelengths were measured on the right-side of the fundamental axial eigenmode. After their fabrication, the initial fundamental eigenwavelengths of SMR1 was found to be just 1.3 pm smaller than SMR2. This fortifies slow-cooking as an ultra-precise fabrication method since application of the same cooking durations developed strikingly similar SMRs. After three iterations of post-processing we achieve equal eigenwavelengths within the 1.3 pm resolution of our OSA measurement. The results are presented
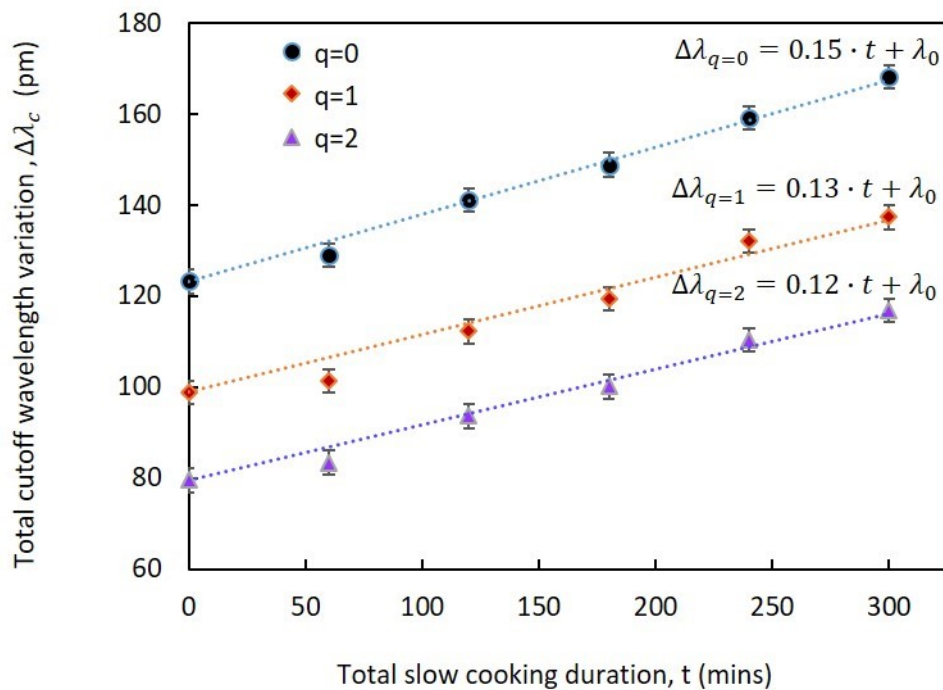
Figure 4.2. Total growth of the first three axial modes, $q = 0,1,2$ at 60mins intervals over 5h with relative to a relative feature displaced from the affected slow-cooking region. Linear trends show the growth in pm/min with intercepts from their respective cutoff wavelengths for each axial quantum number $\lambda_0(q)$ from the pre-fabricated SNAP microresonator at $t = 0$. Vertical error bars show the ± 1.3 pm resolution of the OSA.

by the magnified spectrograms in Figures 4.1(c) and (d) which include plots with the corresponding transmission dips shown to the right. Surprisingly, we do not observe a reduction in Q-factor after postprocessing. We estimate $Q > 10^6$ within the resolution of our OSA.

The two described experiments used different heating optical powers and coupling for postprocessing of the SMR. However, a brief comparison shows that the estimated 0.15pm/min growth precision of the fundamental axial eigenwavelength of the first experiment, can be directly related to our second experiment which demonstrated $\sim$1.3 pm/10mins. Splendidly, the growth over the longer 10mins is almost 10 times larger than predicted over 1min, demonstrating slow-cooking as a robust method for ultra-precise fabrication.

Furthermore, we suggest we may introduce predetermined complex profiles by programmed translation of the heating MF2. Given the characteristic CW growth of $\sim$0.1 pm/min from Figure 4.2, and assuming that 10secs is sufficient for both temperature stabilization and MF translation at the MCF, we estimate a possible accuracy of permanent CWV as high as 0.02 pm/10secs. Notably, the axial translation of MF2 may require disconnection from the MCF to avoid stiction, in which case the longitudinal fabrication precision will also be dictated by the repeatability and accuracy of our translation stages. To this end we test our current setup in Appendix E. Nonetheless the Lorentzian profile of the permanent alterations introduced at the MF2 fixed position can be considered as a building block to generate a plethora of predetermined shapes for applications in microphotonic devices reproducible within the resolution of our OSA and within the accuracy of our MF translation stages. Further work should introduce a temperature control since our OSA resolution is sensitive to even 0.1°C shift in ambient temperature. Overall, the slow cooking method demonstrates an ERV precision of 0.36 Å, limited by the resolution of the OSA. Previous SNAP post-processing methods bettered our resolution only due to the use of fibres with a smaller diameter, thus decreasing the corresponding ERV resolution using the same OSA.

4.3 POST-COOKING PHENOMENA

Previous experiments showed that the CW evolution whilst heating measured significantly less than the final observed CWV at the unheated MCF. For example, in Section 3.3.2.3, we observed a 0.1 nm difference between the temporal CWV and the final resonator height. This difference indicates an additional process which further modifies the CW after heating ceases. Below, we explore the CWV immediately after the slow cooking process by taking rapid spectral measurements to find a post-cooking effect. The following results were conducted in the interims of the post-processing at the two SMRs presented in Section 4.2.

G. I. Gardosi, PhD Thesis, Aston University, 2022.

4.3.1   Experimental Procedure

The same two fabricated SMRs are post-processed as described in Section 4.2.1. Each SMR is post-processed using 100 mW for 10mins. After heating ceases, SMR1 is refilled with water via the syringe epoxied to our MCF, as was procedural in our slow-cooking experiments. Then, we measure the alterations to the CWs by taking rapid spectrums with MF1 positioned at z_{MF2}, over 4h with temporal resolution $\Delta t = 2$ secs. We repeat this process at SMR2; this time after heating ceases, we do not re-fill the MCF, leaving the water inside it undisturbed. We start the recording of the temporal spectrograms as hurriedly as possible. Nonetheless, there is a time delay between the end of heating and the start of measurement of 2m48s for SMR1 and of 1m10s for SMR2.

4.3.2   Results and Discussion

Figure 4.3(a) shows a large bandwidth spatial spectrogram of the two SMRs at the MCF, which were post-processed. After heating ceased we observe a positive CWV in all WGMs for both SMR1 and SMR2, whose growth is so small it is hardly perceptible in Figure 4.3(b) and (c). However, we can see that the evolution of higher radial modes, appearing here as thick green bands, are different in each SMR. Referring back to Figure 4.3(a), we see that these lower contrasted modes with a negative CWV differ at each SMR. The varied slow-cooking durations during our post-processing generated picometre scale changes in wavelength to our SMRs at this low radial mode and much larger variations at higher radial modes. In addition, their thickness signify a decrease in the Q-factor, typical of higher radial modes.

Focussing on our low radial mode, we magnify the same WGM analysed in Section 4.2.2, shown in the black boxes of each temporal spectrogram. We can clearly see nonlinear evolution of the fundamental axial eigenmode over the 4 hour experiment, which measures $\Delta\lambda_{cw}(t = 4h) = 14.1$ pm for SMR1 and $\Delta\lambda_{cw}(t = 4h) = 11.6$ pm. Considering that our OSA resolution is ± 1.3 pm the CWVs are not distinctly different at each SMR. However, the measurements for SMR1 began over 1min30s later than for SMR2 and given the steep rise in CW after heating ceases, we consider that SMR1 does have a larger CWV, revealing that refilling the MCF increased the post-cooking effect. However, further experimentation is needed to conclude whether introducing fresh water after slow-cooking generates a larger CWV.
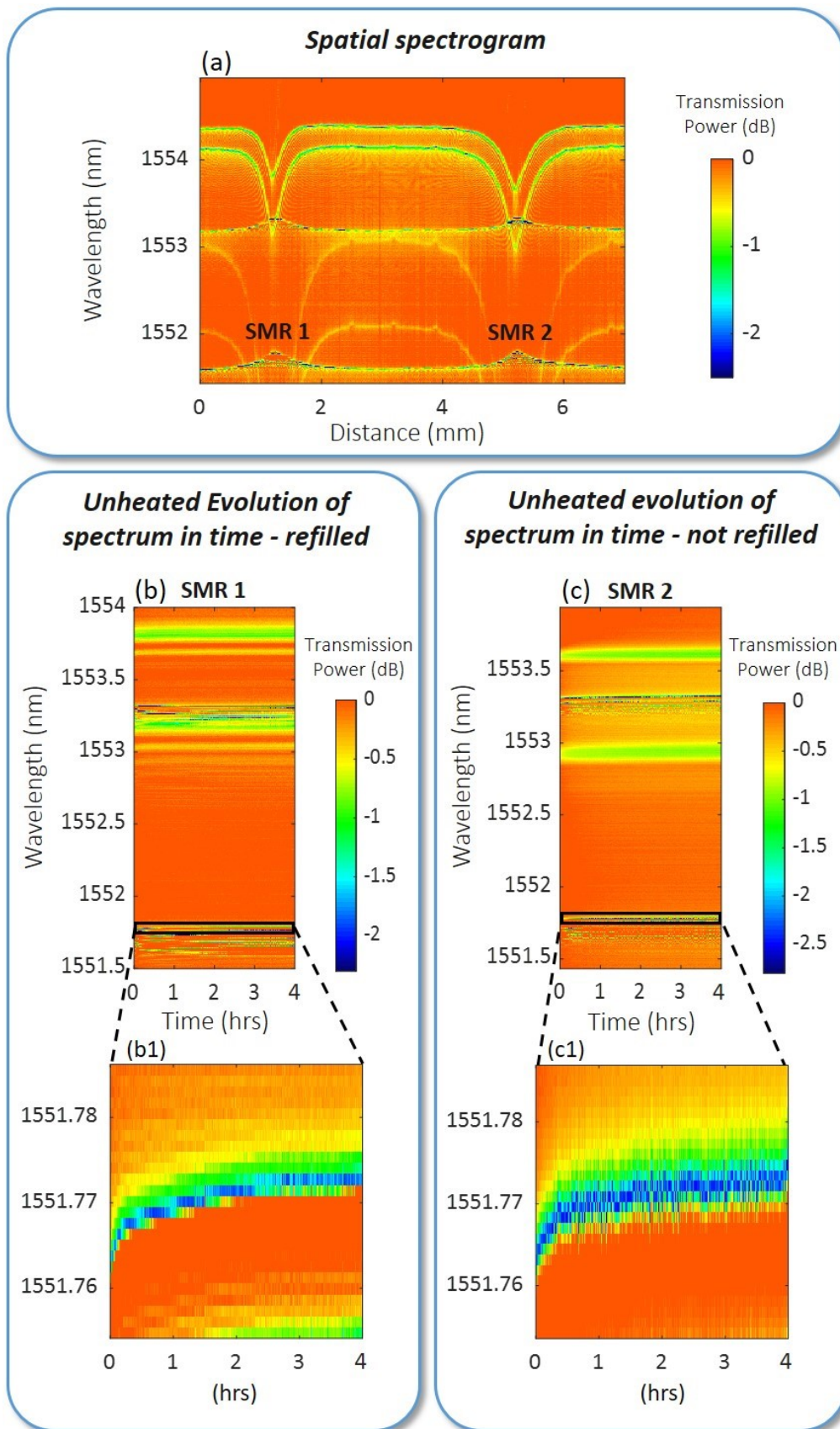
Figure 4.3. (a) Large bandwidth spatial spectrogram of two SMRs at a water-filled MCF. (b) and (c) show the temporal spectrograms measured at z_{MF2}, directly after post-processing SMR1 and SMR2 respectively, with temporal resolution $\Delta t = 2secs$. (b) shows the post-cooking variations found at SMR1 after refilling the MCF with water. (c) shows the same without refilling fresh water into the MCF. (b1) and (c1) are magnified spectrograms at the fundamental axial eigenmode of SMR1 and SMR2.

Overall, the CWV measured $\Delta\lambda_{cw}{\sim}10$ pm is an order of magnitude smaller than the difference measured between the temporal and final resonator height ~100 pm. Thus, further work is needed to understand this disparity, including, an experimental procedural which has no time gap between the rapid temporal measurements after the slow cooking heat is switched off. Nonetheless, we find that the post-cooking effect increases our CWV and saturates in a matter of hours at ambient conditions. This opposes the shrinking of our resonator height with the removal of water made in Section 4.1 which was also observed in ambient conditions. Instead, here water remains in the MCF, and the CWV occurs immediately after ending the thermal and mechanical perturbations induced by slow cooking. Therefore, we suggest that this observation demonstrates the structural transition of the silica glass state, namely its relaxation. Until now, examination of silica's relaxation has required years at ambient conditions [62] or has required extremely high temperatures (over $1000℃$) [63] to become measurable.

Hence, further investigation of the post-cooking effect has the potential to have noteworthy impact on the understanding of silica's relaxation which surpasses the detection limits from previous methods. Consequently, the observed post-cooking phenomenon is important for the ultra-precise slow cooking fabrication of microresonators, since hours must pass before measuring the final resonator profile. In addition, further work is needed to uncover the durability of slow cooked microresonators by measuring their stability over longer time periods, such as weeks and years.

4.4 MAXIMUM TEMPORARY SPECTRAL SHIFT THROUGH COUPLING OPTIMIZATION

A MF's diameter reduces adiabatically to its thinnest region (the taper waist) to maintain a high optical power transmission. Until now, in our slow-cooking procedure, the contact point of the heating MF2 was arbitrarily chosen along our taper waist, provided that it led to excitation of the heating WGMs in the over-coupled regime, commonly employed to improve the stability of a coupler-microresonator system. However, within this regime we may vary the MF2 contact position along its length, and, thus affect the power coupled into our MCF. In the simplest description ignoring scattering losses, coupling at the thinnest point of a taper waist, increases the optical power available for WGM heating. Therefore, this experiment is conducted to determine the coupling position which generates the maximum temporary CWV induced by optical heating.

4.4.1 Experimental method

We use the same experimental setup as described in section 3.2. MF1 makes contact with the water-filled MCF at a fixed z-position 5 μm away from MF2. We translate MF2 along the taper waist length (the thinnest region of the MF) in the y-direction shown in Figure 4.4 to vary the coupling which causes
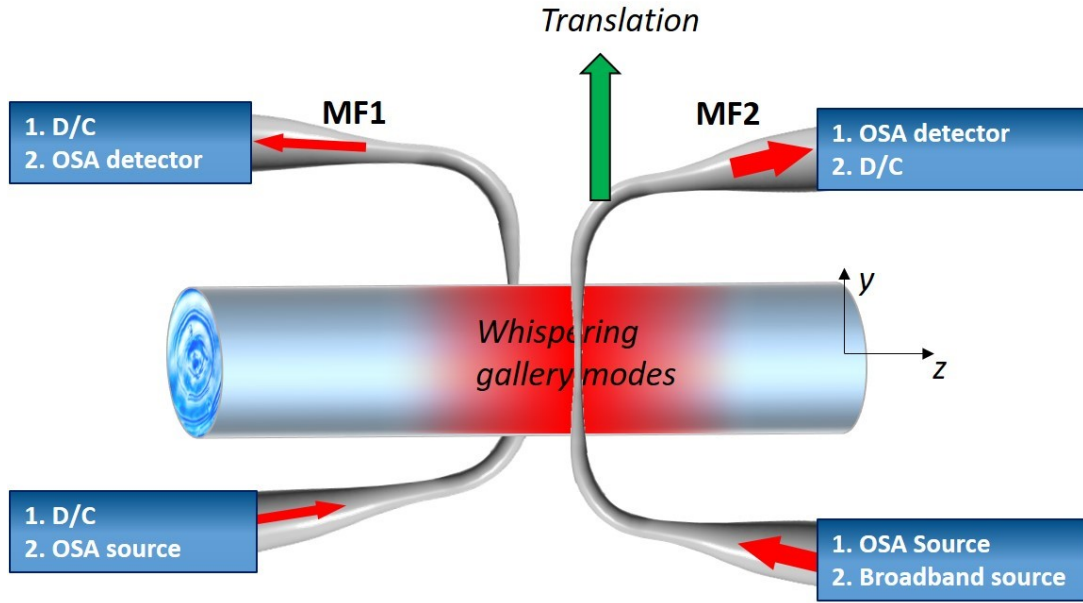
Figure 4.4. Experimental procedure. First MF1 is disconnected and MF2 is connected to the OSA source and detector. Second MF2 is connected to the broadband source to generate a heating effect by WGMS, which is measured by MF1 connected to the OSA source and detector. MF2 is translated along Y to contact the MCF at different positions along the taper waist axis.

the reversible CWV. At the first stage, the input-output MF2 is connected to the OSA source and detector to measure the transmission power over a bandwidth of 1525-1611 nm. This bandwidth is comparable to our heating source bandwidth of 1530-1610 nm. The total power loss via MF2 is analysed by subtracting spectral measurements made in and out of contact with the MCF to find the loss as a function of wavelength,

$$P_L(\lambda) = P_T^{(out)}(\lambda) - P_T^{(in)}(\lambda). \tag{4.1}$$

Integrating across our measurement bandwidth from λ_a to λ_b, gives us the total power lost at the MF2 coupled y-position,

$$P_L^{(Total)} = \int_{\lambda_a}^{\lambda_b} (P_L(\lambda)) \, d\lambda \ .$$

At the second stage, we disconnect the OSA from MF2 and connect it to MF1. Simultaneously, we connect the input of MF2 to the broadband heating source which excites WGMs to generate heating using optical powers of 100, 75 and 50 mW. We measure the thermally shifted CW, $\Delta\lambda_{cw}$ by taking spectrums of the unheated and then heated MCF by switching on the heating source,

G. I. Gardosi, PhD Thesis, Aston University, 2022.

$$\Delta\lambda_{cw} = \lambda_{cw}^{(HTD)} - \lambda_{cw}^{(UNHTD)} \, , \tag{4.2}$$

where $\lambda_{cw}^{(HTD)}$ and $\lambda_{cw}^{(UNHTD)}$ are the heated and unheated CWs of the same quantum numbers $cw = q, m, p, s$. Finally, we vary the coupled y-position of MF2 by its perpendicular translation relative to the MCF, in 0.5 mm steps, and repeat the process from the first stage.

4.4.2   Results and Discussion

The spectrum of power lost, $P_L(\lambda)$, when contacting MF2 to the MCF is shown in Figure 4.5(a). In agreement with Equation 4.1, resonant dips of the excited WGMs are flipped, displayed here by the spectral peaks. The overlap and large FWHM of the peaks indicate the over-coupled regime throughout the experiment. We integrate across the OSA bandwidth to find the total power lost via MF2 at this coupled position. Indeed, scattering losses at the coupled region increase with power and our heat source power is two orders of magnitude greater than our OSA (0.2 mW). However, we assume that this does not significantly affect our characterization of the coupled position. Therefore, we postulate that all power lost via MF2 is coupled into WGMs.

The CW increases when the heating source is switched on as shown with the black arrow in Figure 4.5(b). The unheated spectrum (see red curves) were measured at each y-position, with our CW $\lambda_{cw}^{(UNHTD)}$ identified at the resonant dip of our chosen WGM (see crosses). The CW increases after heating is applied, dependent on the position of coupling (each coloured curve indicates a different y-position). The formed temporary resonator is evidenced by the multitude of resonant dips from the heated spectra. We select the fundamental axial eigenwavelength, $\lambda_{cw}^{(HTD)}$ (see circles) to calculate the thermal shifts $\Delta\lambda_{cw}$ using Equation 4.2.

Figure 4.5(c) compares the measured total power and corresponding wavelength shift as a function of the MF2 y-coordinate acquired in 0.5 mm steps away from an arbitrary contact position. The reversible CWVs, $\Delta\lambda_{cw}$ introduced by optical heating follow similar trends at each position of coupling and are found to be linear with power between the range of 50, 75 and 100 mW. The maximum CWV found at $y = 0.5$ mm, corresponds to a temperature change calculated using Equation 3.1 (setting $F_{cw}^{(s)} = 1$ and ignoring radial expansion) shown in the data labels on the blue, orange and yellow curves. Considering the room temperature was $\sim 22°C$, we find the maximum temperature at the MCF using 100 mW to be $\sim 140°C$. However, liquid water remained in the MCF throughout the experiment (previous discussion on water remaining in liquid state above its boiling point can be found in Section 3.3.2.2.2). Curiously, the y-position for total transmission loss of MF2 does not coincide with the

maximum CWV. Instead, the largest power loss is found 1 mm away from the maximum CWV position at y = 1.5 mm.

There are two main lines of inquiry following our finding: A. Does the maximum power lost via the MF correspond to the largest broadband power available to generate a heating effect? And, B. Does the CWV only represent the temperature change during optical heating? Are there other physical
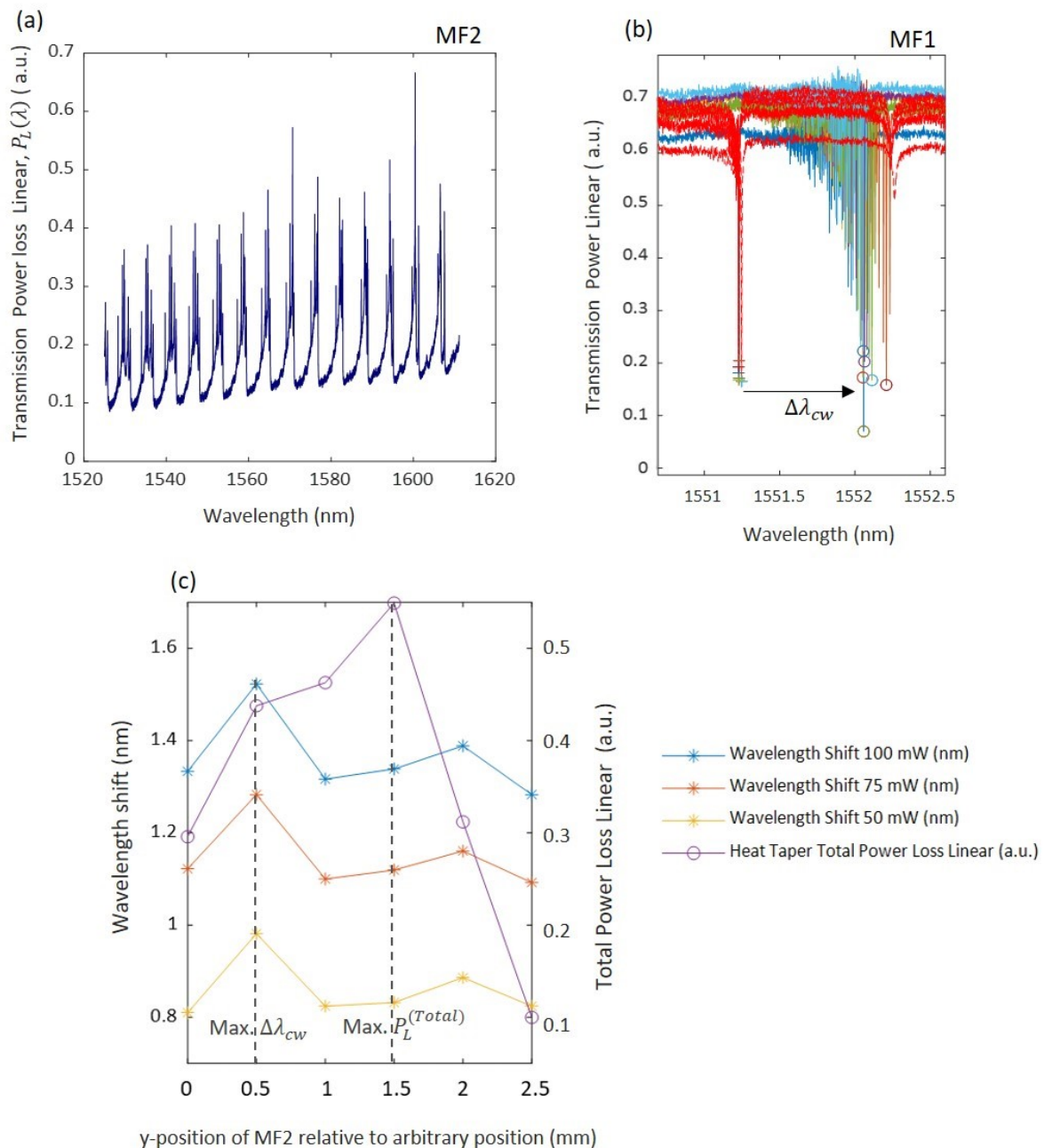

Figure 4.5. (a) Large bandwidth spectrum of a MF2 contact position at the taper waist. (b) Thermal spectral shift of a CW observed during 50 mW optical heating. The red curves show the unheated spectrums with the initial CWs labelled by crosses. The other coloured curves show the heated spectrums at different coupling y-positions with the thermally shifted CWs labelled by circles. (c) The CW shifts due to different MF2 coupling positions at optical heating powers of 100, 75 and 50 mW, compared with the total transmission power loss via MF2. Dotted lines on the graph indicate the positions which yield maximum values, which are not coincident.

processes causing an index change? Assuming A is affirmative, we can probe inquiry B using previous work demonstrating water motion due to the WGM momentum transfer [10]. First, we may disregard our previous assumption of a uniform temperature distribution at the MCF cross-section (see Equation 3.1). We know that momentum transfer occurs at a resonance and the induced speed increases linearly with power as demonstrated in [12] (see Figure 1.7(a)). Fluid mixing takes heated water away from the sensing region close to the internal wall of the MCF. Thus, at the coupling position where maximum power is lost into the MCF, we simultaneously induce an increase in temperature due to water absorption, and a decrease in temperature due to fluid mixing at the sensing region. These competing physical processes could explain why the maxima between our CWV and total power loss are not found to be coincident. In addition, our experiments do not test if water motion affects the refractive index contributing to the CWV.

It is known that in the over-coupled regime, a circulating WGM experiences an enhancement of intensity which peaks at critical coupling. On the other hand, over-coupling excites higher radial modes that penetrate deeper into the MCF wall. Also, the coupling condition is dependent on the radial mode, i.e. the MF coupled position for critical coupling to a lower radial mode is not the same for higher radial modes [95]. Exploration of the effects of coupling on the CWV can help to optimize our slow cooking method, and to better understand the WGM interaction with fluids. Finally, we have found during our experimentation that the permanent alteration at the silica-water interface occurs only above a threshold power. Therefore, to separate any CWV induced by the silica-water interaction, further work should use optical heating powers below this threshold.

4.5 CONCLUSIONS

Our slow cooking fabrication method is capable of introducing picometre increments of CW reproducibly and within experimentally appropriate time periods. We achieve eigenwavelength matching of the fundamental axial modes at two SMRs by post-processing. Our corresponding ERV precision of 0.36 Å is at the same order of magnitude as other developed post-processing techniques on the SNAP platform [11,12]. However, since our technique is exceptionally slow, and our measurements were limited by our OSA resolution, we deem our method feasible of sub-picometre resonant wavelength control. Furthermore, we suggest that we may create resonators with predetermined complex profiles by programmed translation of the heating MF2. Our results indicate that we may introduce smooth Lorentzian-shaped alterations with an estimated precision as high as 0.02 pm per 10secs of optical heating. Thus, slow cooking is a highly promising technique for the precision manufacture needed to create a diverse range of microphotonic devices such as delay lines, dispersion compensators and frequency combs [3,5,91–93].

Nonetheless, further work to characterize the slow cooking technique is required to arrive at a robust approach for ultra-high precision fabrication. Firstly, the observed post-cooking effect, which was found to vary our CW after optical heating by $\Delta\lambda_{cw}{\sim}10$ pm, needs to be factored into our procedure. In addition, the durability of our SMRs fabricated using the silica-water interaction should be tested over several weeks or years. Also, the coupling condition of our heating MF has been shown to contribute to the temporary CWV, and thus, may affect the permanently introduced CWV. Ideally, further work will relate the temporary CWV, which may be monitored during our slow cooking procedure, and the induced permanent CWV.

In general, our investigations to perfect the slow-cooking fabrication technique simultaneously serves to elucidate the silica-water interaction processes. In particular the relaxation of silica [62,63], observed during the post-cooking effect, and the nanocracks [51,57] formed by silica's hydrolysis. The heightened sensitivity of our resonator profile with the removal of water from our MCF, provides a promising avenue for future ultra-high microfluidic sensing, capable of single molecule detection.

5   FUTURE WORK & CONCLUSIONS

5.1   FUTURE WORK

5.1.1   Fabrication of complex resonator profiles with ultra-high precision

We have demonstrated that slow cooking process can generate permanent SMRs with a Lorentzian-shaped profile. However, desired applications for microresonators prescribe profiles of differing CWVs such as for delay lines, dispersion compensators and frequency combs [3,5,91–93]. We suggest that the programmed translation of the heating MF is capable of superimposing our Lorentzian-shaped alterations. Therefore, the CWV can be introduced by controlling the slow cooking time and heating power applied at predetermined positions along our MCF, as shown in Figure 5.1. Whilst, we have shown that an appropriate heating time and power have induced SMRs with linear growth, there are other variables which affect slow cooking such as the recycling of water, and the contact position of the MF with the MCF which changes during MF translation. Thus, suitable calibration of our system will be needed before each sample fabrication to generate the correct modifications in our MCF. In addition, the sensing procedure of the resultant SMR profiles should include a temperature control to
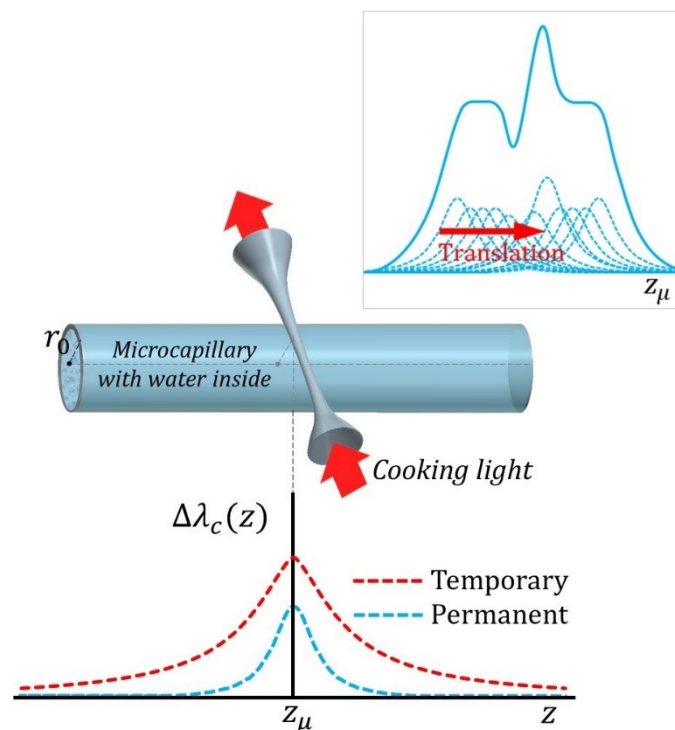

Figure 5.1. Illustration of the proposed technique to fabricate predetermined shapes at a MCF via programmed axial translation of a MF transmitting cooking light. Slow cooking uses optical WGMs of a water-filled MCF to induce a longitudinal temperature distribution (red dashed curve) and resultant permanent CWV (blue dashed curve). Translation of a heating MF transmitting cooking light can allow the introduction of a predetermined CW profile.

appropriately compensate for any picometre CW shifts caused by changes to the ambient conditions during measurement. This can be achieved by parallel-positioning of an extra control fibre of differing radius to our MCF. The sensing MF will contact both the MCF and the control fibre, exciting WGMs in both. Ambient changes during our spectrogram measurement will be recorded by the CWV of the WGMs in the control fibre, and used to correct the CWV measured at our MCF.

Importantly, if the temporary CWV is dependent on the heating MF coupling condition, then in turn, it must also affect the permanent changes found after slow cooking. Further experiments which characterize our coupling condition during optical heating could further our fabrication precision. For example, by standardizing the coupling condition we will ideally arrive at a relation between the induced temporary and permanent CWVs. This would facilitate direct observation of the slow cooking fabrication in real time, allowing us to generate a feedback control system for precise SMR manufacture.

5.1.2   Theoretical modelling of the WGMs to further understanding about the silica-water interaction

By comparing the CW contrast, it is possible to determine which WGMs penetrate deeper into our MCF, closest to water. Although the radial modes are distinguishable, and polarisation separation is simple, identification of the correct azimuthal order is much more challenging. Their determination requires cumbersome modelling of the CWs. Precise modelling of the radial intensity distribution of CWs can identify the sensing efficiency of these modes, and thus, distinguish the possible silica-water interaction processes occurring at them. Our review of literature on the silica-water interaction has allowed us to infer which processes can lead to positive and negative CWV, but, it is reasonable to think that further analysis which restores the observed CWVs could elucidate the diffusion depths of these processes. Naturally, this modelling requires accurate characterization of the coupling condition of the heating MF to determine the overlap integrals with the excited WGMs.

5.1.3   Applications to food technology

Today there is great interest to develop new food packaging that is both sustainable and safe. We can develop our microfluidic sensing platform to probe the safety of food packaging. Since the high efficiency of WGM sensing requires the ultra-low loss of silica MCFs, we propose the addition of a thin coating of a new container material at the internal wall of our MCF filled with liquid food (see Figure
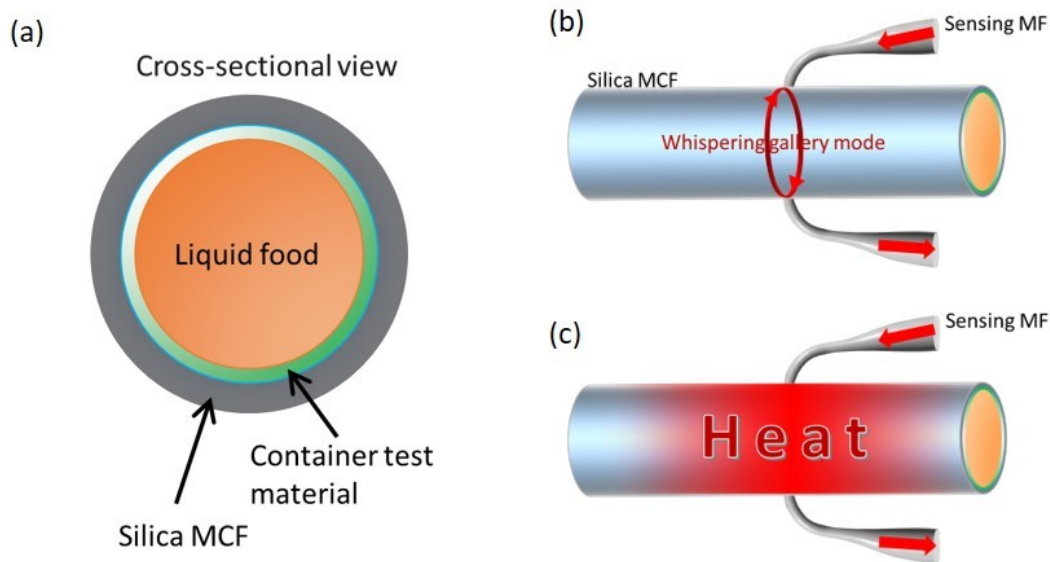

Figure 5.2. (a) Adaptation of our MCF by adding a thin coating of a container test material at the internal wall of our MCF. (b) Monitoring of the CWV over time. (c) Application of heat and liquid motion to simulate a dishwasher.

5.2(a)). We propose two procedures for corrosion testing of the container material. Firstly, b00000y using the setup shown in Figure 5.2(b), we contact the sensing MF with the MCF to monitor the CWV induced over time at ambient conditions. Secondly, we use a similar approach with the application of optical heating via a heating MF (not shown) as illustrated in Figure 5.2(c). The WGM heating which induces both a temperature variation and liquid motion, can be designed to simulate a dishwasher, and thus test the material's durability. Whilst care must be taken not to create alterations between the silica-water interface. However, if such alterations were measured, they would indicate the total corrosion of the container coating. Corrosion tests can be measured over days, weeks or longer during which minute physical changes at the container layer-liquid food interface are measured by our CWV.

5.1.4   Microfluidic sensing

As well as application of our microfluidic platform for food technology, we may probe physical and chemical processes between other solid and liquid materials. For example, we can replace a silica MCF used here with a MCF drawn from materials which have a sufficiently low attenuation of light. Additionally, we can use other liquids inside our MCF such as aprotic, colloidal and of varying pH. We

suggest that single molecule detection is possible with our slow-cooked SMRs. Thanks to the extraordinary sensitivity of the slow-cooked SMRs to the reversible silica-water interaction at ambient conditions, it may be instructive to incorporate a similar SMR for ultra-precise spatiotemporal microfluidic sensing.

We can also further the investigations of the WGM light-fluid momentum transfer, whose first observation was found in a droplet resonator [10]. We suspect that water motion significantly affects the processes in our MCF setup. In particular, characterization of the flow speeds induced by the radiative pressure of our WGM heating method could develop our understanding of this light-matter interaction.

5.1.5   Air-bubble microresonator

During our experiments, we observed the formation of an air bubble, between liquid droplets. In Figure 5.3.(a), we see the spectrogram of an air bubble surrounded by two water droplets within a MCF. Figure 5.3.(a1) shows the microscopic image of the scanned MCF section. In Figure 5.3.(b), we also find air bubble resonators formed between dimethyl sulfoxide (DMSO) droplets, whose scanned MCF section is shown in Figure 5.3.(b1). In the spectrogram, viewing the WGM at $\lambda_{cw}{\sim}1554.4$ nm, we do not find the CW perturbed at the three air-cavity locations. However, a higher radial mode $\lambda_{cw}{\sim}1553.4$ nm is perturbed by three air bubble resonators. Notably, DMSO creates a more prominent resonator with many more axial modes than in the air bubble of the same axial length surrounded by water. We propose that there are stronger reflections at the air-droplet interface using DMSO droplets due to its higher refractive index, which is not so dissimilar to the index of silica. Nonetheless, it interesting to observe the confinement of light in the less dense air bubble.

This is not the first experimental demonstration of a microresonator at an air cavity within a fibre. Previous work demonstrated an air bubble resonator formed via splicing of two standard optical fibres [96]. In this work, a rectangular air bubble was encapsulated by silica, and, applied to the ultra-high sensing of strain. Further investigation into the demonstrated air bubble resonator encapsulated by liquid could generate a new sensing approach, which could be applied to micro-gas sensing.
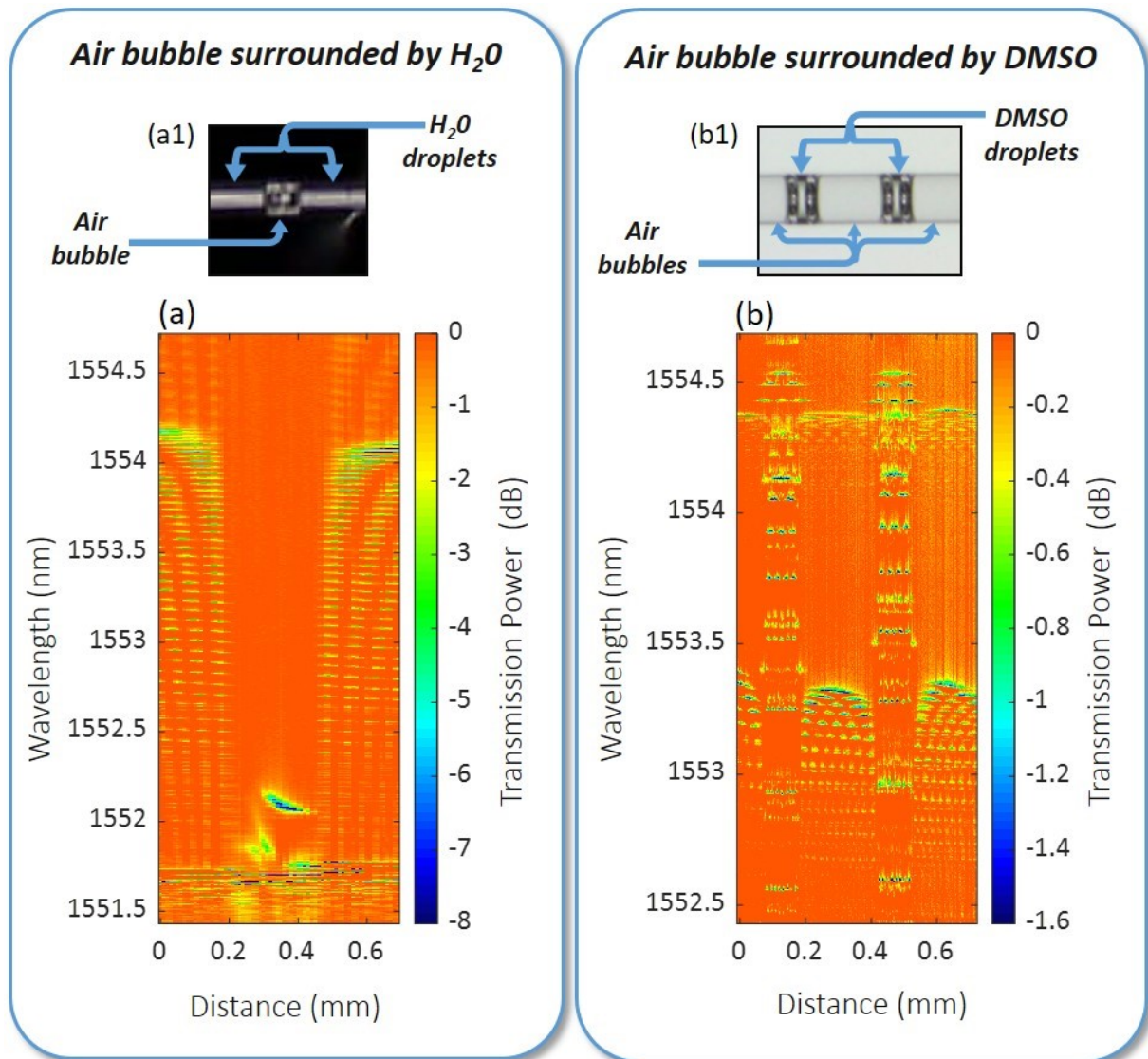
Figure 5.3. Observation of an air bubble resonator. (a) The spectrogram of one air bubble is surrounded by two water droplets, with the microscopic image of the scanned MCF length shown in (a1). (b) The spectrogram of three air bubbles between dimethyl sulfoxide droplets, with the corresponding microscopic image shown in (b1).

5.2 Conclusions

This thesis began with an introduction to WGM resonators, outlining the new generation of microfluidic sensors based on silica structures. I review known processes caused by WGM light-fluid interaction that leads to momentum transfer, as well as the interaction at the silica-water interface as a result of the hydrolysis and hydration processes of the silica material. In Chapter 2, I introduce SNAP technology and the microresonator fabrication techniques already developed based on this microphotonic platform. I discuss the potential for the development of SNAP microfluidics. My incorporation of microfluidics with SNAP technology has led to the discovery of the slow cooking phenomenon [9]. This unexpected finding simultaneously promises to advance the precise fabrication of SMRs and offers a new detection method of the silica-water interaction.

The slow cooking method allows to optically heat a MCF using broadband light which couples into WGMs that evanescently penetrate into water generating a temperature variation along the MCF. As demonstrated in Chapter 3, sustaining the optical heating power via the heating MF fixed to the MCF permanently alters the silica MCF, forming a microresonator. I suggested that both temperature and water motion [10] instigate a continuous interaction between silica and water [39] to introduce a sufficient index variation for the confinement of light. The alterations may have a Lorentzian-shaped or more complex profile along the MCF axis, and can be grown linearly or nonlinearly with an appropriate slow-cooking heating power and duration.

In Chapter 4, I demonstrate control of the resonator's profile with 1.3 pm with minute-long slow cooking durations limited by the OSA resolution. Using this exceptionally slow silica-water interaction, I forecast a dramatic increase in fabrication precision of the CW at 0.02 pm per 10secs, corresponding to a precision of the ERV at 0.6 pm, two orders of magnitude better than the developed laser post-processing methods in SNAP [11,12]. Hence, the slow cooking method is a highly promising technique for the precision manufacture needed to create a diverse range of microphotonic devices such as delay lines, dispersion compensators, switches, buffers and frequency combs [3,5,91–93].

In addition, I relate the observed alterations in my experiments to the possible silica-water interaction processes, summarizing the effects on the CWV in Table 3.1. Whilst decisive deduction has proven challenging, I have inferred the likely processes occurring at each experiment. From the suggested observations of the silica-water interaction, two are the most prominent. Firstly, in Chapter 3, with the observation of the reversible de- and re-hydroxylation of silica [13] when water is removed and added again to the MCF. And, secondly, in Chapter 4, with the observation of silica's structural relaxation [62,63] after heating, deduced from the picometre-order CWV increase. To my knowledge,

such experimental demonstrations of these processes using WGM spectroscopy have never been previously achieved.

Altogether the slow cooking phenomenon appears to be a fruitful discovery with a multitude of applications whose scope is presented in the further work sections, ranging from the ultra-high precision fabrication of SMRs with complex profiles, to microfluidic sensing applicable to food technology and beyond. Yet, there is still so much to uncover using this new technique of fabrication and sensing. Certainly, I will continue to develop the slow-cooking method and I am excited to develop useful applications from my discovery.

LIST OF REFERENCES

1. M. Sumetsky, "Theory of SNAP devices: basic equations and comparison with the experiment," Opt. Express **20**, 22537 (2012).
2. M. Sumetsky, "Slow light optofluidics: a proposal," Opt. Lett. **39**, 5578 (2014).
3. S. V. Suchkov, M. Sumetsky, and A. A. Sukhorukov, "Frequency comb generation in SNAP bottle resonators," Opt. Lett. **42**, 2149 (2017).
4. D. L. P. Vitullo, G. Gardosi, S. Zaki, K. V. Tokmakov, M. Brodsky, and M. Sumetsky, "Discovery of Parabolic Microresonators Produced via Fiber Tapering," Opt. Lett. **43**, 4977 (2018).
5. M. Sumetsky, "Delay of Light in an Optical Bottle Resonator with Nanoscale Radius Variation: Dispersionless, Broadband, and Low Loss," Phys. Rev. Lett. **111**, 163901 (2013).
6. M. Sumetsky, "Microscopic optical buffering in a harmonic potential," Sci Rep **5**, 18569 (2016).
7. D. L. P. Vitullo, S. Zaki, G. Gardosi, B. J. Mangan, R. S. Windeler, M. Brodsky, and M. Sumetsky, "Tunable SNAP microresonators via internal ohmic heating," Opt. Lett. **43**, 4316 (2018).
8. A. Dmitriev, N. Toropov, and M. Sumetsky, "Transient reconfigurable subangstrom-precise photonic circuits at the optical fiber surface," in *2015 IEEE Photonics Conference (IPC)* (IEEE, 2015), pp. 1–2.
9. G. Gardosi, B. J. Mangan, G. S. Puc, and M. Sumetsky, "Photonic Microresonators Created by Slow Optical Cooking," ACS Photonics (2021).
10. D. Bar-David, S. Maayani, L. L. Martin, and T. Carmon, "Cavity optofluidics: a μdroplet's whispering-gallery mode makes a μvortex," Opt. Express **26**, 19115 (2018).
11. N. A. Toropov and M. Sumetsky, "Permanent matching of coupled optical bottle resonators with better than 0.16 GHz precision," Opt. Lett. **41**, 2278 (2016).
12. Q. Yu, Y. Du, Z. Xu, P. Wang, Z. Zhang, Z. Zhu, H. Cao, M. Sumetsky, and X. Shu, "Efficient postprocessing technique for fabricating surface nanoscale axial photonics microresonators with subangstrom precision by femtosecond laser," Opt. Lett. **43**, 5729–5732 (2018).
13. S. L. Warring, D. A. Beattie, and A. J. McQuillan, "Surficial Siloxane-to-Silanol Interconversion during Room-Temperature Hydration/Dehydration of Amorphous Silica Films Observed by ATR-IR and TIR-Raman Spectroscopy," Langmuir **32**, 1568–1576 (2016).
14. J. W. Strutt, *Scientific Papers* (Cambridge University Press, 2009).
15. S. C. Hagness, D. Rafizadeh, S.-T. Ho, and A. Taflove, "Suppression of Higher-Order Radial Whispering Gallery Modes in Waveguide-Coupled Microcavity Disk Resonators," 2 (n.d.).
16. A. M. Armani, R. P. Kulkarni, S. E. Fraser, R. C. Flagan, and K. J. Vahala, "Label-Free, Single-Molecule Detection with Optical Microcavities," Science **317**, 783–787 (2007).
17. I. Teraoka and S. Arnold, "Enhancing the sensitivity of a whispering-gallery mode microsphere sensor by a high-refractive-index surface layer," J. Opt. Soc. Am. B **23**, 1434 (2006).
18. J. M. Ward, Y. Yang, and S. N. Chormaic, "Highly Sensitive Temperature Measurements With Liquid-Core Microbubble Resonators," IEEE Photon. Technol. Lett. **25**, 2350–2353 (2013).
19. M. R. Foreman, J. D. Swaim, and F. Vollmer, "Whispering gallery mode sensors," Adv. Opt. Photon. **7**, 168 (2015).

20. M. L. Gorodetsky and V. S. Ilchenko, "Optical microsphere resonators: optimal coupling to high-Q whispering-gallery modes," J. Opt. Soc. Am. B **16**, 147 (1999).
21. M. D. Baaske, M. R. Foreman, and F. Vollmer, "Single-molecule nucleic acid interactions monitored on a label-free microcavity biosensor platform," Nature Nanotech **9**, 933–939 (2014).
22. Y. Zhang, T. Zhou, B. Han, A. Zhang, and Y. Zhao, "Optical bio-chemical sensors based on whispering gallery mode resonators," Nanoscale **10**, 13832–13856 (2018).
23. Z. Qiao, X. Gong, P. Guan, Z. Yuan, S. Feng, Y. Zhang, M. Kim, G.-E. Chang, and Y.-C. Chen, "Lasing action in microdroplets modulated by interfacial molecular forces," Adv. Photon. **3**, (2021).
24. T. Hamidfar, K. V. Tokmakov, B. J. Mangan, R. S. Windeler, A. V. Dmitriev, D. L. P. Vitullo, P. Bianucci, and M. Sumetsky, "Localization of light in an optical microcapillary induced by a droplet," Optica **5**, 382 (2018).
25. V. D. Ta, S. Caixeiro, F. M. Fernandes, and R. Sapienza, "Microsphere Solid-State Biolasers," Advanced Optical Materials **5**, 1601022 (2017).
26. X.-C. Yu, S.-J. Tang, W. Liu, Y. Xu, Q. Gong, Y.-L. Chen, and Y.-F. Xiao, "Single-molecule optofluidic microsensor with interface whispering gallery modes," Proc Natl Acad Sci USA **119**, e2108678119 (2022).
27. S. Subramanian, S. Vincent, and F. Vollmer, "Effective linewidth shifts in single-molecule detection using optical whispering gallery modes," Appl. Phys. Lett. **117**, 151106 (2020).
28. F. Vollmer and S. Arnold, "Whispering-gallery-mode biosensing: label-free detection down to single molecules," Nat Methods **5**, 591–596 (2008).
29. F. Vollmer, S. Arnold, and D. Keng, "Single virus detection from the reactive shift of a whispering-gallery mode," Proc. Natl. Acad. Sci. U.S.A. **105**, 20701–20704 (2008).
30. I. M. White, H. Oveys, and X. Fan, "Liquid-core optical ring-resonator sensors," Opt. Lett. **31**, 1319 (2006).
31. K. Scholten, X. Fan, and E. T. Zellers, "A microfabricated optofluidic ring resonator for sensitive, high-speed detection of volatile organic compounds," Lab Chip **14**, 3873–3880 (2014).
32. S. I. Shopova, C. W. Blackledge, and A. T. Rosenberger, "Enhanced evanescent coupling to whispering-gallery modes due to gold nanorods grown on the microresonator surface," Appl. Phys. B **93**, 183–187 (2008).
33. D. Zhu, Y. Zhou, X. Yu, P. Shum, and F. Luan, "Radially graded index whispering gallery mode resonator for penetration enhancement," Opt. Express **20**, 26285 (2012).
34. D. Ganta, E. B. Dale, J. P. Rezac, and A. T. Rosenberger, "Optical method for measuring thermal accommodation coefficients using a whispering-gallery microresonator," The Journal of Chemical Physics **135**, 084313 (2011).
35. J. Liao and L. Yang, "Optical whispering-gallery mode barcodes for high-precision and wide-range temperature measurements," Light Sci Appl **10**, 32 (2021).
36. T. Reynolds, N. Riesen, A. Meldrum, X. Fan, J. M. M. Hall, T. M. Monro, and A. François, "Fluorescent and lasing whispering gallery mode microresonators for sensing applications," Laser & Photonics Reviews **11**, 1600265 (2017).
37. O. V. Svitelskiy, Y. Li, M. Sumetsky, D. Carnegie, E. Rafailov, and V. N. Astratov, "Resonant coupling to microspheres and light pressure effects in microfluidic fiber-integrated platforms," in *IEEE Photonic Society 24th Annual Meeting* (IEEE, 2011), pp. 185–186.
38. S. Arnold, D. Keng, S. I. Shopova, S. Holler, W. Zurawsky, and F. Vollmer, "Whispering gallery mode carousel – a photonic mechanism for enhanced nanoparticle detection in biosensing," Opt. Express **17**, 6230 (2009).

39. D. Lis, E. H. G. Backus, J. Hunger, S. H. Parekh, and M. Bonn, "Liquid flow along a solid surface reversibly alters interfacial chemistry," Science **344**, 1138–1142 (2014).

40. Md. S. Azam, C. Cai, J. M. Gibbs, E. Tyrode, and D. K. Hore, "Silica Surface Charge Enhancement at Elevated Temperatures Revealed by Interfacial Water Signals," J. Am. Chem. Soc. **142**, 669–673 (2020).

41. M. Tomozawa, D.-L. Kim, A. Agarwal, and K. M. Davis, "Water diffusion and surface structural relaxation of silica glasses," 8 (2001).

43. L. Dalstein, E. Potapova, and E. Tyrode, "The elusive silica/water interface: isolated silanols under water as revealed by vibrational sum frequency spectroscopy.," Phys Chem Chem Phys **19**, 10343–10349 (2017).

43. S. Nihonyanagi, S. Yamaguchi, and T. Tahara, "Ultrafast Dynamics at Water Interfaces Studied by Vibrational Sum Frequency Generation Spectroscopy," Chem. Rev. **117**, 10665–10693 (2017).

44. D. J. Rosenberg, S. Alayoglu, R. Kostecki, and M. Ahmed, "Synthesis of microporous silica nanoparticles to study water phase transitions by vibrational spectroscopy," Nanoscale Adv. **1**, 4878–4887 (2019).

45. H. Wakabayashi and M. Tomozawa, "Diffusion of Water into Silica Glass at Low Temperature," J American Ceramic Society **72**, 1850–1855 (1989).

46. K. M. Davis and M. Tomozawa, "Water diffusion into silica glass: Structural changes in silica glass and their effect on water solubility and diffusivity," Journal of Non-Crystalline Solids **185**, 203–220 (1995).

47. Z. Huang, "Penetration rate of water in sapphire and silica optical fibers at elevated temperature and pressure," Opt. Eng **43**, 1272 (2004).

48. P. J. Lezzi, M. Tomozawa, and T. A. Blanchet, "Evaluation of residual curvature in two-point bent glass fibers," Journal of Non-Crystalline Solids **364**, 77–84 (2013).

49. P. J. Lezzi and M. Tomozawa, "An Overview of the Strengthening of Glass Fibers by Surface Stress Relaxation," Int J Appl Glass Sci **6**, 34–44 (2015).

50. G. J. Young and T. P. Bursh, "Immersion calorimetry studies of the interaction of water with silica surfaces," Journal of Colloid Science **15**, 361–369 (1960).

51. S. M. Wiederhorn, T. Fett, J.-P. Guin, and M. Ciccotti, "Griffith Cracks at the Nanoscale," Int J Appl Glass Sci **4**, 76–86 (2013).

52. C. Peng, S. Song, and T. Fort, "Study of hydration layers near a hydrophilic surface in water through AFM imaging," Surf. Interface Anal. **38**, 975–980 (2006).

53. B. C. Bunker, "Molecular mechanisms for corrosion of silica and silicate glasses," Journal of Non-Crystalline Solids **179**, 300–308 (1994).

54. R. S. Robinson and H. H. Yuce, "Scanning Tunneling Microscopy of Optical Fiber Corrosion: Surface Roughness Contribution to Zero-Stress Aging," J American Ceramic Society **74**, 814–818 (1991).

55. J. J. Mazer and J. V. Walther, "Dissolution kinetics of silica glass as a function of pH between 40 and 85°C," Journal of Non-Crystalline Solids **170**, 32–45 (1994).

56. P. M. Dove, N. Han, A. F. Wallace, and J. J. De Yoreo, "Kinetics of amorphous silica dissolution and the paradox of the silica polymorphs," Proceedings of the National Academy of Sciences **105**, 9903–9908 (2008).

57. C. L. Rountree, "Recent progress to understand stress corrosion cracking in sodium borosilicate glasses: linking the chemical composition to structural, physical and fracture properties," J. Phys. D: Appl. Phys. **50**, 343002 (2017).

58. S. M. Wiederhorn, F. Yi, D. LaVan, L. J. Richter, T. Fett, and M. J. Hoffmann, "Volume Expansion Caused by Water Penetration into Silica Glass," J. Am. Ceram. Soc. **98**, 78–87 (2015).

G. I. Gardosi, PhD Thesis, Aston University, 2022.

59. A. M. Schrader, J. I. Monroe, R. Sheil, H. A. Dobbs, T. J. Keller, Y. Li, S. Jain, M. S. Shell, J. N. Israelachvili, and S. Han, "Surface chemical heterogeneity modulates silica surface hydration," Proc Natl Acad Sci USA **115**, 2890–2895 (2018).

60. M. Tomozawa, K. M. Davis, J. H. Seaman, and E. M. Aaldenberg, "The origin of anomalous water diffusion in silica glasses at low temperatures," J Am Ceram Soc **100**, 4548–4561 (2017).

61. M. Ciccotti, "Stress-corrosion mechanisms in silicate glasses," J. Phys. D: Appl. Phys. **42**, 214006 (2009).

62. M. Vannoni, A. Sordini, and G. Molesini, "Relaxation time and viscosity of fused silica glass at room temperature," Eur. Phys. J. E **34**, 92 (2011).

63. S.-R. Ryu and M. Tomozawa, "Structural Relaxation Time of Bulk and Fiber Silica Glass as a Function of Fictive Temperature and Holding Temperature," J American Ceramic Society **89**, 81–88 (2006).

64. S. M. Wiederhorn, G. Rizzi, S. Wagner, M. J. Hoffmann, and T. Fett, "Diffusion of water in silica glass in the absence of stresses," J Am Ceram Soc **100**, 3895–3902 (2017).

65. H. Ehrlich, K. D. Demadis, O. S. Pokrovsky, and P. G. Koutsoukos, "Modern Views on Desilicification: Biosilica and Abiotic Silica Dissolution in Natural and Artificial Environments," Chem. Rev. **110**, 4656–4689 (2010).

66. E. F. Vansant, P. V. D. Voort, and K. C. Vrancken, eds., "Chapter 3 The surface chemistry of silica," in *Characterization and Chemical Modification of the Silica Surface*, Studies in Surface Science and Catalysis (Elsevier, 1995), Vol. 93, pp. 59–77.

67. T. A. Michalske and S. W. Freiman, "A molecular interpretation of stress corrosion in silica," Nature **295**, 511–512 (1982).

68. T. A. Michalske and B. C. Bunker, "A Chemical Kinetics Model for Glass Fracture," J American Ceramic Society **76**, 2613–2618 (1993).

69. P. V. Brady and J. V. Walther, "Controls on silicate dissolution rates in neutral and basic pH solutions at 25°C," Geochimica et Cosmochimica Acta **53**, 2823–2830 (1989).

70. F. K. Crundwell, "On the Mechanism of the Dissolution of Quartz and Silica in Aqueous Solutions," ACS Omega **2**, 1116–1127 (2017).

71. N. Kitamura, K. Fukumi, J. Nishii, and N. Ohno, "Relationship between refractive index and density of synthetic silica glasses," Journal of Applied Physics **101**, 123533 (2007).

72. H. N. Ritland, "Relation Between Refractive Index and Density of a Glass at Constant Temperature," J American Ceramic Society **38**, 86–88 (1955).

73. M. Sumetsky, "Nanophotonics of optical fibers," Nanophotonics **2**, 393–406 (2013).

74. M. Sumetsky and Y. Dulashko, "SNAP: Fabrication of long coupled microresonator chains with sub-angstrom precision," Opt. Express **20**, 27896 (2012).

75. Y. Yang and M. Sumetsky, "In situ observation of slow and tunnelling light at the cutoff wavelength of an optical fiber," Opt. Lett. **45**, 762 (2020).

76. M. Crespo-Ballesteros and M. Sumetsky, "Controlled Transportation of Light by Light at the Microscale," Phys. Rev. Lett. **126**, 153901 (2021).

77. M. Sumetsky, D. J. DiGiovanni, Y. Dulashko, J. M. Fini, X. Liu, E. M. Monberg, and T. F. Taunay, "Surface nanoscale axial photonics: robust fabrication of high-quality-factor microresonators," Opt. Lett. **36**, 4824 (2011).

78. M. Sumetsky and J. M. Fini, "Surface nanoscale axial photonics," Opt. Express **19**, 26470 (2011).

79. M. Pöllinger, D. O'Shea, F. Warken, and A. Rauschenbeutel, "Ultrahigh- Q Tunable Whispering-Gallery-Mode Microresonator," Phys. Rev. Lett. **103**, 053901 (2009).

80. Q. Yu, S. Zaki, Y. Yang, N. Toropov, X. Shu, and M. Sumetsky, "Rectangular SNAP microresonator fabricated with a femtosecond laser," Opt. Lett. **44**, 5606 (2019).

G. I. Gardosi, PhD Thesis, Aston University, 2022.

81. D. Bochek, N. Toropov, I. Vatnik, D. Churkin, and M. Sumetsky, "SNAP microresonators introduced by strong bending of optical fibers," Opt. Lett. **44**, 3218 (2019).

82. N. Toropov, S. Zaki, T. Vartanyan, and M. Sumetsky, "Microresonator devices lithographically introduced at the optical fiber surface," Opt. Lett. **46**, 1784 (2021).

83. F. B. Kenrick, C. S. Gilbert, and K. L. Wismer, "The Superheating of Liquids," J. Phys. Chem. **28**, 1297–1307 (1924).

84. L. P. Yarin, A. Mosyak, and G. Hetsroni, *Fluid Flow, Heat Transfer and Boiling in Micro-Channels*, Heat and Mass Transfer (Springer, 2009).

85. B. H. Erné and Penny Snetsinger, "Thermodynamics of water superheated in the microwave oven," J. Chem. Educ. **77**, 1309 (2000).

86. H.-F. Fan, F. Li, R. N. Zare, and K.-C. Lin, "Characterization of Two Types of Silanol Groups on Fused-Silica Surfaces Using Evanescent-Wave Cavity Ring-Down Spectroscopy," Anal. Chem. **79**, 3654–3661 (2007).

87. A. Karbalaei, R. Kumar, and H. Cho, "Thermocapillarity in Microfluidics—A Review," Micromachines **7**, 13 (2016).

88. M. Ciccotti, "Stress-corrosion mechanisms in silicate glasses," J. Phys. D: Appl. Phys. **42**, 214006 (2009).

89. B. Voigtländer, *Atomic Force Microscopy*, NanoScience and Technology (Springer International Publishing, 2019).

90. K.-S. Isleif, G. Heinzel, M. Mehmet, and O. Gerberding, "Compact Multifringe Interferometry with Subpicometer Precision," Phys. Rev. Applied **12**, 034025 (2019).

91. Z. Lu, J. Jhoja, J. Klein, X. Wang, A. Liu, J. Flueckiger, J. Pond, and L. Chrostowski, "Performance prediction for silicon photonics integrated circuits with layout-dependent correlated manufacturing variability," Opt. Express **25**, 9712 (2017).

92. H. Jayatilleka, H. Frish, R. Kumar, J. Heck, C. Ma, M. N. Sakib, D. Huang, and H. Rong, "Post-Fabrication Trimming of Silicon Photonic Ring Resonators at Wafer-Scale," J. Lightwave Technol. **39**, 5083–5088 (2021).

93. H. Jayatilleka, H. Shoman, L. Chrostowski, and S. Shekhar, "Photoconductive heaters enable control of large-scale silicon photonic ring resonator circuits," Optica **6**, 84 (2019).

94. H. Lee, T. Chen, J. Li, K. Y. Yang, S. Jeon, O. Painter, and K. J. Vahala, "Chemically etched ultrahigh-Q wedge-resonator on a silicon chip," Nature Photon **6**, 369–373 (2012).

95. Y. Wang, K. Zhang, S. Zhou, Y.-H. Wu, M.-B. Chi, and P. Hao, "Coupled-mode induced transparency in a bottle whispering-gallery-mode resonator," Opt. Lett. **41**, 1825 (2016).

96. S. Liu, K. Yang, Y. Wang, J. Qu, C. Liao, J. He, Z. Li, G. Yin, B. Sun, J. Zhou, G. Wang, J. Tang, and J. Zhao, "High-sensitivity strain sensor based on in-fiber rectangular air bubble," Sci Rep **5**, 7624 (2015).

97. A. W. Snyder and J. D. Love, *Optical Waveguide Theory* (Springer US, 1984).

98. L. Tong, J. Lou, and E. Mazur, "Single-mode guiding properties of subwavelength-diameter silica and silicon wire waveguides," Opt. Express **12**, 1025 (2004).

99. L. Dalstein, E. Potapova, and E. Tyrode, "The elusive silica/water interface: isolated silanols under water as revealed by vibrational sum frequency spectroscopy.," Phys Chem Chem Phys **19**, 10343–10349 (2017).

APPENDICES

A. TUNING AND DEFORMATION OF PERMANENT SMRS USING OPTICAL HEATING

We present two experiments demonstrating firstly the thermal tuning of prefabricated SMRs (SNAP microresonators), and, secondly the total deformation of a SMR using the optical heating method.

A1. Experimental Procedure

In the first experiment we locally tune SMRs which had been fabricated using the CO_2 laser (Synrad 48-2) annealing method [11,79]. Using the experimental setup described in Section 3.2, the heating MF2 is positioned away from the SMRs so that the temperature variation thermally tunes selected SMRs of our scanned length. MF1 measures our CW profiles of the SMRs at the empty and filled MCF using up to 63 mW of power. The second experiment, uses just one SMR, and positions MF2 away from it, such that by increasing the optical heating, we observe total deformation of the SMR profile.

A2. Results and discussion

Figure A1(a) shows the spectrograms of the empty MCF, with the prefabricated SMRs 1-6 labelled in white. Analysis of the fundamental axial modes found no observable CWV to any of the SMRs, when optical heating is applied, see Figures A1(a1) and (a2). Comparatively, we find that in the spectrograms of the water-filled MCF shown in Figure A1(b), the SMRs undergo a resonant wavelength shift which increases with optical heating power. In Figure A1(b1), we find that using 8 mW heating power the fundamental axial modes of SMRs 4-6 shift by 1.3 pm (equal to the resolution of our OSA), whilst the corresponding modes of SMRs 1-3 are unaffected. More noticeably, using the higher optical heating power of 63 mW we significantly increase the CWV of SMRs 3-6, shown in Figure A1(b2). The largest CWV is found at SMR 6 which is closest to the MF2 heating position. The induced CWV allows temporary mode matching of SMRs 3 and 6, indicated by the black dashed line.

We continue our observations in Figure A2, which demonstrates the total deformation of our SMR. The fundamental axial mode of our SMR is still visible up to 32 mW of heating power. But, using 63 mW of optical power the SMR totally disappears, and the CWV transforms into the temperature variation observed in our slow cooking experiments, refer to Figure 3.3(b) in the main thesis.
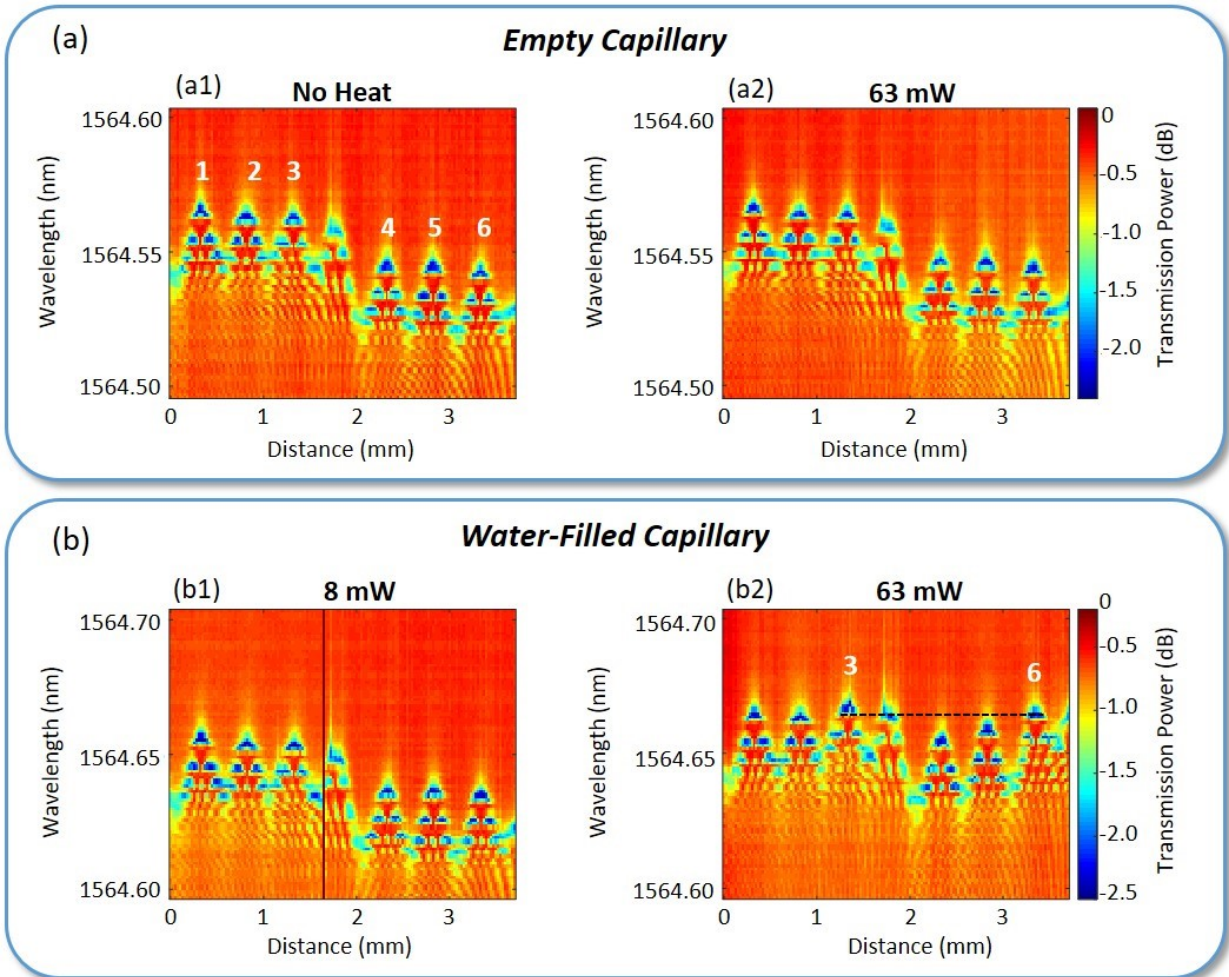
Figure A1. Spectrograms demonstrating local tuning of permanent SMRs fabricated at the MCF surface. (a) shows the CW profile at the empty MCF measured using no heating power in (a1) , with the SMRs 1-6 labelled in white. The measured profile during heating using 63 mW optical power is shown in (a2). (b) shows the CW profile at water-filled MCF using heating powers of 8 mW in (b1) and 63 mW in (b2). Matching of fundamental axial modes is indicated with the black dashed line in (b2) between SMRs 3 and 6. The dark vertical line in spectrogram (b1) is due to a missed measurement during the scanning of the MCF.
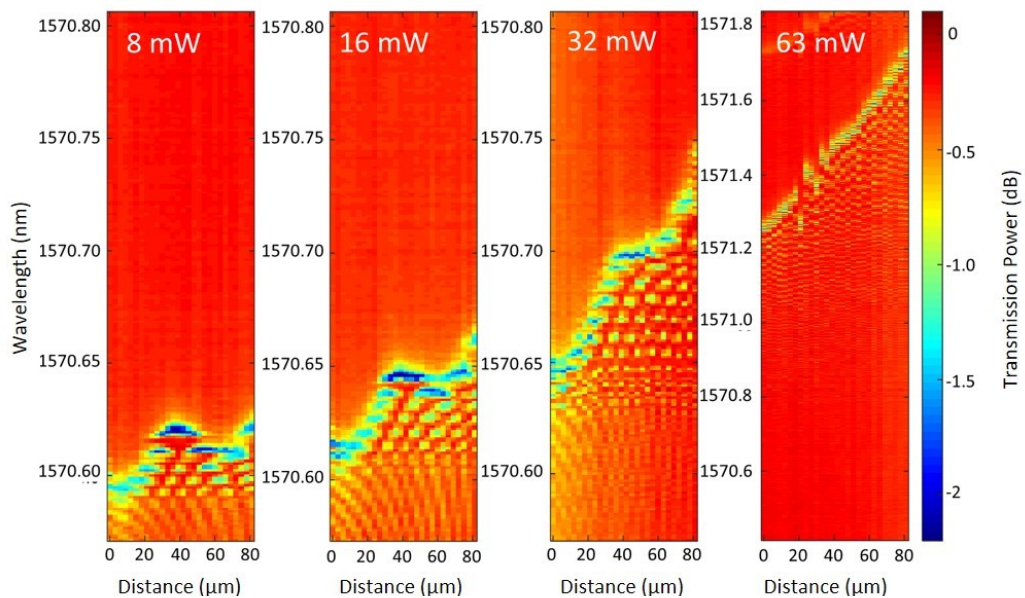
Figure A2. Demonstration of the total deformation of a SMR by increasing the optical broadband power from 8-63 mW.

G. I. Gardosi, PhD Thesis, Aston University, 2022.

B. Capillary radius measurement

We measure the cross-sectional geometry of the MCF used in our experiments shown in Figure B1 using a microscope. Our calculated external radius of the MCF using the azimuthal FSR relation (Equation 2.4 in the main thesis) is in in good agreement, shown in Table B1.
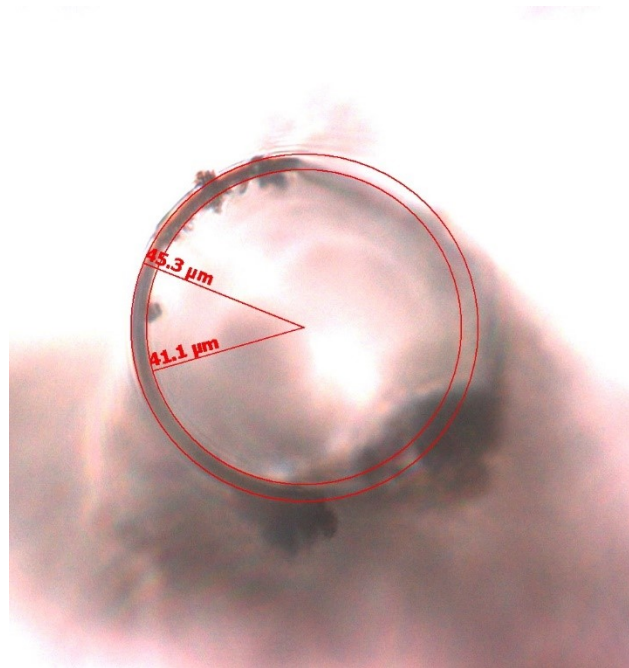

Figure B1. Microscope image of a cleaved MCF sample.

Table B1. Measurement of our MCF external radius and thickness.

	External radius	Wall thickness
From microscope	45.3 μm ($\pm$1 μm)	4.2 μm
Calculated from FSR$_{az}$	45.73 μm	n/a

C. Spectrogram Treatment

C1. Spectrogram cleaning procedure

Some spectrograms contain a titlted quasi-periodic background of the measured the transmission power, see the example in Figure C1(a). To remove the background from our spectrogram we target 10 wavelengths at which the propagation is not resonant, i.e. containing no CWs, see the dashed lines Figure C1(a). We expect the power to be smooth off resonance, however we find the transmission power is uneven, as shown in Figure C2(a). We use a spline interpolation of the transmission power between our targeted wavelengths, k=1,2…,10, which we perform for each z position (where MF1 contacts the MCF axial position during our spectrogram measurement) see Figure C2(b). This background, shown in Figure C1(b), is then subtracted from our original spectrum, $P_{corr}(\lambda, z) = P(\lambda, z) - P_{bkgr}(\lambda, z)$. The subsequent correct spectrogram is shown in Figure C1(c). Finally the original, background and corrected spectrograms are magnified in the neighbourhood of the CW at 1548 nm, as shown in Figures C1(a1), (b1) and (c1).
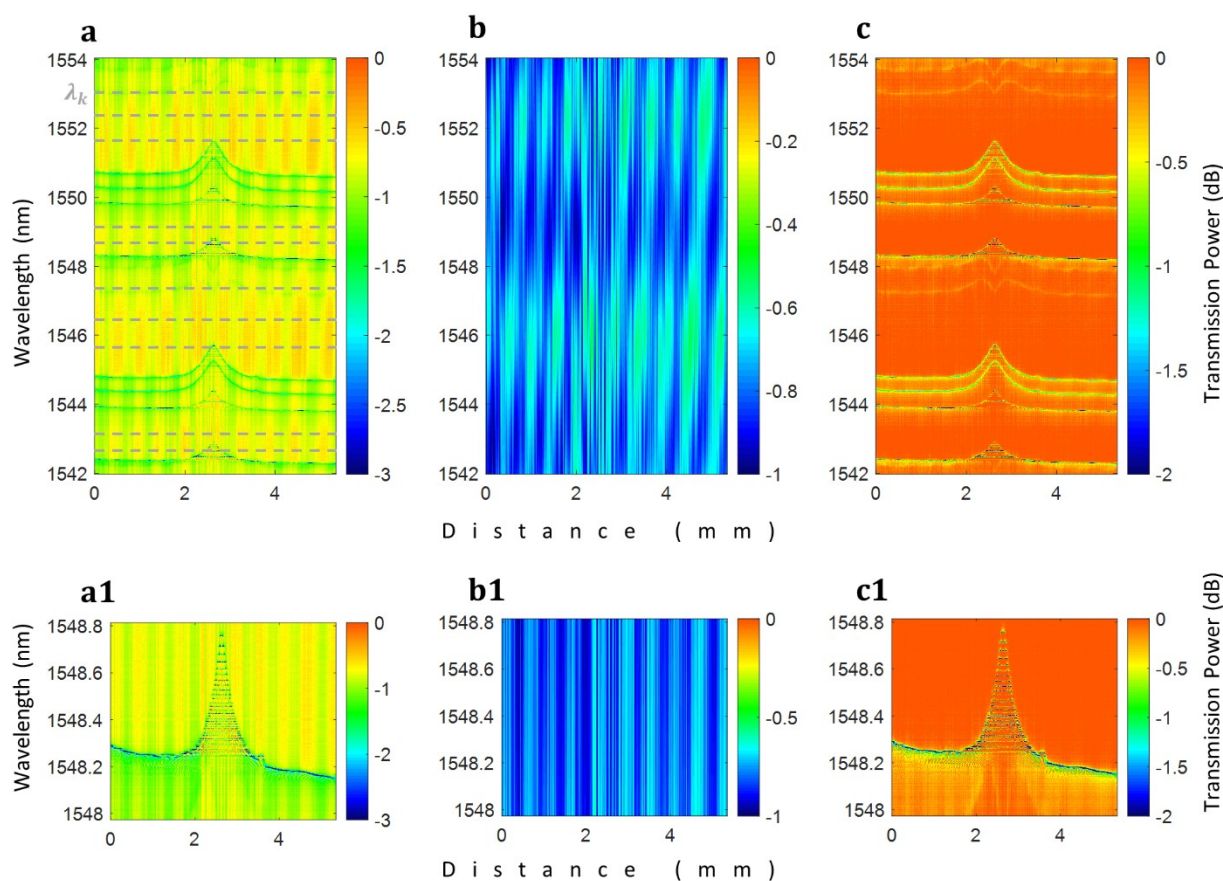

Figure C1. Spectrogram treatment. (a) The measured spectrogram with quasi-periodic background. (b) The background, $P_{bkgr}(\lambda, z)$ calculated using spline interpolation across selected off-resonance wavelengths for each z position. (c) The final spectrogram after subtraction of the background, P_{bkgr} from the measured spectrogram. (a1-c1) Magnified parts of (a-c). From Supplementary section of G. Gardosi et al., "Photonic Microresonators Created by Slow Optical Cooking," ACS Photonics (2021).

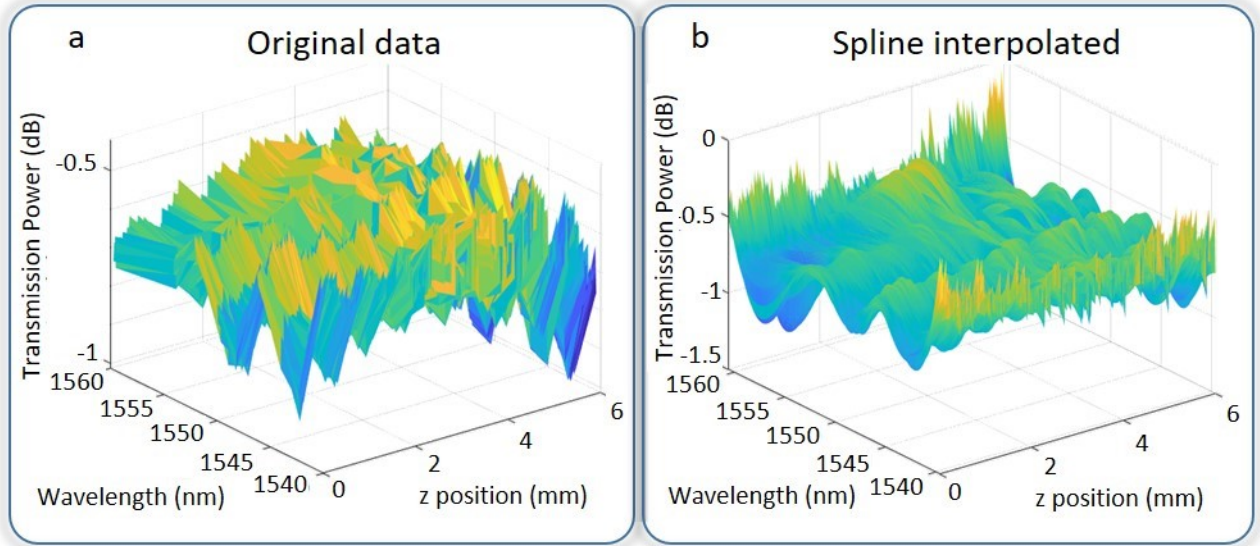G. I. Gardosi, PhD Thesis, Aston University, 2022.

Figure C2. Determination of the background. (a) shows the transmission powers at 10 targeted wavelengths which are not in resonance plotted at each z contact position between the MF and MCF during the spectrogram measurement. (b) shows the results using spline interpolation of the data in (a).

C2. Theory

We suggest that the experimental background arises from the interference of multiple modes propagating along the MF. Our U-shaped MFs, are not single-mode fibres, having a waist diameter of ~ 1.7 μm. Rather they are multi-mode waveguides containing fundamental and higher ordermodes. We define an optical mode guided by a uniform MF with propagation constant β_k as $E_k(x, \mathbf{r}) = A_k \exp(i\beta_k x) \cdot F_k(\mathbf{r})$, where x is the axial MF coordinate and $\mathbf{r}$ is the two-dimensional vector at a MF cross-section [97]. This mode excites the WGM in the MCF, which is defined in the cylindrical coordinates as $\mathcal{E}_{k,m,p,s}(z, \rho, \phi) = C_k A_k exp(i\beta_k x)\exp(im\phi) \cdot U_{m,p,s}(\rho) \cdot \Psi_{m,p,s}(z)$, where C_k are the coupling coefficients, A_k are the constants determined by the input optical power of the MF, and m, p and s are the azimuthal, radial and polarisation quantum numbers. If our MFs contained only the fundamental HE11 mode and the TE01 mode, with propagation constants β_0 and β_1, the excited WGM is determined by their superposition as

$$\mathcal{E}(z, \rho, \phi) = [C_0 A_0 \exp(i\beta_0 x) + C_1 A_1 \exp(i\beta_1 x)] \exp(im\phi) \cdot U_{m,p,s}(\rho) \cdot \Psi_{m,p,s}(z). \qquad (1)$$

Figure C3 shows the propagation constants dependent on the MF diameter for wavelength at $\lambda = 1.55$ μm. This figure was rescaled from a similar plot calculated for $\lambda = 0.633$ μm in [98]. From our rescaled plot we estimate the difference of propagation constants $\Delta\beta = |\beta_0 - \beta_1| \sim 0.6$ μm^{-1}. Following from Equation 1, we infer the characteristic period of oscillations along the MF1 waist length of $\Delta x = \frac{2\pi}{\Delta\beta} \sim 10$ μm.

We assume that the MF translation in the y direction is slightly tilted from the MCF axis along z, as illustrated in Figure C4. Therefore the tilt angle $\theta = \frac{\Delta x}{\Delta z} \sim 0.02$ radians or 1 degree, using the period of background oscillation $\Delta z \sim 500$ μm found from Figure C1(a). Additionally we propose that since the MCF is not perfectly straight, the tilt angle may change during MF translation, giving rise to a change in the period of background oscillations along the MCF length visible in Figure C1(b).
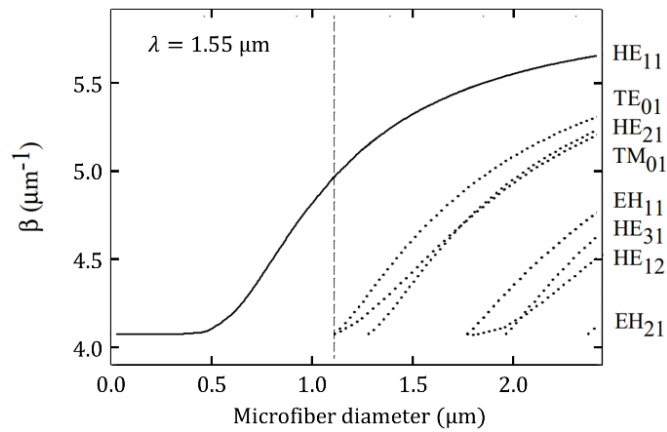

Figure C3. The propagation constants of different transmission modes of a silica microfiber as function of MF diameter at 1.55 μm wavelength (obtained by rescaling the results of [93]). From Supplementary section of G. Gardosi et al., "Photonic Microresonators Created by Slow Optical Cooking," ACS Photonics (2021).
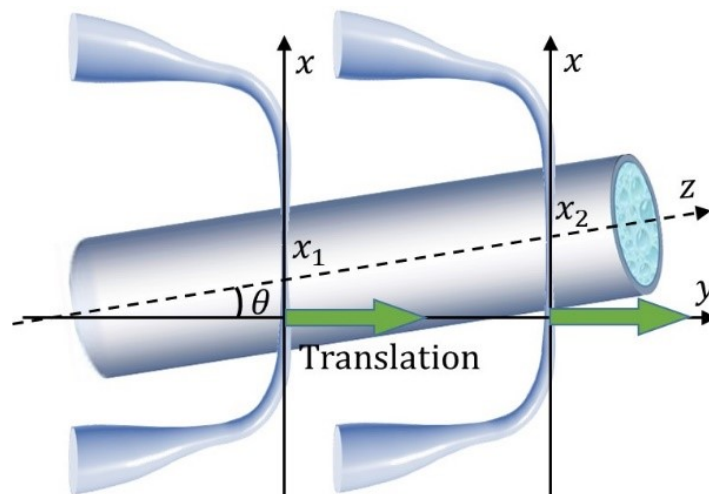

Figure C4. An illustration of a small angle between the MCF axis and MF1 translation direction during our spectrogram measurement, which causes the quasi-periodic background observed. From Supplementary section of G. Gardosi et al., "Photonic Microresonators Created by Slow Optical Cooking," ACS Photonics (2021).

G. I. Gardosi, PhD Thesis, Aston University, 2022.

D. EVIDENCE OF WATER REMAINING ITS LIQUID STATE DURING SLOW COOKING

Below we show confirmation that water remained in its liquid state and did not vaporize in the experiments presented in the main thesis. Occasionally during experimentation we observed the evaporation of water when the optical heating power was very large. However this was easily noticed by use of a microscope camera which monitored the presence of liquid water in our MCF over the slow cooking duration. In addition, the temporal spectrogram which measured the transmission spectrum at 1min intervals, shown in Figure, D1(a), records a CWV jump for all modes at the instant of evaporation. The magnified spectrogram in Figure D1(b) shows the temporal region of evaporation. We see that at $t < 6.5$hrs the CWV steadily increases, with the presence of liquid water within our MCF imaged in Figure D1(c). However at $t \sim 6.5$hrs the rapid change of CW for all WGMs is observed. For a higher radial mode, shown by the CWs with wider yellow lines, we see an exponential decrease in CWV. At this time we see the evaporation of water shown in the microscope image in Figure D1(d). The disappearance of water induces both a refractive index change and reduction in heating. For comparison of the temperature reduction in an empty capillary, see Figure 3.3(c) in the main thesis. Therefore, since we observed no change in our microscope images or CW jumps in our temporal spectrograms, we confirm that water remained in its liquid state for the duration of our slow cooking experiments presented in the main thesis.
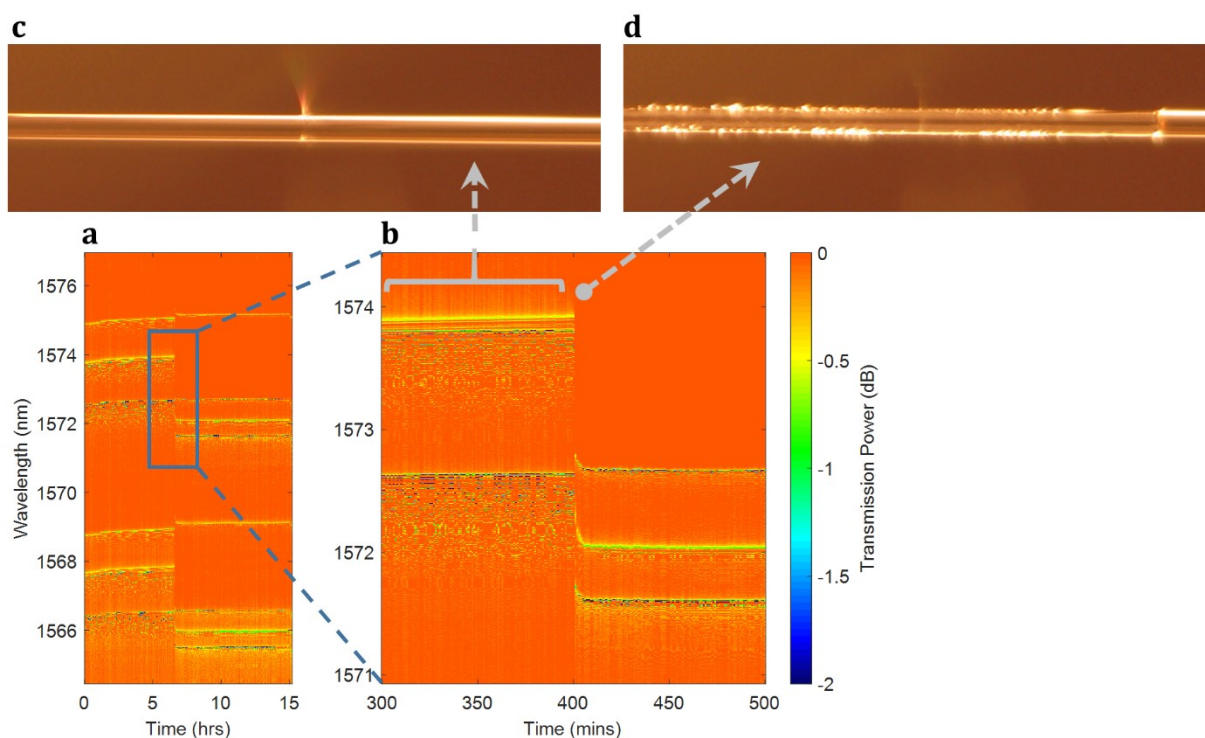

Figure D1. Water evaporation. (a) Temporal spectrogram during slow cooking measured at the MF2 axial position. (b) Magnified temporal region of evaporation. Microscope images of the MCF and contact MFs showing water in its liquid state in(c) at $t < 6.5$ hrs and in its vapour state in (d) at t ~ 6.5 hrs.

E. REPEATABILITY TEST OF MF TRANSLATION VIA ITS POWER LOSS OVER A LARGE BANDWIDTH

Ultra-high fabrication precision using programmed translation is dependent on the repeatability of our heating MF2 to arrive at the pre-determined axial position of the MCF. Additionally during our coupling optimization experiment we determined that the transverse taper waist coupling position of MF2 can affect our WGM heating effect. Therefore it is important to establish the repeatability of our micro-positioning stages. Here, we compare the power transmission through a MF to determine the possible errors which can incur during our proposed slow cooking fabrication process.

E1. Methodology

Our MF is brought into contact with the water-filled MCF, and we take 100 spectral measurements using a large bandwidth of 86.13 nm. We repeat this process adding y-translation (taking the MF out of contact and back into contact with the MCF) and then x- and y-translation (used for programmed translation) between each measurement. For comparison, we also take measurements when MF2 is out of contact with MCF. For each run of spectral measurement the power loss is integrated across the 86.13 nm bandwidth.

E2. Results and Discussion

We normalize the transmission power losses to the out of contact measurements, shown in Figure E1. We find that once the MF contacts the MCF the losses increase, as expected due to the excitation of WGMs and scattering. The loss variation, significantly increases with added translation. Thus, where possible we must reduce translation of the MF2 due to the introduction of power variations which could substantially affect our slow-cooking fabrication of SMRs.
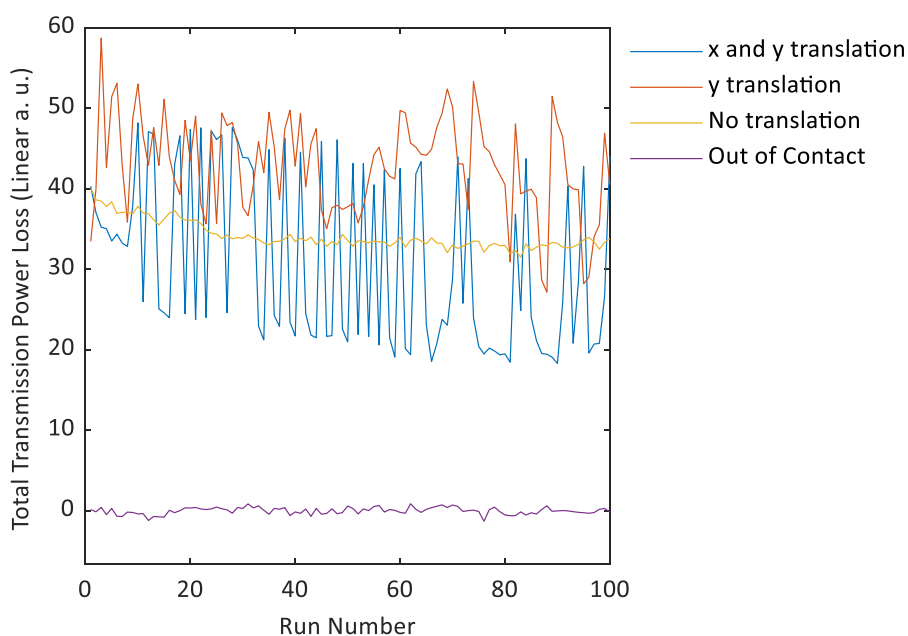

Figure E1. Repeatability test of total transmission power loss via MF1 with its translation.

G. I. Gardosi, PhD Thesis, Aston University, 2022.